Tailored disorder and anisotropic scattering in photonic nanostructures

Dissertation

zur Erlangung des akademischen Grades

doctor rerum naturalium

(Dr. rer. nat.)

im Fach Physik

Spezialisierung: Theoretische Physik

eingereicht an der

Mathematisch-Naturwissenschaftlichen Fakultät

der Humboldt-Universität zu Berlin

von

M.Sc. Paraschos Varytis

Präsidentin der Humboldt-Universität zu Berlin

Prof. Dr. Sabine Kunst

Dekan der Mathematisch-Naturwissenschaftlichen Fakultät

Prof. Dr. Elmar Kulke

Gutachter/innen:

1. Prof. Dr. Kurt Busch
2. Prof. Dr. Marian Florescu
3. Prof. Dr. Wolfram Pernice

Tag der mündlichen Prüfung: 31.10.2019

Ich erkläre, dass ich die Dissertation selbständig und nur unter Verwendung der von mir gemäß §7 Abs. 3 der Promotionsordnung der Mathematisch-Naturwissenschaftlichen Fakultät, veröffentlicht im Amtlichen Mitteilungsblatt der Humboldt-Universität zu Berlin Nr. 126/2014 am 18.11.2014 angegebenen Hilfsmittel angefertigt habe.

Weiterhin erkläre ich, dass ich mich nicht bereits anderwärts um einen Doktorgrad im Promotionsfach Physik beworben habe beziehungsweise einen entsprechenden Doktorgrad besitze.

Ich habe Kenntnis der dem Promotionsverfahren zugrunde liegenden Promotionsordnung der Mathematisch-Naturwissenschaftlichen Fakultät, veröffentlicht im Amtlichen Mitteilungsblatt der Humboldt-Universität zu Berlin Nr. 126/2014 am 18.11.2014.

Berlin, den 29. November 2019

Humboldt-Universität zu Berlin
Mathematisch-Naturwissenschaftliche Fakultät
Institut für Physik

Tailored disorder and anisotropic scattering in photonic nanostructures

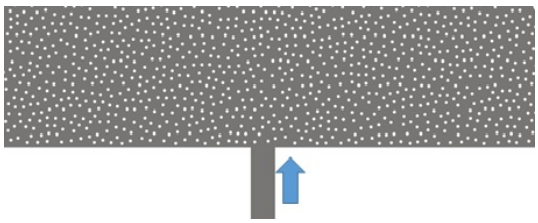

Dissertation
by Paraschos Varytis

Supervisor: Prof. Dr. Kurt Busch

To my family

Abstract

In this thesis, we study the optical response of planar spectrometers based on disorder scatterers, composite dielectric nanoparticles with plasmonic shell, and all-dielectric magneto-optical shape-modified metasurfaces. Therefore, we employ both Mie and multiple scattering theory as well as a discontinuous Galerkin time-domain method based on finite elements for the numerical computation of the electromagnetic fields. Specifically, we present a theoretical design study for obtaining random spectrometers with high spectral resolution. Furthermore, we provide an alternative strategy to achieve preferentially high backscattering by studying the optical properties of composite nanoparticles. Finally, we present enhanced Faraday rotation along with high transmittance in all-dielectric magneto-optical metasurfaces composed of shape-modified nanodisks.

Zusammenfassung

In dieser Arbeit untersuchen wir das optische Antwortverhalten von planaren Spektrometern basierend auf ungeordneten Streuzentren, dielektrischen Verbundnanopartikeln mit einer plasmonischer Ummantelung, sowie volldielektrischen magnetooptischen formveränderten Metaoberflächen. Dafür benutzen wir sowohl Mie und Mehrfach-Streutheorie als auch ein unstetiges Galerkin Zeitraumverfahren basierend auf finiten Elementen zur numerischen Berechnung der elektromagnetischen Felder. Wir stellen insbesondere eine theoretische Designstudie vor, um ungeordnete Spektrometer mit hoher spektraler Auflösung zu erhalten. Darüber hinaus geben wir eine alternative Strategie an, um durch Untersuchung der optischen Eigenschaften von Verbundnanopartikeln eine Erhöhung der bevorzugten Rückstreuung zu erreichen. Zum Schluss präsentieren wir eine Erhöhung der Faraday-Rotation bei gleichzeitig hoher Transmission von volldielektrischen magnetooptischen Metaoberflächen, welche aus formangepassten Nanodisks bestehen.

Introduction

In this thesis, we study the optical properties of random spectrometers, plasmonic composite nanoparticles with dielectric-metal core-shell morphology and magneto-optical Huygens' metasurfaces composed of shape-modified all-dielectric nanodisks, by means of full electrodynamic simulations using a discontinuous Galerkin time-domain (DGTD) finite-element approach accompanied by Mie theory and multiple scattering theory [P1].

Compact spectrometers based on disordered waveguide exhibit high resolution with a small footprint due to multiple light scattering which enhances the optical path length. A design study of random spectrometers for TE and TM polarization in the near-infrared (NIR) and visible wavelength regime is reported. It is shown that for low concentration of scatterers, the performance of such spectrometers depends on single scattering quantities like scattering efficiency and asymmetry parameter. Moreover, enhanced effective optical path and therefore, high spectral resolution can be achieved in the visible and near-infrared region due to the reduction of the transport mean free path. Within this framework, Gehring et al. [P2] presented a hybrid approach of out-of-plane optical coupling from the top, to structures based on waveguides by utilizing 3D direct laser writing. The couplers are characterized by broad bandwidth and low losses. Furthermore, Hartmann et al. [P3] proceeded with the realization of broadband and compact on-chip random spectrometers operating from the visible up to telecom wavelength range. The experimental results and the theoretical findings show good agreement.

Moreover, plasmonic nanoparticles with dielectric-metal core-shell morphology exhibit hybrid plasmon modes at the outer and inner surfaces of the shell [P4]. In this work, we show that due to the interference of the hybrid plasmon modes, such composite subwavelength nanospheres exhibit negative asymmetry parameter and strong scattering in the optical region. Therefore, for a low density collection of scatterers, an anomalous regime occurs, where the extinction mean free path is longer than the transport mean free path. Explicit results for silver-coated nanospheres are presented.

Finally, magneto-optical Huygens' metasurfaces composed of shape-modified all dielectric nanodisks, which enable enhanced Faraday rotation angle along with high transmittance, are studied by means of full electromagnetic simulations [P5]. It is shown that by setting a number of control points along the circumference of the nanodisks and varying randomly their radial position, we obtain a strong Faraday rotation enhancement accompanied by almost 100% transmittance.

Contents

CHAPTER 1

Electromagnetic fields in homogeneous media

In this chapter, we present the fundamental theoretical background that is used in this thesis. After introducing Maxwell's equations and constitutive relations, we discuss the solutions of wave equation in simple isotropic media.

1.1 Maxwell's equations

Light propagation in matter, as well as all the relevant electric and magnetic effects, is described by Maxwell's equations, which in SI units, read [1]:

$$\begin{aligned} \nabla \cdot \mathbf{D}(\mathbf{r},t) &= \rho(\mathbf{r},t) & \nabla \cdot \mathbf{B}(\mathbf{r},t) &= 0 \\ \nabla \times \mathbf{E}(\mathbf{r},t) &= -\frac{\partial \mathbf{B}(\mathbf{r},t)}{\partial t} & \nabla \times \mathbf{H}(\mathbf{r},t) &= \frac{\partial \mathbf{D}(\mathbf{r},t)}{\partial t} + \mathbf{j}(\mathbf{r},t) \ , \end{aligned} \tag{1.1}$$

where $\mathbf{E}$ and $\mathbf{H}$ are the macroscopic electric and magnetic field, respectively, $\mathbf{D}$ the electric displacement and $\mathbf{B}$ the magnetic induction, while with ρ and $\mathbf{j}$ we denote the free charge density and the electric current density, respectively. By applying the divergence to both sides of the fourth Maxwell equation and making use of the first Maxwell equation and a vector identity that is always true and states that the divergence of the curl of any vector field is always zero, we obtain the continuity equation

$$\frac{\partial \rho(\mathbf{r},t)}{\partial t} + \nabla \cdot \mathbf{j}(\mathbf{r},t) = 0 \ . \tag{1.2}$$

Conservation of energy equates the rate of change of the stored energy and the power flux to the rate per unit volume at which electromagnetic fields gain energy via interaction with charges. By forming the scalar product of the fourth Maxwell equation with the

electric field, we obtain

$$\mathbf{E}(\mathbf{r},t)\cdot\big[\nabla\times\mathbf{H}(\mathbf{r},t)\big]-\mathbf{E}(\mathbf{r},t)\cdot\frac{\partial\mathbf{D}(\mathbf{r},t)}{\partial t}=\mathbf{E}(\mathbf{r},t)\cdot\mathbf{j}(\mathbf{r},t)\ . \tag{1.3}$$

Making use of the vector identity A.10 and third Maxwell equation, we get

$$\begin{aligned}\mathbf{H}(\mathbf{r},t)\cdot\frac{\partial\mathbf{B}(\mathbf{r},t)}{\partial t}+\mathbf{E}(\mathbf{r},t)\cdot\frac{\partial\mathbf{D}(\mathbf{r},t)}{\partial t}+\nabla\cdot\big[\mathbf{E}(\mathbf{r},t)\times\mathbf{H}(\mathbf{r},t)\big]&=-\mathbf{E}(\mathbf{r},t)\cdot\mathbf{j}(\mathbf{r},t)\\ \Rightarrow\frac{\partial U(\mathbf{r},t)}{\partial t}+\nabla\cdot\mathbf{S}(\mathbf{r},t)&=-\mathbf{E}(\mathbf{r},t)\cdot\mathbf{j}(\mathbf{r},t)\ ,\end{aligned} \tag{1.4}$$

where $\mathbf{S}\equiv\mathbf{E}\times\mathbf{H}$ and $\partial_t U=\mathbf{H}\cdot\partial_t\mathbf{B}+\mathbf{E}\cdot\partial_t\mathbf{D}$. When $\mathbf{E}\cdot\mathbf{j}=0$, Eq. 1.4 and continuity equation 1.2 have the same form. Here, U is the electromagnetic field energy per volume. $\mathbf{S}$ is called the Poynting vector and is the energy per unit area per unit time carried by the electromagnetic field.

1.2 Constitutive relations

The electric displacement and magnetic induction are connected to the electric and magnetic field through the constitutive relations, respectively. In the linear response regime, we have

$$\begin{aligned}D_i(\mathbf{r},t)&=\int_V d^3r'\int_{-\infty}^{+\infty}dt'\sum_j\epsilon_{ij}(\mathbf{r},t;\mathbf{r}',t')E_j(\mathbf{r}',t')\\ B_i(\mathbf{r},t)&=\int_V d^3r'\int_{-\infty}^{+\infty}dt'\sum_j\mu_{ij}(\mathbf{r},t;\mathbf{r}',t')H_j(\mathbf{r}',t')\ ,\end{aligned} \tag{1.5}$$

where the spatial integration occurs over the material's volume V. In isotropic materials, the dielectric and magnetic tensors are scalar: $\epsilon_{ij}=\epsilon\delta_{ij}$ and $\mu_{ij}=\mu\delta_{ij}$.

Due to time homogeneity, the temporal dependence of the response functions is expressed through the difference $t-t'$ and not through t and t' separately. Moreover, causality implies that these functions vanish for $t<t'$. If we assume that locality holds, i.e., in every point in space the electrical displacement and magnetic induction depend only on the fields on the same point, we obtain $\epsilon_{ij}(\mathbf{r},t;\mathbf{r}',t')=\epsilon_{ij}(\mathbf{r},t-t')\delta(\mathbf{r}-\mathbf{r}')$ and $\mu_{ij}(\mathbf{r},t;\mathbf{r}',t')=\mu_{ij}(\mathbf{r},t-t')\delta(\mathbf{r}-\mathbf{r}')$. Therefore, Eq. 1.5 takes the form

$$\begin{aligned}D_i(\mathbf{r},t)&=\int_{-\infty}^{+\infty}dt'\sum_j\epsilon_{ij}(\mathbf{r},t-t')E_j(\mathbf{r},t')\\ B_i(\mathbf{r},t)&=\int_{-\infty}^{+\infty}dt'\sum_j\mu_{ij}(\mathbf{r},t-t')H_j(\mathbf{r},t')\ .\end{aligned} \tag{1.6}$$

Using the Fourier transform $[\int_{-\infty}^{+\infty} dt \exp(i\omega t)\ldots]$, we obtain

$$\begin{aligned} D_i(\mathbf{r},\omega) &= \sum_j \epsilon_{ij}(\mathbf{r},\omega) E_j(\mathbf{r},\omega) \\ B_i(\mathbf{r},\omega) &= \sum_j \mu_{ij}(\mathbf{r},\omega) H_j(\mathbf{r},\omega) \ , \end{aligned} \tag{1.7}$$

where $f(\mathbf{r},\omega) = \int_{-\infty}^{+\infty} dt \exp(i\omega t) f(\mathbf{r},t)$. In matrix form, Eq. 1.7 reads

$$\begin{pmatrix} \mathbf{D} \\ \mathbf{B} \end{pmatrix} = \begin{pmatrix} \boldsymbol{\epsilon} & \mathbf{0} \\ \mathbf{0} & \boldsymbol{\mu} \end{pmatrix} \begin{pmatrix} \mathbf{E} \\ \mathbf{H} \end{pmatrix} \ . \tag{1.8}$$

It is worth noting that while the transformed fields and corresponding response functions are complex, the time-dependent fields and corresponding response functions are real and therefore

$$f(\mathbf{r},-\omega) = f^*(\mathbf{r},\omega) \ , \tag{1.9}$$

where $*$ denotes the complex conjugate. Due to the linearity of Maxwell's equations, the total field stems from the linear combination of monochromatic fields. Therefore, we can solve Maxwell's equations for any monochromatic field with the form

$$\begin{aligned} \mathbf{E}(\mathbf{r},t) &= \mathrm{Re}\left[\mathbf{E}(\mathbf{r},\omega)\exp(-i\omega t)\right] \\ \mathbf{H}(\mathbf{r},t) &= \mathrm{Re}\left[\mathbf{H}(\mathbf{r},\omega)\exp(-i\omega t)\right] \ . \end{aligned} \tag{1.10}$$

The average energy flux density of a harmonic monochromatic electromagnetic (EM) wave is given by the time-averaged Poynting vector (averaged over a full cycle $T = 2\pi/\omega$). By using Eqs. 1.10, we obtain

$$\langle \mathbf{S}(\mathbf{r}) \rangle = \frac{1}{2}\mathrm{Re}\left[\mathbf{E}(\mathbf{r},\omega) \times \mathbf{H}^*(\mathbf{r},\omega)\right] \ . \tag{1.11}$$

Moreover, from Maxwell's equations in media without sources and making use of the vector identity A.10, we have $\nabla \cdot [\mathbf{E} \times \mathbf{H}^*] = i\omega[\mathbf{H}^* \cdot \mathbf{B} - \mathbf{E} \cdot \mathbf{D}^*]$. By integrating the averaged power, $\nabla \cdot \langle \mathbf{S} \rangle$, over a volume V enclosed by a surface $A(V)$ and applying the Gauss divergence theorem, we obtain

$$\int_{A(V)} d^2 r \widehat{\mathbf{n}} \cdot \langle \mathbf{S}(\mathbf{r}) \rangle = -\frac{\omega}{2} \int_V d^3 r \ \mathrm{Im}[\mathbf{H}^*(\mathbf{r},\omega) \cdot \mathbf{B}(\mathbf{r},\omega) - \mathbf{E}(\mathbf{r},\omega) \cdot \mathbf{D}^*(\mathbf{r},\omega)] \ , \tag{1.12}$$

where $\widehat{n}$ is the outward pointing unit normal vector. In the case of losses, the power flowing into the volume is lower than the out coming power. Therefore the left-hand side of Eq. 1.12 is $\leqslant 0$, where equality holds when there are no losses. Consequently, we have

$$\mathrm{Im}[\mathbf{H}^*(\mathbf{r},\omega) \cdot \mathbf{B}(\mathbf{r},\omega) - \mathbf{E}(\mathbf{r},\omega) \cdot \mathbf{D}^*(\mathbf{r},\omega)] \geqslant 0 \ . \tag{1.13}$$

By writing $2\mathrm{Im}z = i(z^* - z)$ and making use of the constitutive equations 1.7, the relation 1.13 leads to the condition

$$(\mathbf{E}^*, \mathbf{H}^*) \left\{ i \left[\begin{pmatrix} \boldsymbol{\epsilon} & \mathbf{0} \\ \mathbf{0} & \boldsymbol{\mu} \end{pmatrix}^\dagger - \begin{pmatrix} \boldsymbol{\epsilon} & \mathbf{0} \\ \mathbf{0} & \boldsymbol{\mu} \end{pmatrix} \right] \right\} \begin{pmatrix} \mathbf{E} \\ \mathbf{B} \end{pmatrix} \geq 0 \ , \tag{1.14}$$

where with † we denote adjoint matrix. Therefore, in lossy media without sources, the Hermitian matrix 1.14 should be positive (positive eigenvalues). Consequently, in isotropic homogeneous media holds: $\mathrm{Im}\epsilon \geq 0$ and $\mathrm{Im}\mu \geq 0$.

1.3 Solutions to wave equation in simple isotropic media

Maxwell's equations for a harmonic monochromatic field in a simple isotropic medium without sources and currents, described by the constitutive relations $\mathbf{D} = \epsilon_0 \epsilon \mathbf{E}$ and $\mathbf{B} = \mu_0 \mu \mathbf{H}$, read $\nabla \cdot \mathbf{B} = 0$, $\nabla \cdot \mathbf{D} = 0$, $\nabla \times \mathbf{E} = i\omega \mathbf{B}$, $\nabla \times \mathbf{H} = -i\omega \mathbf{D}$. By applying the vector identity A.6, we obtain the wave equation for the electric field

$$\nabla^2 \mathbf{E}(\mathbf{r}) + q^2 \mathbf{E}(\mathbf{r}) = 0 \ , \tag{1.15}$$

where $q = \omega\sqrt{\epsilon\mu}/c$. Plane waves constitute a complete set of solutions to Eq. 1.15

$$\mathbf{E}_{\mathbf{q}\mathrm{p}}(\mathbf{r}) = \mathbf{E}_0(\mathbf{q}) \exp(i\mathbf{q} \cdot \mathbf{r}) \ , \tag{1.16}$$

with $\mathbf{E}_0(\mathbf{q}) = E_0(\mathbf{q})\ \widehat{\mathbf{e}}_\mathrm{p}(\mathbf{q})$, where $\widehat{\mathbf{e}}_\mathrm{p}(\mathbf{q})$, $\mathrm{p} = 0, 1, 2$ denote the radial, polar and azimuthal unit vector, respectively, for a given wave vector $\mathbf{q}$ and define the polarization (Fig. 1.1). It is worth noting that the longitudinal wave $\widehat{\mathbf{e}}_0(\mathbf{q}) = \widehat{\mathbf{q}}$ represents a solution only if $\omega = 0$, or $\epsilon\mu = 0$ and therefore can not describe wave propagation. The magnetic field is given from the corresponding electric field through the Maxwell equation $\nabla \times \mathbf{E} = i\omega \mathbf{B}$.

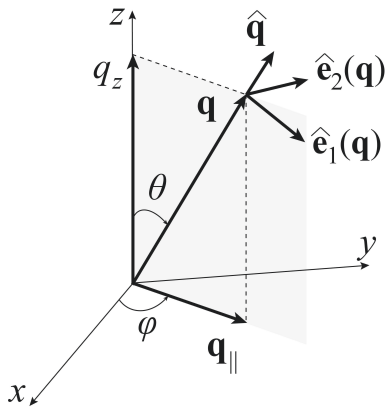

Figure 1.1: Wavevector analysis in the coordinate system.

Alternatively, the solutions to wave equation 1.15 can be developed in a complete basis of vector spherical waves for given q. The basis consists of: (a) Longitudinal wave functions ($\nabla \times \mathbf{F}_{Llm} = 0$)

$$\mathbf{F}_{Llm}(\mathbf{r}) = \frac{1}{q}\nabla \left[f_l(qr) Y_{lm}(\widehat{\mathbf{r}}) \right] \ , \quad l = 0, 1, 2, \dots \ ; \ m = -l, -l+1, \dots, l, \tag{1.17}$$

where Y_{lm} are the usual spherical harmonics (see appendix B) and f_l may be any linear combination of the spherical Bessel function, j_l, and the spherical Hankel function h_l^+ (see appendix C).
(b) Transverse (divergenceless) spherical wave functions ($\nabla \cdot \mathbf{F}_{Hlm} = 0$, $\nabla \cdot \mathbf{F}_{Elm} = 0$)

$$\mathbf{F}_{Hlm}(\mathbf{r}) = f_l(qr)\mathbf{X}_{lm}(\widehat{\mathbf{r}}) \ , \quad l = 1, 2, \dots \ ; \ m = -l, -l+1, \dots, l, \tag{1.18}$$

and

$$\mathbf{F}_{Elm}(\mathbf{r}) = \frac{i}{q}\nabla \times f_l(qr)\mathbf{X}_{lm}(\widehat{\mathbf{r}}) \ , \quad l = 1, 2, \dots \ ; \ m = -l, -l+1, \dots, l, \tag{1.19}$$

where $\mathbf{X}_{lm}$ are the vector spherical harmonics. The above vector spherical wave functions constitute a complete basis set for the expansion of any vector field in the sense of Helmholtz theorem. The vector spherical wave functions satisfy the following differential equations

$$\begin{aligned}
&\nabla \cdot \mathbf{F}_{Llm}(\mathbf{r}) = -q f_l(qr) Y_{lm}(\widehat{\mathbf{r}}) \\
&\nabla \times \mathbf{F}_{Hlm}(\mathbf{r}) = -iq\mathbf{F}_{Elm}(\mathbf{r}) \\
&\nabla \times \mathbf{F}_{Elm}(\mathbf{r}) = iq\mathbf{F}_{Hlm}(\mathbf{r}) \\
&\nabla \times \nabla \times \mathbf{F}_{Hlm}(\mathbf{r}) = q^2\mathbf{F}_{Hlm}(\mathbf{r}) \\
&\nabla \times \nabla \times \mathbf{F}_{Elm}(\mathbf{r}) = q^2\mathbf{F}_{Elm}(\mathbf{r}) \ ,
\end{aligned} \tag{1.20}$$

and the orthogonality relations

$$\begin{aligned}
&\int_0^{2\pi} d\phi \int_0^{\pi} d\theta \sin\theta \ \overline{\mathbf{F}}_{Hlm}(\mathbf{r}) \cdot \mathbf{F}_{El'm'}(\mathbf{r}) = 0 \\
&\int_0^{2\pi} d\phi \int_0^{\pi} d\theta \sin\theta \ \overline{\mathbf{F}}_{Llm}(\mathbf{r}) \cdot \mathbf{F}_{Hl'm'}(\mathbf{r}) = 0 \\
&\int_0^{2\pi} d\phi \int_0^{\pi} d\theta \sin\theta \ \overline{\mathbf{F}}_{Hlm}(\mathbf{r}) \cdot \mathbf{F}_{Hl'm'}(\mathbf{r}) = f_l^2(qr)\delta_{ll'}\delta_{mm'} \\
&\int_0^{2\pi} d\phi \int_0^{\pi} d\theta \sin\theta \ \overline{\mathbf{F}}_{Elm}(\mathbf{r}) \cdot \mathbf{F}_{El'm'}(\mathbf{r}) = \frac{1}{2l+1}[(l+1)f_{l-1}^2(qr) + l f_{l+1}^2(qr)]\delta_{ll'}\delta_{mm'} \\
&\int_0^{2\pi} d\phi \int_0^{\pi} d\theta \sin\theta \ \overline{\mathbf{F}}_{Llm}(\mathbf{r}) \cdot \mathbf{F}_{Ll'm'}(\mathbf{r}) = \frac{1}{2l+1}[l f_{l-1}^2(qr) + (l+1)f_{l+1}^2(qr)]\delta_{ll'}\delta_{mm'} \\
&\int_0^{2\pi} d\phi \int_0^{\pi} d\theta \sin\theta \ \overline{\mathbf{F}}_{Llm}(\mathbf{r}) \cdot \mathbf{F}_{El'm'}(\mathbf{r}) = \frac{\psi_l}{2l+1}[f_{l+1}^2(qr) - f_{l-1}^2(qr)]\delta_{ll'}\delta_{mm'} \ ,
\end{aligned} \tag{1.21}$$

where $\psi_l = \sqrt{l(l+1)}$ and the bar above a vector spherical wave function denotes the complex conjugate over the angular part. Due to the relation $\nabla \cdot \mathbf{E} = 0$, the electric field can be expanded in the basis of the traverse wave functions $\mathbf{F}_{Hlm}$ and $\mathbf{F}_{Elm}$ only and does not involve $\mathbf{F}_{Llm}$. Therefore the solution of Eq. 1.15 takes the form

$$\mathbf{E}(\mathbf{r}) = \sum_{l=1}^{\infty} \sum_{m=-l}^{l} \left[a_{Hlm} \mathbf{F}_{Hlm}(\mathbf{r}) + a_{Elm} \mathbf{F}_{Elm}(\mathbf{r}) \right] \ , \tag{1.22}$$

where a_{Hlm} and a_{Elm} are the associated spherical-wave amplitudes. We write the (traverse) plane wave (1.16) as

$$\mathbf{E}_{\mathbf{q}\mathrm{p}}(\mathbf{r}) = \sum_{l=1}^{\infty} \sum_{m=-l}^{l} \left[a^0_{Hlm} j_l(qr) \mathbf{X}_{lm}(\widehat{\mathbf{r}}) + a^0_{Elm} \frac{i}{q} \nabla \times j_l(qr) \mathbf{X}_{lm}(\widehat{\mathbf{r}}) \right] \ , \tag{1.23}$$

because the field must be finite everywhere, thus, only regular vector spherical waves that involve j_l (appendix C) enter in the expansion of Eq. 1.23. We write the spherical-wave amplitudes in the form

$$a^0_{Plm} = \mathbf{A}^0_{Plm}(\widehat{\mathbf{q}}) \cdot \mathbf{E}_0(\mathbf{q}) \ , \tag{1.24}$$

where the vectors $\mathbf{A}^0_{Plm}$ are defined on the plane of $\widehat{\mathbf{e}}_1$, $\widehat{\mathbf{e}}_2$. By applying to Eq. 1.23 and making use of the expansion [2]

$$\exp(i\mathbf{q} \cdot \mathbf{r}) = 4\pi \sum_{lm} i^l j_l(qr) Y_{lm}(\widehat{\mathbf{r}}) Y^*_{lm}(\widehat{\mathbf{q}}) \ , \tag{1.25}$$

and the relations B, we obtain

$$\begin{aligned}
\mathbf{A}^0_{Hlm}(\widehat{\mathbf{q}}) &= \frac{4\pi i^l \, (-1)^{m+1}}{\psi_l} \\
&\times \Big\{ \Big[\alpha^m_l \cos\theta \, e^{i\phi} \, Y_{l-m-1}(\widehat{\mathbf{q}}) + m \sin\theta \, Y_{l-m}(\widehat{\mathbf{q}}) \\
&+ \alpha^{-m}_l \cos\theta \, e^{-i\phi} \, Y_{l-m+1}(\widehat{\mathbf{q}}) \Big] \widehat{\mathbf{e}}_1(\mathbf{q}) \\
&+ i \left[\alpha^m_l \, e^{i\phi} \, Y_{l-m-1}(\widehat{\mathbf{q}}) - \alpha^{-m}_l \, e^{-i\phi} \, Y_{l-m+1}(\widehat{\mathbf{q}}) \right] \widehat{\mathbf{e}}_2(\mathbf{q}) \Big\} \\
&= 4\pi i^l \, (-1)^{m+1} \, \mathbf{X}_{l-m}(\widehat{\mathbf{q}})
\end{aligned} \tag{1.26}$$

and

$$\begin{aligned}
\mathbf{A}^0_{Elm}(\widehat{\mathbf{q}}) &= \frac{4\pi i^l\,(-1)^{m+1}}{\psi_l} \\
&\times \left\{ i\left[\alpha_l^m\, e^{i\phi}\, Y_{l-m-1}(\widehat{\mathbf{q}}) - \alpha_l^{-m}\, e^{-i\phi}\, Y_{l-m+1}(\widehat{\mathbf{q}})\right]\widehat{\mathbf{e}}_1(\mathbf{q}) \right. \\
&- \left[\alpha_l^m \cos\theta\, e^{i\phi}\, Y_{l-m-1}(\widehat{\mathbf{q}}) + m\sin\theta\, Y_{l-m}(\widehat{\mathbf{q}}) \right. \\
&+ \left. \left. \alpha_l^{-m}\cos\theta\, e^{-i\phi}\, Y_{l-m+1}(\widehat{\mathbf{q}})\right]\widehat{\mathbf{e}}_2(\mathbf{q}) \right\} \\
&= 4\pi i^l\,(-1)^{m+1}\,\mathbf{X}_{l-m}(\widehat{\mathbf{q}})\times\widehat{\mathbf{q}}\ , \qquad (1.27)
\end{aligned}$$

where $\alpha_l^m = \left[\left(l-m\right)\left(l+m+1\right)\right]^{1/2}/2$, θ and ϕ are the angular variables of $\mathbf{q}$ while $\widehat{\mathbf{e}}_1$ and $\widehat{\mathbf{e}}_2$ are the polar and azimuthal unit vectors, respectively, normal to $\mathbf{q}$ in the spherical coordinate system (Fig. 1.1). It is worth noting that the wave vector, q_z, could be real or imaginary. In the second case, the $\cos\theta$ in the expressions of $Y_{lm}(\widehat{\mathbf{q}})$ (see appendix B) is replaced by the q_z/q.

CHAPTER 2

Scattering by a single scatterer

In this chapter, we study the light scattering properties for isotropic spherical and cylindrical scatterer. Scattering by single particles is described through quantities such as T matrix, scattering efficiency, differential scattering efficiency, and asymmetry parameter.

2.1 Scattering matrix for a single sphere

We assume a homogeneous isotropic sphere characterized by scalar electromagnetic (EM) parameters ϵ_1 and μ_1. The scatterer is centered at the origin of coordinates in a homogeneous and isotropic host medium (ϵ_h, μ_h) and illuminated by a monochromatic harmonic plane EM wave of angular frequency ω. We expand the EM field in transverse vector spherical waves which are given by Eqs. 1.18 and 1.19, with $f_l = j_l$ because the field must be finite everywhere:

$$\begin{aligned}\mathbf{E}_0(\mathbf{r}) &= \sum_{l=1}^{\infty}\sum_{m=-l}^{l}\left[a^0_{Hlm} j_l(q_h r)\mathbf{X}_{lm}(\widehat{\mathbf{r}}) + \frac{i}{q_h} a^0_{Elm}\nabla\times j_l(q_h r)\mathbf{X}_{lm}(\widehat{\mathbf{r}})\right] \\ \mathbf{H}_0(\mathbf{r}) &= Z_h^{-1}\sum_{l=1}^{\infty}\sum_{m=-l}^{l}\left[a^0_{Elm} j_l(q_h r)\mathbf{X}_{lm}(\widehat{\mathbf{r}}) - \frac{i}{q_h} a^0_{Hlm}\nabla\times j_l(q_h r)\mathbf{X}_{lm}(\widehat{\mathbf{r}})\right] ,\end{aligned} \tag{2.1}$$

where $q_h = \omega\sqrt{\epsilon_h\mu_h}/c$, $Z_h = \sqrt{\mu_0\mu_h/(\epsilon_0\epsilon_h)}$, while a^0_{Hlm} and a^0_{Elm} are the associated spherical-wave amplitudes with dimensions of electric field. The multipole expansion of the scattered field consists of transverse spherical waves with $f_l = h_l^+$, because of the asymptotic form of the outgoing spherical waves: $h_l^+(x) \approx (-i)^l \exp(ix)/ix$, for $x \to \infty$.

Therefore, we have

$$\begin{aligned}\mathbf{E}_{\rm sc}(\mathbf{r}) &= \sum_{l=1}^{\infty}\sum_{m=-l}^{l}\left[a^{+}_{Hlm}h^{+}_{l}(q_h r)\mathbf{X}_{lm}(\widehat{\mathbf{r}}) + \frac{i}{q_h}a^{+}_{Elm}\nabla\times h^{+}_{l}(q_h r)\mathbf{X}_{lm}(\widehat{\mathbf{r}})\right]\\ \mathbf{H}_{\rm sc}(\mathbf{r}) &= Z_h^{-1}\sum_{l=1}^{\infty}\sum_{m=-l}^{l}\left[a^{+}_{Elm}h^{+}_{l}(q_h r)\mathbf{X}_{lm}(\widehat{\mathbf{r}}) - \frac{i}{q_h}a^{+}_{Hlm}\nabla\times h^{+}_{l}(q_h r)\mathbf{X}_{lm}(\widehat{\mathbf{r}})\right]\ .\end{aligned} \tag{2.2}$$

The field inside the sphere consists of only regular vector spherical waves

$$\begin{aligned}\mathbf{E}_{\rm in}(\mathbf{r}) &= \sum_{l=1}^{\infty}\sum_{m=-l}^{l}\left[a^{\rm in}_{Hlm}j_l(q_1 r)\mathbf{X}_{lm}(\widehat{\mathbf{r}}) + \frac{i}{q_1}a^{\rm in}_{Elm}\nabla\times j_l(q_1 r)\mathbf{X}_{lm}(\widehat{\mathbf{r}})\right]\\ \mathbf{H}_{\rm in}(\mathbf{r}) &= Z_1^{-1}\sum_{l=1}^{\infty}\sum_{m=-l}^{l}\left[a^{\rm in}_{Elm}j_l(q_1 r)\mathbf{X}_{lm}(\widehat{\mathbf{r}}) - \frac{i}{q_1}a^{\rm in}_{Hlm}\nabla\times j_l(q_1 r)\mathbf{X}_{lm}(\widehat{\mathbf{r}})\right]\ ,\end{aligned} \tag{2.3}$$

where $q_1 = \omega\sqrt{\epsilon_1\mu_1}/c$ and $Z_1 = \sqrt{\mu_0\mu_1/(\epsilon_0\epsilon_1)}$. We can relate the coefficients of the irregular spherical waves a^{+}_{Plm}, $P = H, E$, to those of the corresponding regular waves, through the scattering T matrix,

$$a^{+}_{Plm} = \sum_{P'l'm'} T_{Plm;P'l'm'}a^{0}_{P'l'm'}\ , \tag{2.4}$$

where in the general case is non-diagonal. For scatterers with spherical symmetry, the T matrix is diagonal with respect to P and l and independent to m. Indeed, for a homogeneous isotropic sphere of radius S, by applying the boundary conditions of continuity of the tangential components of the fields at the interface $r = S$

$$\begin{aligned}\mathbf{X}^{*}_{lm}(\widehat{\mathbf{r}})\cdot\mathbf{E}_{\rm in}(\mathbf{r}) &= \mathbf{X}^{*}_{lm}(\widehat{\mathbf{r}})\cdot\mathbf{E}_{\rm out}(\mathbf{r})\\ \left[\widehat{\mathbf{r}}\times\mathbf{X}^{*}_{lm}(\widehat{\mathbf{r}})\right]\cdot\mathbf{E}_{\rm in}(\mathbf{r}) &= \left[\widehat{\mathbf{r}}\times\mathbf{X}^{*}_{lm}(\widehat{\mathbf{r}})\right]\cdot\mathbf{E}_{\rm out}(\mathbf{r})\\ \mathbf{X}^{*}_{lm}(\widehat{\mathbf{r}})\cdot\mathbf{H}_{\rm in}(\mathbf{r}) &= \mathbf{X}^{*}_{lm}\cdot\mathbf{H}_{\rm out}(\mathbf{r})\\ \left[\widehat{\mathbf{r}}\times\mathbf{X}^{*}_{lm}(\widehat{\mathbf{r}})\right]\cdot\mathbf{H}_{\rm in}(\mathbf{r}) &= \left[\widehat{\mathbf{r}}\times\mathbf{X}^{*}_{lm}(\widehat{\mathbf{r}})\right]\cdot\mathbf{H}_{\rm out}(\mathbf{r})\ ,\end{aligned} \tag{2.5}$$

with $\mathbf{E}_{\rm out}(\mathbf{r}) = \mathbf{E}_0(\mathbf{r}) + \mathbf{E}_{\rm sc}(\mathbf{r})$ and $\mathbf{H}_{\rm out}(\mathbf{r}) = \mathbf{H}_0(\mathbf{r}) + \mathbf{H}_{\rm sc}(\mathbf{r})$, we obtain

$$a^{+}_{Plm} = T_{Pl}\ a^{0}_{Plm}\ , \tag{2.6}$$

where

$$T_{Hl} = -\frac{j_l(q_1 S)\left[x j_l(x)\right]'_{q_h S}\mu_1 - j_l(q_h S)\left[x j_l(x)\right]'_{q_1 S}\mu_h}{j_l(q_1 S)\left[x h_l^+(x)\right]'_{q_h S}\mu_1 - h_l^+(q_h S)\left[x j_l(x)\right]'_{q_1 S}\mu_h}$$
$$T_{El} = -\frac{j_l(q_1 S)\left[x j_l(x)\right]'_{q_h S}\epsilon_1 - j_l(q_h S)\left[x j_l(x)\right]'_{q_1 S}\epsilon_h}{j_l(q_1 S)\left[x h_l^+(x)\right]'_{q_h S}\epsilon_1 - h_l^+(q_h S)\left[x j_l(x)\right]'_{q_1 S}\epsilon_h} \,. \tag{2.7}$$

Accordingly, we have

$$a^{\text{in}}_{Plm} = R_{Pl}\; a^0_{Plm} \,, \tag{2.8}$$

where

$$R_{Hl} = \frac{i\mu_1/(q_h S)}{j_l(q_1 S)\left[x h_l^+(x)\right]'_{q_h S}\mu_1 - h_l^+(q_h S)\left[x j_l(x)\right]'_{q_1 S}\mu_h}$$
$$R_{El} = \frac{i\epsilon_1\mu_1/(\mu_h q_1 S)}{j_l(q_1 S)\left[x h_l^+(x)\right]'_{q_h S}\epsilon_1 - h_l^+(q_h S)\left[x j_l(x)\right]'_{q_1 S}\epsilon_h} \,. \tag{2.9}$$

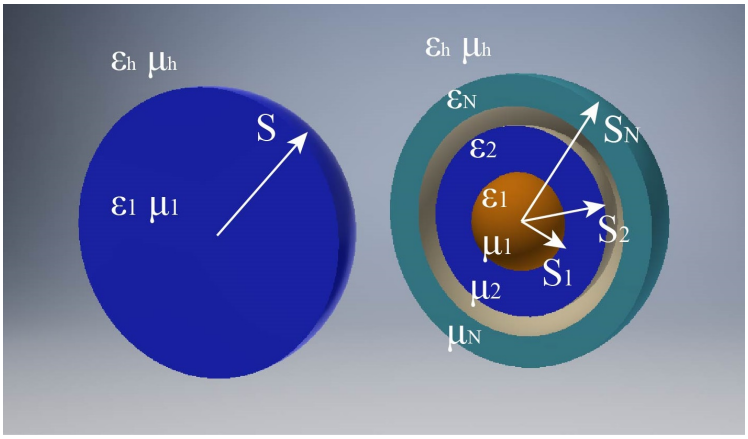

Figure 2.1: Homogenous and multilayered sphere.

If we apply the boundary conditions of continuity of the fields, Eq. 2.5, at the consecutive interfaces for a multilayered sphere comprised of $n = 1, 2, \ldots, N$ concentric spherical shells of radius S_n ($S_N \equiv S$) and characterized by EM parameters ϵ_n and μ_n (see Fig. 2.1), we obtain that the elements of the scattering matrix for a sphere with n first shells embedded in a medium with permittivity ϵ_{n+1} and permeability μ_{n+1}, $T^{(n)}_{Pl}$, are related to the elements of the scattering matrix of a sphere with $n-1$ first shells embedded in a medium with permittivity ϵ_n and permeability μ_n, $T^{(n-1)}_{Pl}$, through the

relation:

$$T_{Pl}^{(n)} = -\frac{\mathrm{A}_{Pl}^{(n,n+1)} + T_{Pl}^{(n-1)}\ \mathrm{B}_{Pl}^{(n,n+1)}}{\Gamma_{Pl}^{(n,n+1)} + T_{Pl}^{(n-1)}\ \Delta_{Pl}^{(n,n+1)}}\ ,\quad P = H, E\ , \tag{2.10}$$

where

$$\begin{aligned}
\mathrm{A}_{Hl}^{(n,n+1)} &= j_l(q_n S)\left[x j_l(x)\right]'_{q_{n+1}S}\mu_n - j_l(q_{n+1}S)\left[x j_l(x)\right]'_{q_n S}\mu_{n+1}\\
\mathrm{B}_{Hl}^{(n,n+1)} &= h_l^+(q_n S)\left[x j_l(x)\right]'_{q_{n+1}S}\mu_n - j_l(q_{n+1}S)\left[x h_l^+(x)\right]'_{q_n S}\mu_{n+1}\\
\Gamma_{Hl}^{(n,n+1)} &= j_l(q_n S)\left[x h_l^+(x)\right]'_{q_{n+1}S}\mu_n - h_l^+(q_{n+1}S)\left[x j_l(x)\right]'_{q_n S}\mu_{n+1}\\
\Delta_{Hl}^{(n,n+1)} &= h_l^+(q_n S)\left[x h_l^+(x)\right]'_{q_{n+1}S}\mu_n - h_l^+(q_{n+1}S)\left[x h_l^+(x)\right]'_{q_n S}\mu_{n+1}\ .
\end{aligned} \tag{2.11}$$

The same expression holds for the elements $T_{El}^{(n)}$, where the index of polarization is E instead of H and the permittivity ϵ_n, ϵ_{n+1} is replaced by the permeability μ_n, μ_{n+1}, respectively. The total scattering matrix $T_{Pl} \equiv T_{Pl}^{(N)}$ of the multilayered sphere is calculated for $n = N$ and $\epsilon_{N+1} = \epsilon_h$, $\mu_{N+1} = \mu_h$. Accordingly, for the matrix R we have

$$\begin{aligned}
R_{Hl}^{(n)} &= \frac{i\mu_n/(q_{(n+1)}S_n)}{\Gamma_{Hl}^{(n,n+1)} + T_{Hl}^{(n-1)}\ \Delta_{Hl}^{(n,n+1)}}\\
R_{El}^{(n)} &= \frac{i\epsilon_n\mu_n/(\mu_{(n+1)}q_n S_n)}{\Gamma_{El}^{(n,n+1)} + T_{El}^{(n-1)}\ \Delta_{El}^{(n,n+1)}}\ .
\end{aligned} \tag{2.12}$$

2.2 Scattered power by a single sphere

Light scattering by a sphere is usually described in terms of power that is scattered and absorbed by the particle. We define the scattering or absorption efficiency as the ratio of the scattered or absorbed light power to the incident light power through a circular section of area πS^2. In the case of a monochromatic harmonic wave, the averaged-Poynting vector over a period is given by Eq. 1.11 and the mean average of the power through a surface A, by making use of the divergence Gauss theorem (A.13), reads

$$P = \int_A d^2r\ \widehat{\mathbf{n}} \cdot \langle \mathbf{S}(\mathbf{r}) \rangle\ . \tag{2.13}$$

The average energy flux density, normally to the propagation direction, for an incident plane wave (Eq. 1.16) takes the form

$$\langle \mathbf{S}_0 \rangle \cdot \widehat{\mathbf{q}} = \frac{1}{2Z_h}\left|E_0\right|^2\ . \tag{2.14}$$

The total scattered light power is given by the integral of the above time-averaged Poynting vector over a spherical surface A (in the far-field zone) which encloses the

particle. By applying Eq. 2.2, and appendix B and C, we obtain

$$P_{\rm sc} = \frac{1}{2}{\rm Re}\int_A d^2r\ \widehat{\mathbf{r}}\cdot\left[\mathbf{E}_{\rm sc}(\mathbf{r})\times\mathbf{H}^*_{\rm sc}(\mathbf{r})\right] = \frac{1}{2Z_h q_h^2}\sum_{Plm}\left|a^+_{Plm}\right|^2\ . \tag{2.15}$$

Due to the energy conservation, the absorbed power is equal to the total power flowing out of a surface A:

$$P_{\rm out} = \frac{1}{2}{\rm Re}\int_A d^2r\ \widehat{\mathbf{r}}\cdot\left[\mathbf{E}_{\rm out}(\mathbf{r})\times\mathbf{H}^*_{\rm out}(\mathbf{r})\right] \equiv P_0 + P_{\rm sc} - P_{\rm ext}\ , \tag{2.16}$$

where

$$P_0 = \frac{1}{2}{\rm Re}\int_A d^2r\ \widehat{\mathbf{r}}\cdot\left[\mathbf{E}_0(\mathbf{r})\times\mathbf{H}^*_0(\mathbf{r})\right] = 0 \tag{2.17}$$

and

$$\begin{aligned} P_{\rm ext} &= -\frac{1}{2}{\rm Re}\int_A d^2r\ \widehat{\mathbf{r}}\cdot\left[\mathbf{E}_0(\mathbf{r})\times\mathbf{H}^*_{\rm sc}(\mathbf{r}) + \mathbf{E}_{\rm sc}(\mathbf{r})\times\mathbf{H}^*_0(\mathbf{r})\right] \\ &= -\frac{1}{2Z_h q_h^2}\sum_{Plm}{\rm Re}\left(a^{0*}_{Plm}a^+_{Plm}\right)\ , \end{aligned} \tag{2.18}$$

is the power related to the interference between the incident and scattered field and is called extinction energy. Energy conservation requires $P_{\rm abs} = -P_{\rm out} = P_{\rm ext} - P_{\rm sc}$ and therefore the extinction energy describes the total energy which is supplied from the source of the EM wave to the particle. By applying Eqs. 2.4 and 1.24, we have

$$\begin{aligned} P_{\rm sc} &= \frac{1}{2Z_h q_h^2}\sum_{Plm}\left|\sum_{P'l'm'}T_{Plm;P'l'm'}A^0_{P'l'm';{\rm p}}\right|^2|E_0|^2 \\ P_{\rm ext} &= -\frac{1}{2Z_h q_h^2}{\rm Re}\sum_{Plm}\left(A^0_{Plm;{\rm p}}\right)^*\sum_{P'l'm'}T_{Plm;P'l'm'}A^0_{P'l'm';{\rm p}}|E_0|^2\ , \end{aligned} \tag{2.19}$$

where the index p denotes the polarization of the incident wave (p $= 1, 2$ for TM and TE polarization, respectively). It is worth noting that if the scatterers do not exhibit spherical symmetry, the cross section depends on the polarization and the propagation direction of the incident wave. We define the scattering and extinction efficiency for spherical scatterers as the ratio of the corresponding light power, $Q = P/P_0$, given by Eqs. 2.15 and 2.18, respectively, to the incident light power, $P_0 = \pi S^2|E_0|^2/(2Z_h)$, through a circular section of area. By making use of the relations 1.24, 1.26, 1.27 and B.8, we obtain

$$\begin{aligned} Q_{\rm sc} &= \frac{2}{x^2}\sum_{l=1}^{\infty}(2l+1)(|a_l|^2+|b_l|^2) \\ Q_{\rm ext} &= -\frac{2}{x^2}\sum_{l=1}^{\infty}\left(2l+1\right){\rm Re}\left(a_l+b_l\right)\ , \end{aligned} \tag{2.20}$$

where $x = q_h S$ is the size parameter and $a_l = T_{El}, b_l = T_{Hl}$ denote the Mie scattering coefficients and represent the electric and magnetic moments of multipole sources located at the origin. Another important quantity is the backscattering efficiency of a spherical scatterer:

$$Q_{\mathrm{b}} = \frac{1}{x^2}\left|\sum_{l=1}^{\infty}(2l+1)(-1)^n(a_l - b_l)\right|^2 . \tag{2.21}$$

The backscattering efficiency is related to the fraction of the energy scattered in the backward direction ($\theta = 180°$) and depends on the terms $(a_l - b_l)$, which indicate the interference between the electric and magnetic moment of the same order in the backward scattering direction.

Accordingly, the forward scattering efficiency for a spherical scatterer reads

$$Q_{\mathrm{f}} = \frac{1}{x^2}\left|\sum_{l=1}^{\infty}(2l+1)(a_l + b_l)\right|^2 , \tag{2.22}$$

and is related to the fraction of the energy scattered in the forward direction ($\theta = 0°$). A zero backward scattering is expected at wavelengths where $a_l = b_l$, while a minimum forward scattering occurs at wavelengths where $a_l = -b_l$, for all l (Kerker conditions).

The analytical expression for the average cosine of the scattering angle, the so-called asymmetry parameter g is given by [3]

$$\begin{aligned} g = \frac{4}{Q_{\mathrm{sc}}x^2}\sum_{l=1}^{\infty}\Bigg[&\frac{l(l+2)}{l+1}\mathrm{Re}\left(a_l a_{l+1}^* + b_l b_{l+1}^*\right) \\ &+ \frac{2l+1}{l(l+1)}\mathrm{Re}\left(a_l b_l^*\right)\Bigg] , \end{aligned} \tag{2.23}$$

where the terms $\mathrm{Re}\left(a_l a_{l+1}^* + b_l b_{l+1}^*\right)$ indicate the interference between moments of same type and different order while the terms $\mathrm{Re}\left(a_l b_l^*\right)$ represent the interference between moments of different type and same order.

From multiple-scattering theory, it follows that for a dilute suspension of scatterers, the transport mean free path l_t is related to the extinction mean free path l_{ext} through

$$\frac{l_{\mathrm{t}}}{l_{\mathrm{ext}}} = \frac{Q_{\mathrm{ext}}}{Q_{\mathrm{ext}} - Q_{\mathrm{sca}}g} , \tag{2.24}$$

Therefore, for negative asymmetry parameter $g < 0$, a peculiar regime occurs, where the extinction mean free path is longer than the transport mean free path $l_{\mathrm{ext}} > l_{\mathrm{t}}$.

2.3 Scattering by an infinite cylinder

We assume a homogeneous isotropic infinite cylinder characterized by scalar EM parameters ϵ_1 and μ_1. The scatterer is centered at the origin of coordinates in a homogeneous

and isotropic host medium characterized by ϵ_h and μ_h and is illuminated by a monochromatic harmonic plane EM wave of angular frequency ω, perpendicularly to the cylinders axis. The vector cylindrical harmonics for perpendicular incidence are [4]

$$\begin{aligned} \mathbf{M}_{lq}^{Z}(r,\phi) &= \left(il\frac{Z_l(qr)}{qr}\widehat{\mathbf{r}} - Z_l'(qr)\widehat{\boldsymbol{\phi}} \right) qe^{il\phi} \\ \mathbf{N}_{lq}^{Z}(r,\phi) &= \frac{1}{q}\nabla \times \mathbf{M}_{lq}^{Z}(qr) = Z_l(qr)e^{il\phi}\widehat{\boldsymbol{\phi}} \ , \end{aligned} \tag{2.25}$$

where $\widehat{\mathbf{r}} = (\cos\phi, \sin\phi, 0)$, $\widehat{\boldsymbol{\phi}}(-\sin\phi, \cos\phi, 0)$, $\widehat{\boldsymbol{z}} = (0,0,1)$ and $q = \sqrt{\epsilon}\omega/c$. Z_l may be any of Bessel functions of first J_l or second Y_l kind as well as a linear combination of them $H_l = J_l + iY_l$ and $H_l^- = J_l - iY_l$ (Hankel function of first or second kind), while the prime indicates differentiation with respect to the argument. We expand the EM field, inside the cylinder and the surrounding medium, in vector cylindrical harmonics [3]

$$\begin{aligned} \mathbf{E}_{\text{in}}(r,\phi) &= \frac{1}{q_1}\sum_{l=-\infty}^{\infty}(-i)^l\left(A_l\mathbf{M}_{lq_1}^{J} + B_l\mathbf{N}_{lq_1}^{J}\right) \\ \mathbf{E}_{\text{sc}}(r,\phi) &= \frac{1}{q_h}\sum_{l=-\infty}^{\infty}(-i)^l\left(C_l\mathbf{M}_{lq_h}^{H^+} + D_l\mathbf{N}_{lq_h}^{H^+}\right) \\ \mathbf{E}_{\text{out}} &= \mathbf{E}_0 + \mathbf{E}_{\text{sc}} \ . \end{aligned} \tag{2.26}$$

The incident field $\mathbf{E}_0$ for the s polarization (electric field parallel to the cylinder axis) is given by

$$\mathbf{E}_0^s(r,\phi) = \widehat{\boldsymbol{z}}e^{-iq_h r\cos\phi} \ , \tag{2.27}$$

whereas for the p polarization reads

$$\mathbf{E}_0^p(r,\phi) = (\widehat{\mathbf{r}}\sin\phi + \widehat{\boldsymbol{\phi}}\cos\phi)e^{-iq_h r\cos\phi} \ . \tag{2.28}$$

By making use of the fourth Maxwell equation, we acquire the corresponding magnetic fields. In order to obtain the scattering coefficients, we apply the continuity conditions on the boundary of the cylinder $r = S$.

For the s polarization we have

$$D_l^s = \frac{J_l(q_1S)J_l'(q_hS) - \sqrt{\frac{\epsilon_1\mu_1}{\epsilon_h\mu_h}}J_l(q_hS)J_l'(q_1S)}{J_l(q_1S)H_l'(q_hS) - \sqrt{\frac{\epsilon_1\mu_1}{\epsilon_h\mu_h}}J_l'(q_1S)H_l(q_hS)} \ , \tag{2.29}$$

whereas for the p polarization we obtain

$$C_l^p = i\frac{\sqrt{\frac{\epsilon_1\mu_1}{\epsilon_h\mu_h}}J_l(q_1S)J_l'(q_hS) - J_l(q_hS)J_l'(q_1S)}{\sqrt{\frac{\epsilon_1\mu_1}{\epsilon_h\mu_h}}J_l(q_1S)H_l'(q_hS) - J_l'(q_1S)H_l(q_hS)} \ . \tag{2.30}$$

In the case of a coated cylinder, where the shell is characterized by the EM parameters ϵ_2 and μ_2, the expansion of the EM field inside the shell reads [4]

$$\mathbf{E}_{\text{shell}}(r,\phi) = \frac{1}{q_2}\sum_{l=-\infty}^{\infty}(-i)^l\left(E_l\mathbf{M}_{lq_2}^J + F_l\mathbf{N}_{lq_2}^Y + G_l\mathbf{M}_{lq_2}^Y L_l\mathbf{N}_{lq_2}^J\right) . \tag{2.31}$$

By applying the continuity conditions again at the inner radius S_1 (core-shell) and the outer radius S (shell-medium), we obtain the scattering coefficients [4].

For the s polarization we have

$$D_{l,c}^s = \frac{K_l^1K_l^5 - K_l^3K_l^6}{K_l^1K_l^2 - K_l^3K_l^4} , \tag{2.32}$$

while for the p polarization we obtain

$$C_{l,c}^p = i\frac{W_l^1W_l^2 - W_l^3W_l^4}{W_l^3W_l^5 - W_l^1W_l^6} , \tag{2.33}$$

where

$$\begin{aligned}
K_l^1 &= \frac{\pi S_1}{2}[q_1J_l^{'}(q_1S_1)J_l(q_2S_1) - q_2J_l^{'}(q_2S_1)J_l(q_1S_1)]\\
K_l^2 &= q_hY_l(q_2S)H_l^{'}(q_hS) - q_2H_l(q_hS)Y_l^{'}(q_2S)\\
K_l^3 &= \frac{\pi S_1}{2}[q_1J_l^{'}(q_1S_1)Y_l(q_2S_1) - q_2Y_l^{'}(q_2S_1)J_l(q_1S_1)]\\
K_l^4 &= q_hJ_l(q_2S)H_l^{'}(q_hS) - q_2H_l(q_hS)J_l^{'}(q_2S)\\
K_l^5 &= q_2Y_l^{'}(q_2S)J_l(q_hS) - q_hJ_l^{'}(q_hS)Y_l(q_2S)\\
K_l^6 &= q_2J_l^{'}(q_2S)J_l(q_hS) - q_hJ_l^{'}(q_hS)J_l(q_2S)\\
W_l^1 &= \frac{\pi S_1}{2}[q_2J_l^{'}(q_1S_1)Y_l(q_2S_1) - q_1Y_l^{'}(q_2S_1)J_l(q_1S_1)]\\
W_l^2 &= q_hJ_l^{'}(q_2S)J_l(q_hS) - q_2J_l^{'}(q_hS)J_l(q_2S)\\
W_l^3 &= \frac{\pi S_1}{2}[q_2J_l^{'}(q_1S_1)J_l(q_2S_1) - q_1J_l^{'}(q_2S_1)J_l(q_1S_1)]\\
W_l^4 &= q_2Y_l^{'}(q_2S)J_l(q_hS) - q_hJ_l^{'}(q_hS)Y_l(q_2S)\\
W_l^5 &= q_2Y_l(q_2S)H_l^{'}(q_hS) - q_hH_l(q_hS)Y_l^{'}(q_2S)\\
W_l^6 &= q_2J_l(q_2S)H_l^{'}(q_hS) - q_hH_l(q_hS)J_l^{'}(q_2S) .
\end{aligned} \tag{2.34}$$

The scattering efficiency for an infinite cylindrical scatterer at normal incidence reads

$$Q_{\text{sc}}^{\text{s,p}} = \frac{2}{x}\left[|a_0^{\text{s,p}}|^2 + 2\sum_{l=1}^{\infty}|a_l^{\text{s,p}}|^2\right] , \tag{2.35}$$

where $a_l^{\text{s}} = D_l^{\text{s}}$ and $a_l^{\text{p}} = -iC_l^{\text{p}}$ for a homogeneous cylinder, while $a_l^{\text{s}} = D_{l,c}^{\text{s}}$ and $a_l^{\text{p}} =$

$-iC_{l,c}^{\mathrm{p}}$ for a coated cylinder. The associated differential scattering efficiency is given by

$$\frac{\partial Q_{\mathrm{sc}}^{\mathrm{s,p}}(\phi)}{\partial \phi} = \frac{2}{\pi x}\left| a_0^{\mathrm{s,p}} + 2\sum_{l=1}^{\infty} a_l^{\mathrm{s,p}} cos(n\theta)\right|^2 , \tag{2.36}$$

where $\theta = \pi - \phi$ is the scattering angle. The average cosine of the scattering angle defines [3, 5] the so-called asymmetry parameter g:

$$\begin{aligned} g^{\mathrm{s,p}} = \langle \cos(\theta) \rangle &= \frac{\int_0^{\pi} \frac{\partial Q_{\mathrm{sc}}^{\mathrm{s,p}}(\phi)}{\partial \phi} \cos(\theta) d\theta}{Q_{\mathrm{sc}}^{\mathrm{s,p}}} \\ &= \frac{4}{x Q_{\mathrm{sc}}^{\mathrm{s,p}}} \sum_{l=0}^{\infty} a_l^{\mathrm{s,p}} (a_{l+1}^{\mathrm{s,p}})^* . \end{aligned} \tag{2.37}$$

For isotropic scattering, the asymmetry parameter vanishes and for predominantly forward (backward) scattering the asymmetry parameter takes on positive (negative) values.

CHAPTER 3

The Discontinous Galerkin Time-Domain Method

In this chapter, we present the Discontinuous Galerkin Time-Domain method for the simulation of light propagation in complex nanophotonic structures. Furthermore, we introduce the Maxwell curl equations in conservation form, the boundary conditions and the material model in DGTD. Finally, we reveal the potential of the DGTD approach by simulating a nanostructure with experimentally relevant geometry.

3.1 Maxwell curl equations in conservation form and dimensionless units

The time evolution of the EM fields can be determined through the Maxwell curl equations

$$\begin{aligned} \mu(\mathbf{r})\partial_t \mathbf{H}(\mathbf{r},t) &= -\nabla \times \mathbf{E}(\mathbf{r},t) \\ \epsilon(\mathbf{r})\partial_t \mathbf{E}(\mathbf{r},t) &= \nabla \times \mathbf{H}(\mathbf{r},t) - \mathbf{j}(\mathbf{r},t) \ , \end{aligned} \tag{3.1}$$

where the vacuum electric permittivity and vacuum magnetic permeability have been absorbed into the EM fields:

$$\begin{aligned} \mathbf{E}^{'}(\mathbf{r},t^{'}) &= \mathbf{E}(\mathbf{r},t) \\ \mathbf{H}^{'}(\mathbf{r},t^{'}) &= \sqrt{\frac{\mu_0}{\epsilon_0}}\mathbf{H}(\mathbf{r},t) \\ t^{'} &= \frac{1}{\sqrt{\epsilon_0\mu_0}}t \\ c^{'} &= 1 \ . \end{aligned} \tag{3.2}$$

Therefore, the electric and magnetic field have the same unit, where for the time variable the new unit is length. The vacuum speed of light is dimensionless and equal to 1. Consequently, is straight forward to convert to dimensionless units by rescaling all fields by an arbitrary electric field amplitude E_0. Similarly, time and space variables convert to dimensionless units in the new system by rescaling them by an arbitrary length λ_0. It is worth noting that in Eqs. 3.1, we neglect all primes for notational convenience.

SI-Quantity	**Dimensionless units**
t_{SI}	$t = \frac{c_{SI}}{\lambda_0} t_{SI}$
λ_{SI}	$\lambda = \frac{1}{\lambda_0} \lambda_{SI}$
ω_{SI}	$\omega = \frac{\lambda_0}{c_{SI}} \omega_{SI}$
$\mathbf{j}_{SI}$	$\mathbf{j} = \frac{1}{E_0} \mathbf{j}_{SI}$
$\mathbf{E}_{SI}$	$\mathbf{E} = \mathbf{E}_{SI}/E_0$
$\mathbf{H}_{SI}$	$\mathbf{H} = \mathbf{H}_{SI}/E_0\sqrt{\epsilon_0/\mu_0}$

Table 3.1: Conversion from SI units to dimensionless units.

By introducing the material matrix

$$\overleftrightarrow{Q} = \begin{pmatrix} \epsilon(\mathbf{r}) & 0 \\ 0 & \mu(\mathbf{r}) \end{pmatrix}, \tag{3.3}$$

the six-dimensional state vector

$$\vec{q}(\mathbf{r}, t) = \begin{pmatrix} \mathbf{E}(\mathbf{r}, t) \\ \mathbf{H}(\mathbf{r}, t) \end{pmatrix}, \tag{3.4}$$

and the flux

$$\mathbf{F} = \begin{pmatrix} \vec{F}_x \\ \vec{F}_y \\ \vec{F}_z \end{pmatrix}, \tag{3.5}$$

where

$$\vec{F}_i(\vec{q}) = \begin{pmatrix} -\widehat{\mathbf{e}}_i \times \mathbf{H}(\mathbf{r},t) \\ \widehat{\mathbf{e}}_i \times \mathbf{E}(\mathbf{r},t) \end{pmatrix}, \tag{3.6}$$

we can reformulate Eq. 3.1 as the conservation law

$$\overleftrightarrow{Q}(\mathbf{r}) \cdot \partial_t \vec{q}(\mathbf{r},t) + \nabla \cdot \mathbf{F}(\vec{q}) = 0 \ . \tag{3.7}$$

If the divergence conditions of Maxwell equations are fulfilled for a given initial state ($\mathbf{E}(\mathbf{r},t_0)$ and $\mathbf{H}(\mathbf{r},t_0)$), they will be fulfilled for all future times [6, 7]. In DGTD method [7, 8], we compute field values all over the computational domain. The tessellation of the simulation volume consists of individual elements Δ of different types according to the system, e.g., triangles in 2D and tetrahedrons in 3D. It is worth noting that these elements have different sizes and shapes and therefore, the formed mesh is unstructured. Moreover, we can vary the accuracy by using more or fewer elements for different regions of the simulation volume, e.g., higher accuracy and therefore more elements at the interface of two different materials are needed, whereas for large homogeneous areas fewer elements are required. By considering a numerical approximation $\vec{q}_n$ to Eq. 3.7, we have:

$$\overleftrightarrow{Q}(\mathbf{r}) \cdot \partial_t \vec{q}_N(\mathbf{r},t) + \nabla \cdot \mathbf{F}(\vec{q}_N) = \mathbf{residual} \neq 0 \ . \tag{3.8}$$

Each component of the state vector $\vec{q}$ in each element can be expanded into Lagrange polynomials $L_i(\mathbf{r})$

$$\vec{q}^{\,\Delta}_{i,N}(\mathbf{r},t) = \sum_{j=1}^{n} \vec{q}^{\,\Delta}_{i,j}(t) \cdot L_j(\mathbf{r}) \equiv \vec{q}^{\,\Delta}_{i,j}(t) \cdot L_j(\mathbf{r}) \ , \tag{3.9}$$

where

$$L_i(\mathbf{r}_j) = \delta_{ij} = \begin{cases} 0 & \text{for } i \neq j \\ 1 & \text{for } i = j \ . \end{cases} \tag{3.10}$$

Therefore, the expansion coefficients correspond to the field values at the discretization points $\mathbf{r}_k$ (nodes):

$$\vec{q}^{\,\Delta}_{i,N}(\mathbf{r}_k,t) = \vec{q}^{\,\Delta}_{i,j}(t) \cdot L_j(\mathbf{r}_k) = \vec{q}^{\,\Delta}_{i,k}(t) \ . \tag{3.11}$$

Consequently, this DG method is called a nodal method. The Lagrange polynomials of

order p are given by [9]

$$L_i(\mathbf{r}) = \sum_{k,l,m=0}^{k+l+m\leqslant p} a_{k,l,m}^{(i)} x^k y^l z^m \ , \tag{3.12}$$

where $a_{k,l,m}^{(i)}$ are the expansion coefficients and

$$\begin{aligned} n &= p+1 && (1D) \\ n &= \frac{1}{2}(p+1)(p+2) && (2D) \\ n &= \frac{1}{6}(p+1)(p+2)(p+3) && (3D). \end{aligned}$$

The numerical approximation to Eq. 3.7 corresponds to an optimal solution that minimizes the residual. By applying the orthogonality condition of the residual and the expansion functions, we have

$$\begin{aligned} \int_{V_\Delta} \left[\overleftrightarrow{Q}(\mathbf{r}) \cdot \partial_t \vec{q}_N(\mathbf{r},t) + \nabla \cdot \mathbf{F}(\vec{q}_N(\mathbf{r},t)) \right] L_i(\mathbf{r}) d^3r = \\ \int_{V_\Delta} \mathbf{residual} \cdot L_i(\mathbf{r}) d^3r = 0 \ , \end{aligned} \tag{3.13}$$

where V_Δ is the volume of the element Δ. It is clear that Eq. 3.13 consists of only local field values in the element Δ. It is shown [6, 10] that the coupling to neighboring elements must fulfil the boundary conditions of continuity of the tangential components of the fields at the interface of the neighboring elements. By integrating Eq. 3.13 by parts

$$\int_{V_\Delta} \left[\overleftrightarrow{Q}(\mathbf{r}) \cdot \partial_t \vec{q}_N(\mathbf{r},t) L_i(\mathbf{r}) - \mathbf{F}(\vec{q}_N) \nabla \cdot L_i(\mathbf{r}) \right] d^3r = - \int_{\partial V_\Delta} \left(\widehat{\mathbf{n}} \cdot \mathbf{F}(\vec{q}_N) \right) L_i(\mathbf{r}) d^2r \ , \tag{3.14}$$

where ∂V_Δ denotes the element's surface and $\widehat{\mathbf{n}}$ is the outward pointing unit normal vector. By replacing the flux $\mathbf{F}(\vec{q}_N(\mathbf{r},t))$ on the right-hand side of Eq. 3.14 by the numerical flux $\mathbf{F}^*(\vec{q}_N(\mathbf{r},t))$ and then undoing the integration by parts, we obtain

$$\begin{aligned} \int_{V_\Delta} \left[\overleftrightarrow{Q}(\mathbf{r}) \cdot \partial_t \vec{q}_N(\mathbf{r},t) + \nabla \cdot \mathbf{F}(\vec{q}_N) \right] L_i(\mathbf{r}) d^3r = \\ \int_{\partial V_\Delta} \widehat{\mathbf{n}} \left[\mathbf{F}(\vec{q}_N(\mathbf{r},t)) - \mathbf{F}^*(\vec{q}_N(\mathbf{r},t)) \right] L_i(\mathbf{r}) d^2r \ . \end{aligned} \tag{3.15}$$

It is worth noting that several expressions occur for the introduced numerical flux $\mathbf{F}^*(\vec{q}_N(\mathbf{r},t))$. According to [6], the upwind flux is a proper choice for nodal schemes

in means of numerical stability and convergence:

$$\widehat{\mathbf{n}}\Big[\mathbf{F}(\vec{q}_N(\mathbf{r},t)) - \mathbf{F}^*(\vec{q}_N(\mathbf{r},t))\Big] = \begin{pmatrix} \frac{1}{\bar{\mathrm{Z}}}\Big\{\alpha\Big[\Delta\mathbf{E} - \widehat{\mathbf{n}}(\widehat{\mathbf{n}}\Delta\mathbf{E})\Big] + Z^+\widehat{\mathbf{n}}\times\Delta\mathbf{H}\Big\} \\ \frac{1}{\bar{\mathrm{Y}}}\Big\{\alpha\Big[\Delta\mathbf{H} - \widehat{\mathbf{n}}(\widehat{\mathbf{n}}\Delta\mathbf{H})\Big] + Y^+\widehat{\mathbf{n}}\times\Delta\mathbf{E}\Big\} \end{pmatrix}, \quad (3.16)$$

where

$$Z^{\pm} = \sqrt{\frac{\mu_0\mu^{\pm}}{\epsilon_0\epsilon^{\pm}}} \qquad \text{and} \qquad Y^{\pm} = \sqrt{\frac{\epsilon_0\epsilon^{\pm}}{\mu_0\mu^{\pm}}}\ , \quad (3.17)$$

and the corresponding sums:

$$\bar{\mathrm{Z}} = Z^+ - Z^- \qquad \text{and} \qquad \bar{\mathrm{Y}} = Y^+ - Y^-\ . \quad (3.18)$$

It is worth noting that with the index "-" we denote the local element, whereas the index "+" corresponds to the neighboring element. Moreover, Eq. 3.16 includes the field differences

$$\Delta\mathbf{E} = \mathbf{E}^+ - \mathbf{E}^- \qquad \text{and} \qquad \Delta\mathbf{H} = \mathbf{H}^+ - \mathbf{H}^-\ , \quad (3.19)$$

at the interface of the neighboring elements.

3.2 Boundary conditions

Since DGTD method is a volume method, we need to specify boundary conditions, i.e, to terminate the simulation domain. Several types of boundary conditions occur, such as Silver-Müller boundary conditions [11, 12], perfect electric conducting (PEC) and perfect magnetic conducting (PMC) boundary conditions. By applying the Silver-Müller boundary conditions, the outgoing radiation is partially absorbed at the outer boundary of the computational domain. Only spherical waves, impinging normally on the boundary, are perfectly absorbed. Therefore, to avoid back reflection, we need to attenuate the outgoing radiation. A very convenient approach for DGTD method is to apply an artificial domain, the so-called uniaxial perfectly matched layer (uPML), between the physical domain and the outer boundary, that is characterized by EM parameters:

$$\overleftrightarrow{\epsilon}' = \overleftrightarrow{\Lambda}\epsilon \quad \text{and} \quad \overleftrightarrow{\mu}' = \overleftrightarrow{\Lambda}\mu \quad \text{where} \quad \overleftrightarrow{\Lambda} = \begin{pmatrix} \frac{s_y s_z}{s_x} & 0 & 0 \\ 0 & \frac{s_x s_z}{s_y} & 0 \\ 0 & 0 & \frac{s_x s_y}{s_z} \end{pmatrix}. \quad (3.20)$$

The uPML parameters read

$$s_i = 1 - \frac{\sigma_i}{i\omega}, \quad i = x, y, z\ , \quad (3.21)$$

where the parameter σ_i is responsible for the damping of the outgoing radiation in the i-direction [9, 13]. Furthermore, the uPML and physical domain are characterized by the same EM parameters ($Z' = Z,\ Y' = Y$) in order to avoid back reflection at the interface of the two regions. In the case of PEC or PMC boundary conditions, the electric and magnetic fields are terminated at the outer boundary, respectively.

Boundary conditon	**$\Delta\mathbf{E}$**	**$\Delta\mathbf{H}$**
PMC	0	$-2\mathbf{H}^-$
PEC	$-2\mathbf{E}^-$	0
Silver-Müller	$-2\mathbf{E}^-$	$-2\mathbf{H}^-$

Table 3.2: Field differences for PEC, PMC and Silver-Müller boundary conditions [9, 14].

3.3 Sources of electromagnetic waves in DGTD

Due to the linearity of Maxwell equations, we can apply the total-field/scattered-field (TfSf) source. According to the TfSf technique, we split the EM fields into incident and scattered fields

$$\mathbf{E}_{\text{tot}}(\mathbf{r}, t) = \mathbf{E}_{\text{sc}}(\mathbf{r}, t) + \mathbf{E}_{\text{in}}(\mathbf{r}, t)\ , \tag{3.22}$$

where the subscripts “tot”, “in” and "“sc” indicate the total, incident and scattered field, respectively. By dividing the computational domain into two regions, the Tf and Sf region, we solve the Maxwell equations for total or only scattered fields, respectively,

$$\begin{aligned} \overleftrightarrow{Q}(\mathbf{r}) \cdot \partial_t \vec{q}_{\text{tot}}(\mathbf{r}, t) + \nabla \cdot \mathbf{F}(\vec{q}_{\text{tot}}) = 0 \\ \overleftrightarrow{Q}(\mathbf{r}) \cdot \partial_t \vec{q}_{\text{sc}}(\mathbf{r}, t) + \nabla \cdot \mathbf{F}(\vec{q}_{\text{sc}}) = 0\ . \end{aligned} \tag{3.23}$$

It is worth noting that at the interface between Tf and Sf region, the field differences (Eq. 3.19) are modified

$$\begin{aligned} \Delta\mathbf{E}_{\text{tot}}(\mathbf{r}, t) &= \mathbf{E}^+_{\text{sc}}(\mathbf{r}, t) + \mathbf{E}_{\text{inc}}(\mathbf{r}, t) - \mathbf{E}^-_{\text{tot}}(\mathbf{r}, t) \\ \Delta\mathbf{E}_{\text{sc}}(\mathbf{r}, t) &= \mathbf{E}^+_{\text{tot}}(\mathbf{r}, t) - \mathbf{E}_{\text{inc}}(\mathbf{r}, t) - \mathbf{E}^-_{\text{sc}}(\mathbf{r}, t)\ . \end{aligned} \tag{3.24}$$

In this work, the incident field takes the form of a pulsed plane wave or a pulsed waveguide mode [C1].

3.4 Material model in DGTD

3.4.1 Auxiliary Differential Equations

The DGTD method is a time-domain method and therefore, we need to model the time-dependent material response. In this regard, the time-dependent displacement for isotropic materials (see Eq. 1.6) reads

$$\mathbf{D}(\mathbf{r},t) = \int_{-\infty}^{t} \epsilon(\mathbf{r},t-\tau)\mathbf{E}(\mathbf{r},\tau)d\tau \ . \tag{3.25}$$

Instead of inserting Eq. 3.25 into Maxwell curl equations, we can apply the auxiliary differential equations (ADE) method. The frequency-dependent permittivity is given by

$$\epsilon(\omega) = \epsilon_\infty + \chi(\omega) \ , \tag{3.26}$$

where ϵ_∞ is the constant background permittivity and $\chi(\omega)$ is the susceptibility. Multiplying Eq. 1.7 by $-i\omega$, we have

$$-i\omega\mathbf{D}(\omega) = -i\omega\epsilon_\infty\mathbf{E}(\omega) + \mathbf{j}_p(\omega) \ , \tag{3.27}$$

with

$$\mathbf{j}_p(\omega) = -i\omega\chi(\omega)\mathbf{E}(\omega) \ , \tag{3.28}$$

where $\mathbf{j}_p$ is a polarization current. Moreover, by Fourier transforming Eq. 3.27, we obtain an expression for the temporal derivative of $\mathbf{D}(t)$:

$$\partial_t\mathbf{D}(t) = \epsilon_\infty\partial_t\mathbf{E}(t) + \mathbf{j}_p(t) \ , \tag{3.29}$$

and therefore, the third Maxwell equation reads

$$\partial_t\mathbf{E}(\mathbf{r},t) = \epsilon_\infty^{-1}(\mathbf{r})\Big(\nabla\times\mathbf{H}(\mathbf{r},t) - \mathbf{j}(\mathbf{r},t) - \mathbf{j}_p(\mathbf{r},t)\Big) \ . \tag{3.30}$$

It is clear that with the ADE method, we have to solve simple ADEs equations for $\mathbf{j}_p(t)$ instead of solving complicated integro-differential equations.

3.4.2 Drude model

In order to describe bulk noble metals in the infrared and visible regime, we can apply the Drude or Lorentz model. In the Drude model, since the valence electrons are assumed to not interact with other electrons or ions, the polarization current takes the form [15]

$$\mathbf{j}_D(\mathbf{r},\omega) = \frac{\omega_D^2}{\gamma_D - i\omega}\mathbf{E}(\mathbf{r},\omega) \ , \tag{3.31}$$

where the plasma frequency reads

$$\omega_D = \sqrt{\frac{e^2 n}{m_e}} \ , \tag{3.32}$$

while n is the density of the valence electrons, with charge e and mass m_e. The Fourier transform of Eq. 3.31 leads to the Drude ADE

$$\partial_t \mathbf{j}_D = \omega_D^2 \mathbf{E}(\mathbf{r}, t) - \gamma_D \mathbf{j}_D(\mathbf{r}, t) \ . \tag{3.33}$$

3.4.3 Lorentz model

On the other hand, if we want to take into account the interband transitions, the Lorentz model is suitable. A resonance frequency ω_L is introduced since electrons are considered as driven harmonic oscillators. Therefore, the susceptibility takes the form

$$\chi_L(\omega) = \frac{\Delta\epsilon_L \omega_L^2}{\omega_L^2 - i\gamma_L \omega - \omega^2} \ , \tag{3.34}$$

where $\Delta\epsilon_L = \omega_D^2/\omega_L^2$ is the oscillator strength, γ_L is the damping parameter and ω_L the eigenfrequency of the oscillator. By inserting Eq. 3.34 into Eq. 3.28, we obtain

$$\begin{aligned} -i\omega \mathbf{j}_L(\omega) &= \Delta\epsilon_L \omega_L^2 \mathbf{E}(\omega) + \mathbf{q}_L(\omega) \\ \mathbf{q}_L(\omega) &= -\frac{\omega_L^2 \mathbf{j}_L(\omega) + \gamma_L \Delta\epsilon_L \omega_L^2 \mathbf{E}(\omega)}{\gamma_L - i\omega} \ . \end{aligned} \tag{3.35}$$

The Fourier transform of Eq. 3.35 leads to

$$\begin{aligned} \partial_t \mathbf{j}_L(t) &= \Delta\epsilon_L \omega_L^2 \mathbf{E}(t) + \mathbf{q}_L(t) \\ \partial_t \mathbf{q}_L(t) &= -\omega_L^2 \mathbf{j}_L(t) - \gamma_L \Delta\epsilon_L \omega_L^2 \mathbf{E}(t) - \gamma_L \mathbf{q}_L(t) \ . \end{aligned} \tag{3.36}$$

It is worth noting that the Lorentz model is described by two ADEs. Finally, the material response for N_D Drude poles and N_L Lorentz poles is given by

$$\epsilon(\omega) = \epsilon_\infty - \sum_{i=1}^{N_D} \frac{\omega_{D,i}^2}{\omega(\omega + i\gamma_{D,i})} + \sum_{j=1}^{N_L} \frac{\Delta\epsilon_{L,j}\ \omega_{L,j}^2}{\omega_{L,j}^2 + i\gamma_{L,j}\omega - \omega^2} \ , \tag{3.37}$$

where for each N_D Drude pole corresponds one ADE and two free parameters, whereas for each N_L Lorentz pole corresponds two ADEs and 3 free parameters. Consequently, the third Maxwell equation reads

$$\partial_t \mathbf{E}(\mathbf{r}, t) = \epsilon_\infty^{-1}(\mathbf{r}) \Big[\nabla \times \mathbf{H}(\mathbf{r}, t) - \sum_{i=1}^{N_D} \mathbf{j}_D(\mathbf{r}, t) - \sum_{j=1}^{N_L} \mathbf{j}_L(\mathbf{r}, t) - \dots \Big] \ . \tag{3.38}$$

3.5 Computational example

3.5.1 Enhanced optical transmission in perforated metal films

Periodic arrays of subwavelength apertures in metal films exhibit unique optical properties due to the conversion of light into surface waves such as surface plasmons (SP). Moreover, the scattering by a hole array provides the additional momentum so that the incident light can couple to the SP mode. Due to the aforementioned interaction, enhanced transmission peaks, e.g., extraordinary transmission (EOT), have been reported in the transmission spectrum of perforated metal films. We assume a square hole array of radius 125 nm Aluminium film [16, 17] on a glass substrate ($\epsilon = 4$) with a period $P = 475\,\text{nm}$. The transmission spectrum is characterized by two peaks at $\lambda_1 = 500\,\text{nm}$ and $\lambda_2 = 725\,\text{nm}$. The resonance positions in the transmission spectrum are given in a first approximation, without taking into account the presence of the holes, by:

$$\lambda_{max} = \frac{P}{\sqrt{i^2 + j^2}} \sqrt{\frac{\epsilon_m \epsilon_d}{\epsilon_m + \epsilon_d}}\ , \tag{3.39}$$

where i, j are the scattering orders of the array, ϵ_m, ϵ_d are the dielectric constants of the metal and the dielectric material at the interface, respectively, and P is the period of the array.

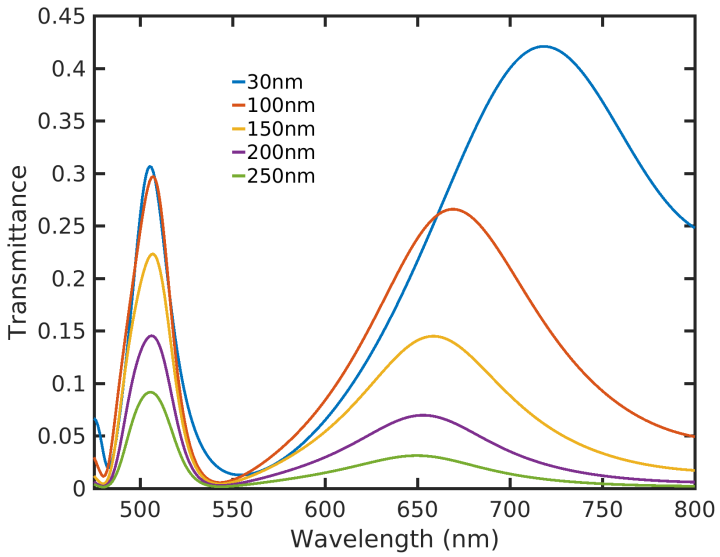

Figure 3.1: Variation of the transmission spectra, for light normally incident on a square hole array of radius 125 nm milled in an Aluminium film on a 30 nm thick glass substrate with period $P = 475\,\text{nm}$, versus the thickness of the metal film.

The transmission peak at lower wavelengths (see Fig. 3.1) is associated with $(i, j) = (1, 0)$ at the air-metal interface, while the second peak corresponds to the $(i, j) = (0, 1)$ mode at the metal-glass interface. According to Eq. 3.39, when the structure is asym-

metric, i.e., the material in immediate contact with the metal is different on either side of the holes, supports two sets of peaks. Each peak corresponds to one of the surfaces, e.g., to the air-metal or metal-glass interface, as in our case. It is worth noting that the transmission peaks predicted by Eq. 3.39 are slightly blue-shifted than the actual peaks due to the scattering by the holes. By increasing the metal thickness, we observe that both peaks are less pronounced. The resonance at higher wavelengths is blue shifted, while a slight red shift occurs for the transmission peak with higher energy (see Fig. 3.1).

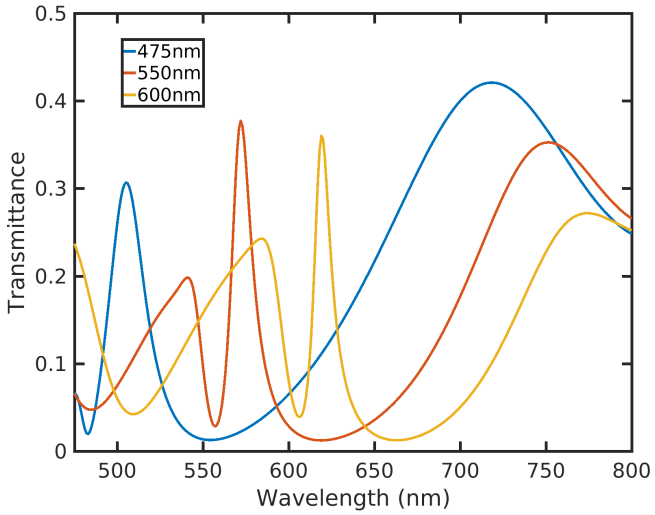

Figure 3.2: Variation of the transmission spectra, for light normally incident on a square hole array of radius 125 nm milled in a 30 nm thick Aluminium film on a 30 nm thick glass substrate, versus the period of the hole array.

It is worth mentioning that the hole array can be considered as a grating and each hole as a Huygens' source. Therefore for $\lambda > P$, only zero order diffraction occurs, whereas for $\lambda < P$, higher order diffractions are formed. By adjusting the period, we can tune the resonances to the desired wavelengths and therefore metal films with periodic array of holes can act as filters (see Fig. 3.2).

3.5.2 Convergence studies

It is important to determine the precision of our computations. In general, the most important parameters for the accuracy of the DGTD computations is the size h of the largest mesh element and the Lagrange polynomial order p. As we already mentioned, we can achieve higher accuracy by using more elements, e.g., at the interface of two materials. In our example, the most important region of the computational domain, where we have to study the convergence of the computations, is in (see Fig. 3.3) and around the hole area. In Fig. 3.4, we present the difference in the transmission spectra $\Delta T = T - T_{ref}$, for different sizes of the largest mesh element inside the hole. As a reference, we consider the transmission spectrum associated with the smallest size of the

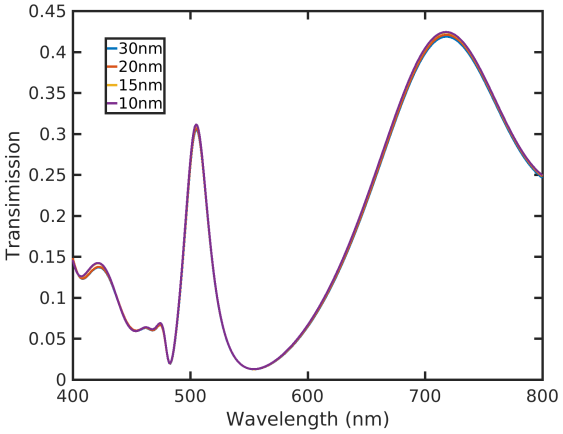

Figure 3.3: Variation of the transmission spectra, for light normally incident on a square hole array of radius 125 nm milled in a 30 nm thick Aluminium film on a 30 nm thick glass substrate, versus the size of the largest mesh element in the hole area.

largest mesh element $h = 10$ nm. By decreasing the size of the largest mesh element, we increase the number of elements in the specific area and therefore we can achieve better accuracy.

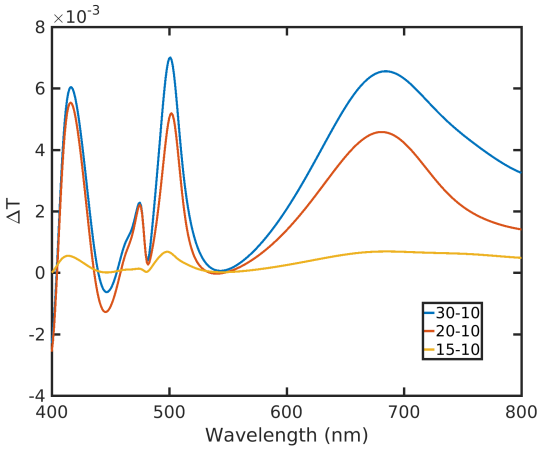

Figure 3.4: Variation of the transmission difference $\Delta T = T - T_{ref}$, for light normally incident on a square hole array of radius 125 nm milled in a 30 nm thick Aluminium film on a 30 nm thick glass substrate, versus the size of the largest mesh element in the hole area. As a reference, we use the transmission spectrum associated with the smallest size of the largest mesh element ($h = 10$ nm) inside the hole.

Another interesting topic in nanophotonics is the combination of plasmonics with magneto-optical materials. Since the magneto-optical response of conventional mate-

rials at infrared and visible frequencies is rather weak, magnetoplasmonic structures provide unique optical properties due to the strong field enhancement in the vicinity of the magneto-optical material. Moreover, such nanostructures are suitable for magneto-optical recording [18]. Therefore, by adding a 20 nm thick GdFeCo [19] magnetic film at the bottom of the afore-described design, we can study the optical properties of the considered magneto-optical structure.

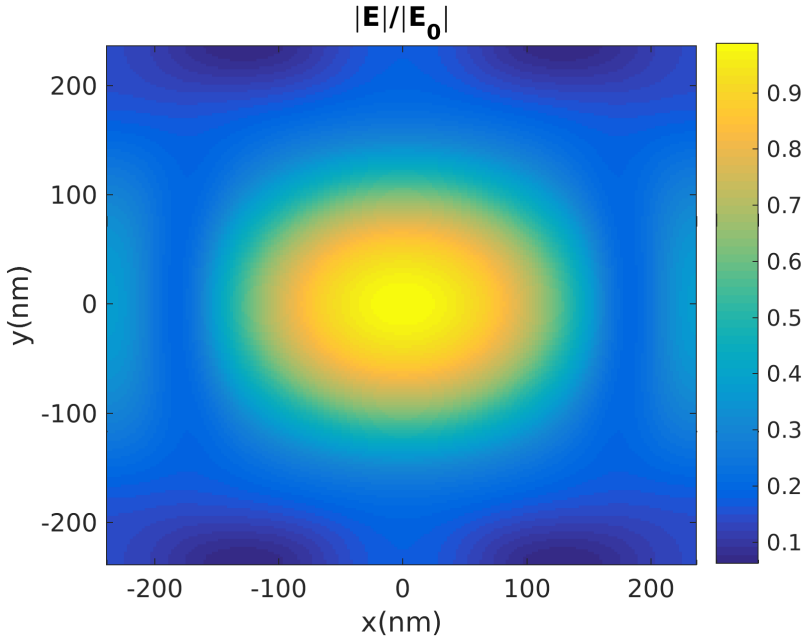

Figure 3.5: Relative (with respect to a linearly polarized incident plane wave) electric field amplitude distribution in the plane of polarization at the resonance wavelength $\lambda = 500\,\text{nm}$.

As the underlying mechanism is the field enhancement, it is important to compute the field distribution. By properly adjusting the period ($P = 474\,\text{nm}$) of the hole array, we obtain a strong field enhancement in the magnetic region (see Fig. 3.5), accompanied by an absorption peak (see Fig. 3.6) at the desired wavelength ($\lambda = 500\,\text{nm}$) which results in the optimal transfer of the optical energy to the magnetic recording layer. It is worth mentioning that for these computations, we took into account only the diagonal elements of the permittivity tensor of the magnetic material (GdFeCo) [19]. For the spatial discretization of the scattering geometry, we use an adaptive tetrahedral mesh by utilizing the freely available mesher NETGEN [20]. Furthermore, the simulation domain consists of a TfSf contour, from where we launch a Gaussian modulated plane wave, and contours for recording the Poynting flux. To terminate the simulation domain, we employ the Silver-Müller boundary conditions and to avoid back reflection of the outgoing radiation, we surround the computational domain with 400 nm thick layer of uPML at the top and bottom of the computational domain. Finally, we employ periodic boundary conditions along the x- and y-directions.

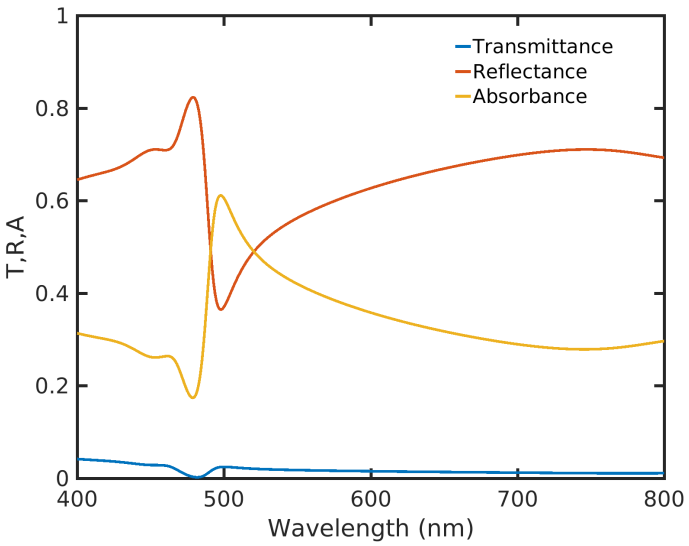

Figure 3.6: Transmission, reflection and absorption spectra, for light normally incident on a square hole array of radius 125 nm and period $P = 474$ nm milled in a 30 nm thick Aluminium film on a 30 nm thick glass substrate and a 20 nm thick GdFeCo.

CHAPTER 4

Design study of random spectrometers in the visible and NIR wavelength regime

Optical spectrometers are commonly used scientific instruments that utilize the effect of optical dispersion. While conventional spectrometers based on gratings designs feature relatively large footprints, compact spectrometers based on disordered planar waveguides utilize multiple scattering process which enhances the effective optical path length and leads to high spectral resolution combined with a small device footprint [21]. Since many biological and medical applications [22–24] taking place in the near-infrared and visible regime, where molecules exhibit low fluorescence and water, tissue and cells feature low absorption, silicon nitride is the material of choice as it is a robust material [25, 26] with low thermal sensitivity and compatible with CMOS-based processes. Moreover, silicon nitride is a transparent material in a broad wavelength regime (from 300 nm to 5000 nm) with a relatively high refractive index ($n \sim 2$) at optical frequencies and therefore suitable for many applications in the visible and NIR regime [27–30].

In the present work [P1], through exact numerical electrodynamic simulations (using a Discontinuous Galerkin Time-Domain finite-element approach) in conjunction with Mie and multiple scattering theory, we study the performance of silicon nitride-based random spectrometers for frequencies in the visible, NIR, and telecom ranges for both TE- and TM-polarizations. Specifically, we demonstrate how the spectral resolution depends on single scattering properties for low concentration of scatterers and we provide reliable guidelines for obtaining high resolution. In our subsequent analysis, we represent the silicon-nitride-based structure with a wavelength-independent refractive index $n = 2$. As scatterers, we consider identical pores that have been etched into silicon nitride waveguides.

4.1 Random spectrometer design study

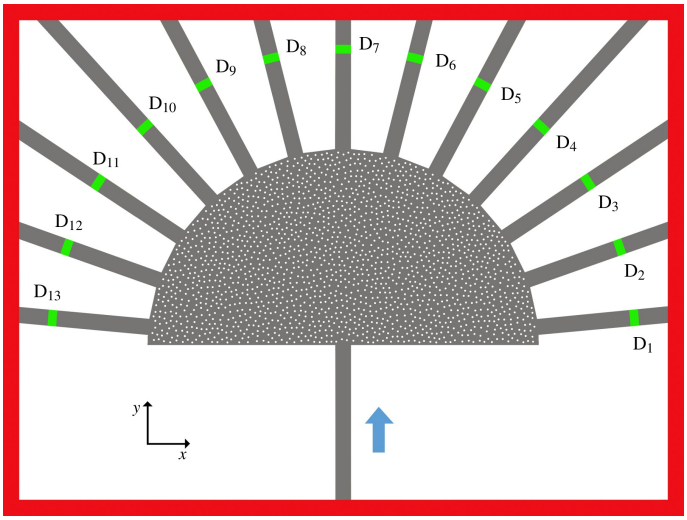

Figure 4.1: Schematic of the random spectrometer. An input waveguide delivers a fundamental mode pulse [C1] into the center of the semicircular scattering area and after multiple scattering, light is detected at the detectors D_1, ... D_{13} (green lines) or escapes into free space (white-shaded region). Gray-shaded regions represent the silicon-nitride-based spectrometer, white-shaded regions represent the free space, and red-shaded regions correspond to perfectly matched layers (PMLs). Reprinted with permission from [P1] ©The Optical Society of America.

The random spectrometer is formed of a 2D semicircular scattering area of radius $L = 25\,\mu m$ (see Fig. 4.1), which consists of a random array of identical pores with radius 125 nm and covers the 9% of the scattering area. Through a single input waveguide (with a width of 2 µm), a fundamental mode pulse [C1] is launched into the center of the scattering area, where light is multiply scattered by the pores and finally reaches the 13 readout waveguides (with widths of 2 µm) along the circumference of the scattering area. The radiation that reaches the readout ports is determined by the detectors D_1, ..., D_{13}. After a single time-domain computation, we recover the Fourier transformed time dependent output signals which are stored in a transmission matrix T. The transmission matrix T describes the intensity distribution over the detectors through the relation $I = TS$, where I is the detected intensity and S the input signal. For the numerical computations, we employ the DGTD approach [7, 8]. The dimensions of the physical simulation domain are 83.00 µm x 61.25 µm, surrounded by 2 µm of PMLs on all sides. We used $1.6 * 10^6$ triangular finite elements for the spatial discretization of the computational domain with 4.7 nm smallest element size. For the time-stepping, we employ a 14-stage fourth-order low-storage-Runge scheme [8]. By using 3^{rd}-order basis functions, the total run-time of 385 hours for a complete computation on a dual-CPU mainboard equipped with Intel XEON E5-2670 processor at 2.60 GHz requires 0.85 GByte RAM. The physical

simulation time corresponds to 5.67 ps.

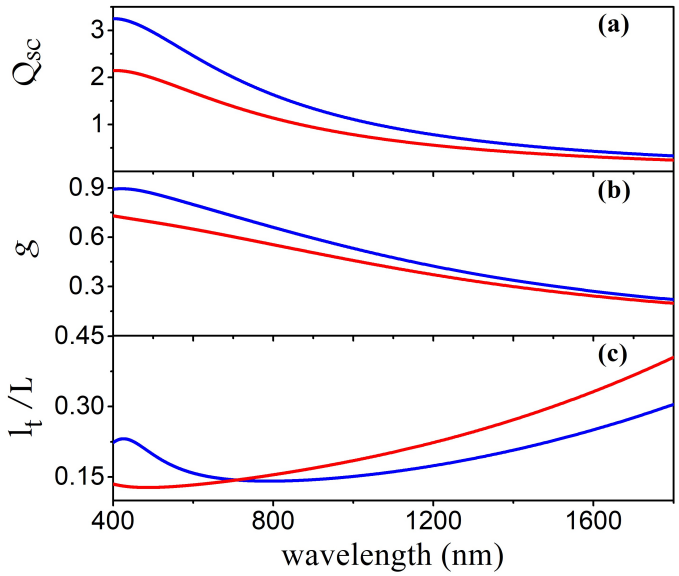

Figure 4.2: (a) Scattering efficiency Q_{sc} and (b) asymmetry parameter g for an air cylinder of radius 125 nm, for TM- (electric field parallel to the cylinder axis) and TE-polarization (electric field perpendicular to the cylinder axis), under normal incidence (red and blue lines, respectively). The host medium is silicon nitride. (c) Transport mean free path l_t normalized to the radius L of the scattering area of a 2D random array of air pores in a silicon nitride matrix with a filling fraction of $f = 0.09$. Reprinted with permission from [P1] ©The Optical Society of America.

The spectral resolution of the spectrometer is quantified by the spectral correlation function [21]

$$C(\Delta\lambda, D_i) = \frac{\langle I(\lambda, D_i) I(\lambda + \Delta\lambda, D_i)\rangle}{\langle I(\lambda, D_i)\rangle \langle I(\lambda + \Delta\lambda, D_i)\rangle} - 1 \ , \tag{4.1}$$

where $I(\lambda, D_i)$ is the light intensity recorded at the detector D_i ($i = 1, 2, ..., 13$) with wavelength λ, while the average is over the wavelength. The spectral correlation function C is normalized at $\Delta\lambda = 0$ and averaged over all detectors. The half-width at half-maximum (HWHM) in the correlation function spectrum provides an estimate of the spectral resolution.

Since the pore filling fraction is $f = 0.09$, the multiple scattering process can be described by the independent scattering approximation [31, 32]. Moreover, it is well known from multiple-scattering theory [33, 34] that the transport mean free path for lossless scatterers is given by

$$l_t^{s,p} = \frac{\pi S}{2 f Q_{sc}^{s,p} (1 - g^{s,p})} \ , \tag{4.2}$$

where S is the radius of the scatterer, $Q_{sc}^{s,p}$ is the scattering efficiency (Eq. 2.35) and $g^{s,p}$

the asymmetry parameter (Eq. 2.37). The superscripts s and p correspond, respectively, to s-wave (TM-polarization, electric field perpendicular to the xy-plane in Fig. 4.1) and p-wave (TE-polarization, electric field parallel to the xy-plane in Fig. 4.1). In the diffusive regime, the effective optical path length scales as $l_t^{s,p}/L^2$ [35]. Therefore, we can achieve higher spectral resolution by reducing the transport mean free path $l_t^{s,p}$. For this purpose, according to Eq. 4.2, reduced transport mean free paths can be expected when the scattering is strong (high scattering efficiency) and when the scattering is either isotropic ($g \sim 0$) or even backward ($g < 0$).

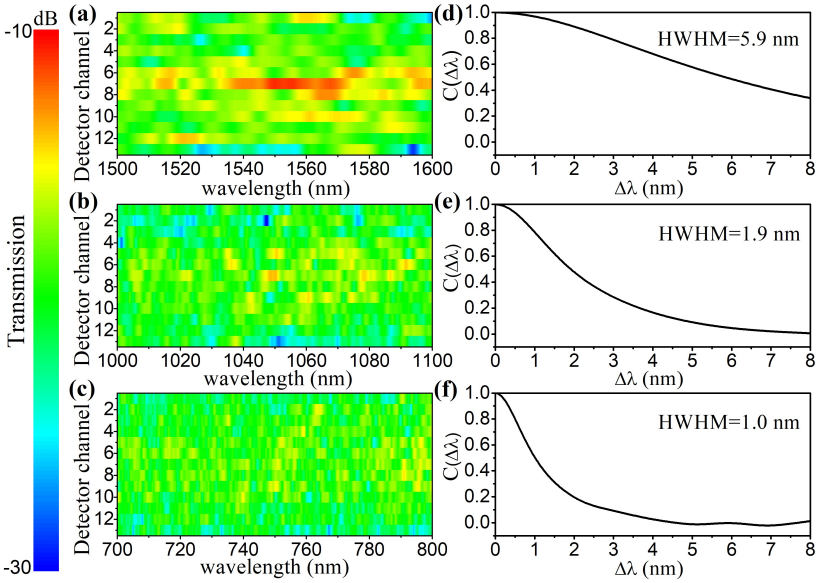

Figure 4.3: Panels (a), (b) and (c): Wavelength- and detector-resolved transmission matrix for the random spectrometer depicted in Fig. 4.1 for TE-polarization in the telecom, NIR, and visible wavelength regime, respectively. Light is launched from the input waveguide and detected by the detectors D_1 to D_{13}. The ordinate labels correspond to the detector index. The color coding corresponds to the relative intensity transmitted into the different waveguides and expressed in decibels. Panels (d), (e) and (f): The normalized spectral correlation function corresponding to the wavelength regimes of panels (a), (b) and (c). Reprinted with permission from [P1] ©The Optical Society of America.

For an air cylinder of radius 125 nm into a silicon nitride matrix (see Fig. 4.2), the scattering efficiency, for TE- and TM-polarization, increases monotonously while moving to shorter wavelengths, where at the same the direction of the scattering becomes more forward (higher asymmetry parameter). Overall, the transport mean free path decreases when moving from telecom to visible wavelengths (with a minimum around 700 nm for TE-polarization) and consequently, we expect high spectral resolution of the random spectrometer at visible and NIR frequencies. Upon moving to even shorter wavelengths ($\sim$ 400 nm), we observe a peak in the transport mean free path spectrum, for TE-

polarization, due to the fact that light scatters almost only in the forward direction ($g \sim 0.9$).

Since the transport mean free path is relatively high and comparable to the scattering area at telecom wavelengths (1500 nm-1600 nm), a ballistic transport regime occurs and we observe, according to Figs. 4.3(a) and 4.4(a), that the intensity distribution over the detectors is characterized by high concentrations in the central readout waveguides, for TE- and TM-polarization, respectively.

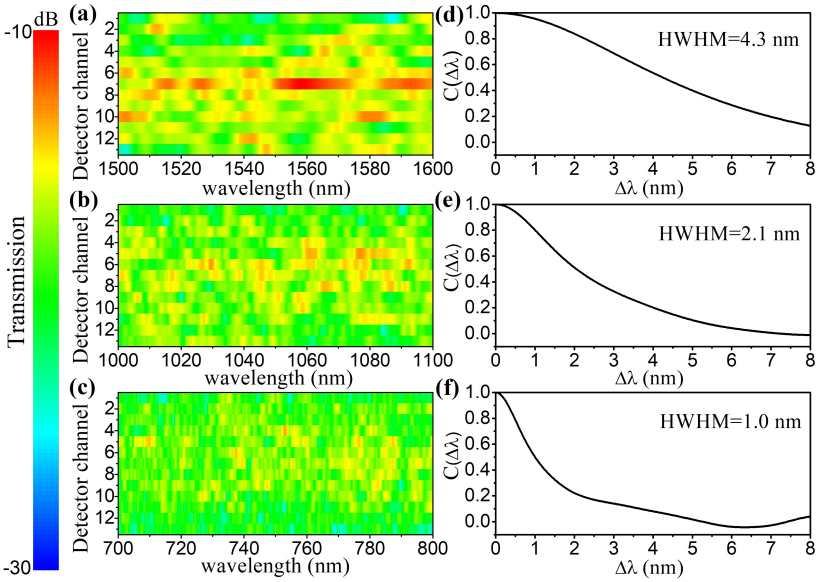

Figure 4.4: Panels (a), (b) and (c): Wavelength- and detector-resolved transmission matrix for the random spectrometer depicted in Fig. 4.1 for TM-polarization in the telecom, NIR, and visible wavelength regime, respectively. Light is launched from the input waveguide and detected by the detectors D_1 to D_{13}. The ordinate labels correspond to the detector index. The color coding corresponds to the relative intensity transmitted into the different waveguides and expressed in decibels. Panels (d), (e) and (f): The normalized spectral correlation function corresponding to the wavelength regimes of panels (a), (b) and (c). Reprinted with permission from [P1] ©The Optical Society of America.

In the NIR wavelength part of the spectrum (1000 nm-1100 nm), the onset of the diffusion occurs due to the stronger scattering and we obtain a more uniform distribution along with stronger decorrelation of light. Consequently, we expect a higher resolution since the HWHM is less than half the values obtained at telecom wavelengths, for both polarizations.

The diffusive transport regime is fully developed at the red end of the visible spectrum (700 nm-800 nm) due to a further decrease of the transport mean free path (Fig. 4.2(c)). Moreover, in this wavelength regime, we obtain the highest resolution (HWHM = 1.0 nm) for both polarizations (see Figs. 4.3(f) and 4.4(f)), where at the same time the trans-

mission matrix is characterized by sharp intensity peaks, uniformly distributed over the readout ports (Figs. 4.3(c) and 4.4(c)).

Therefore, the size of the scattering area can be determined by the transport mean free path due to the trade-off between the footprint of the device and the spectral resolution. When the radius of the scattering area is much longer than the transport mean free path, the diffusive regime is fully developed and subsequently, we obtain the highest resolution. However, in many applications where the size of the spectrometer should be relatively small, we can design the size of the scattering area in order to achieve the onset of the diffusion and consequently, acceptable resolution.

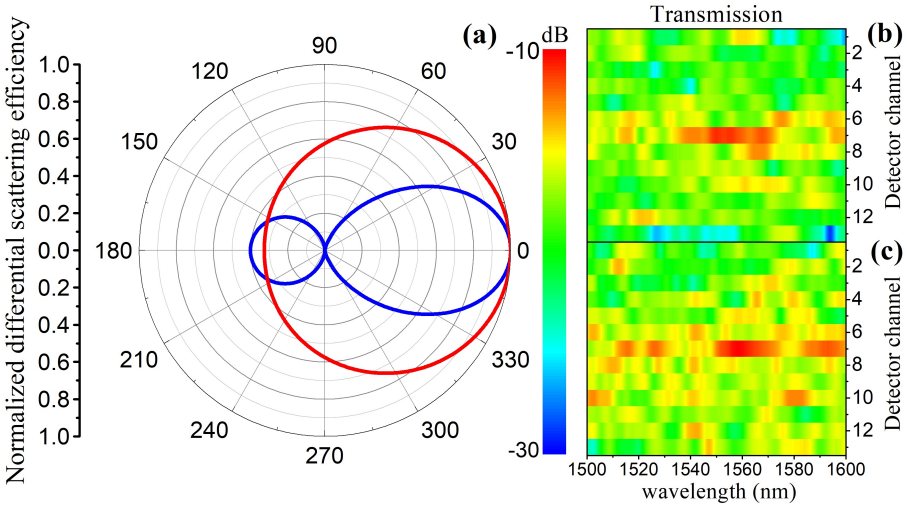

Figure 4.5: Panel (a): Angular scattering characteristics, Eq. (2.36), for an air pore of 125 nm radius embedded in a silicon nitride matrix, for TE- (blue line) and TM- (red line) polarization and fixed wavelength $\lambda = 1500\,\text{nm}$. Light scatters to larger angles for TM polarization due to predominance of s-wave scattering. Panels (b),(c): Wavelength- and detector-resolved transmission matrix for TE and TM polarizations, respectively. Reprinted with permission from [P1] ©The Optical Society of America.

Notably, the angular distribution of light over the detectors can be explained by studying the angular distribution of scattering by a single scatterer (cf. Fig. 4.5). Moreover, for TE-polarization, light scatters in p-waves and subsequently is mostly detected in the central readout waveguides. For TM polarization, the single scattering is more isotropic due to the dominant scattered s-waves and therefore the distribution of light over all detectors is more uniform. It is worth noting that the correlation between single and multiple scattering in the angular distribution holds only in the regimes where the diffusion is not fully developed (cf. Figs. 4.3(b) and 4.4(b)).

Our simulations are carried out in two dimensions so that we cannot directly address out-of-plane losses. For these strictly two dimensional simulations, we provide the total transmission (normalized to the input intensity) into the 13 output ports of the

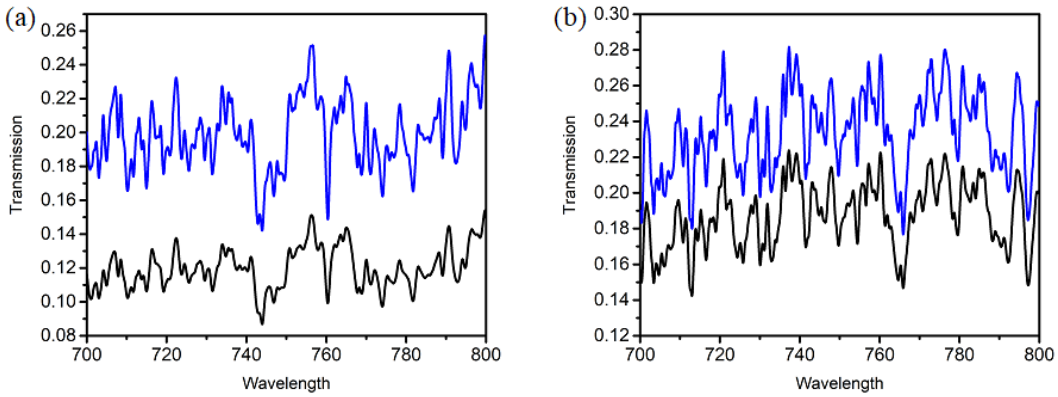

Figure 4.6: Panel (a): TE-polarization. Panel (b) TM-polarization. Frequency-resolved simulated total transmission into the 13 output ports of the random spectrometer whose transmission matrices are depicted in Figs. 4.3 and 4.4 of the manuscript (filling ratio $f = 0.09$, radius of semicircular scattering area $L = 25\,\mu m$). The simulations are carried out in two dimensions. In order to provide an estimate of the out-of-plane losses, we have carried out two types of simulations: While the blue lines correspond to simulations with lossless materials, the black lines correspond to simulations where a small imaginary part ($Im\epsilon = 0.01$) has been added into the air pores of the scattering region.

random spectrometer in the frequency range between 700-800 nm (the corresponding port-resolved transmission matrices are depicted in Figs. 4.3(c) and 4.4(c)). By their very nature, these simulations only include scattering losses in the plane of propagation. In order to emulate out-of-plane losses, we recompute the transmission matrices and total transmission into the 13 output ports for the same system by including a small imaginary part of 0.01 to the dielectric constant of the air pores. The results clearly show a reduced overall total transmission which nonetheless is within the experimentally accessible range. Overall, this approximate treatment of out-of-plane losses lowers the total transmission roughly by a factor of two. The resulting 10% - 18% total transmission is consistent with experimental results on the full 3D structures.

In order to provide an experimental estimate of the attainable device performance, we have measured the total transmission into the 13 output ports (including out-couplers) and normalized to the transmission of a reference waveguide (without scattering area but complete with in- and out-coupler). Therefore, we provide an estimate for the total transmission of the device only, i.e., for the random spectrometer without coupling structures but including out-of-plane losses. A typical result within the frequency range discussed above is depicted below – the total transmission lies within the 10% - 20% range. These measured losses are consistent with the results of the two-dimensional simulations augmented by an effective treatment of the out-of-plane losses via a small imaginary part of the dielectric constant in the pores.

In terms of signal-to-noise ratio, the measurable performance is eventually limited by the sensitivity of the photoreceivers used to characterize the light levels at each waveguide

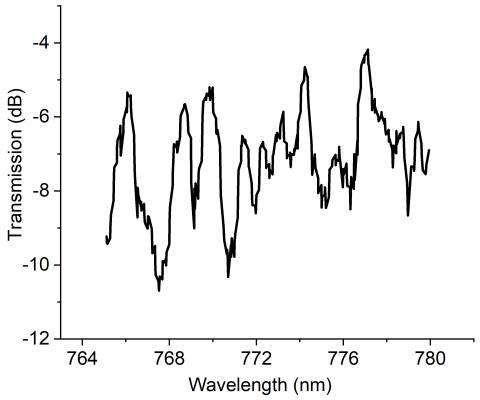

Figure 4.7: Frequency-resolved measured total transmission into the 13 output ports (including out-couplers) of a random spectrometer with filling ratio $f = 0.05$ that is slightly lower than in the above simulations and a slightly larger semicircular scattering area than in the above simulations (radius $L = 30\,\mu m$ in the experiment, radius $L = 25\,\mu m$ in the simulations). The total transmission is normalized to the transmission of a reference waveguide (including in- and out-couplers) so that the results characterize the actual random spectrometer device including out-of-plane losses.

output of the on-chip device. Since no spectral information is recorded at the output of each waveguide channel, we are able to use low-noise photodetectors with a noise floor of -110 dBm at 1550 nm and -90 dBm at visible wavelengths. These levels lie far below the transmission level through the device at each channel ($\sim -20\,dBm$). Hence, the remaining dynamic reserve is quite large and does not impact the measurement of our devices.

Our electromagnetic simulations discretize the computational domains into finite-element meshes. Clearly, these meshes resolve each and every pore of any simulated spectrometer (and all other material boundaries as well). Therefore, our simulations fully incorporate each and every Mie resonance present in the system for every filling fraction. With regards to Mie resonances of a single particle, we would like to note that whether or not a Mie resonance manifests itself as a pronounced spectral feature depends (a) on the dielectric contrast and (b) on the topology (i.e., low-index inclusion in a high-index background or high-index inclusion in a low-index background). Quite generally, the lower the index contrast, the less pronounced are the Mie resonances. Moreover and equally generally, the Mie resonances for low-index inclusions in a high-index matrix (i.e., for the topology considered in our work) are considerably less pronounced than for the reverse topology. Thus in our case of a rather moderate index-contrast (silicon nitride vs. air corresponds to an index contrast of 2:1) and the low-index-inclusion topology, we expect the Mie resonances to be rather broad. In fact, a careful inspection in Fig. 4.2(a) already reveals that the first Mie resonance appears in the scattering efficiency around

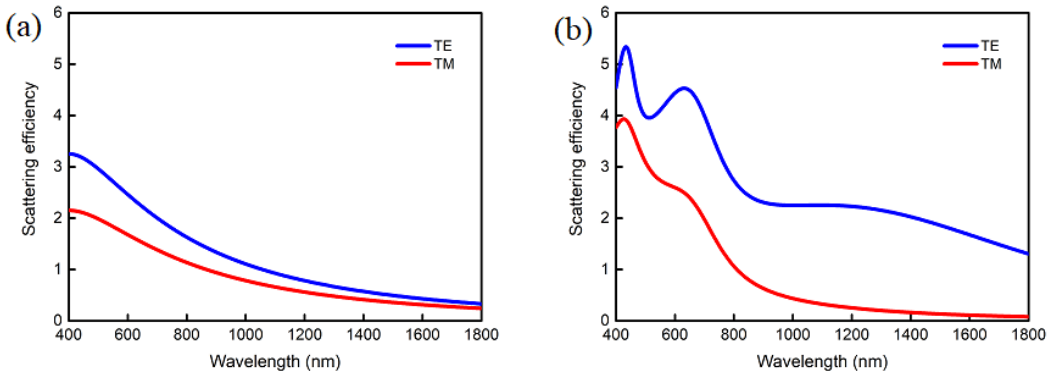

Figure 4.8: Panel (a): Scattering efficiency (scattering cross section normalized to the geometric cross section) of an air pore of radius 125 nm in silicon nitride under normal incidence for TM- and TE-polarization. Panel (b): Scattering efficiency of a silicon nitride rod of radius 125 nm in air under normal incidence for TM- and TE-polarization. While the rod-in-air system exhibits rather strong and spectrally well-localized Mie resonances, the reverse topology scatters less strongly and the Mie resonances are much less pronounced.

a wavelength of 400 nm and is extremely broad, both for TM- and TE-polarization. In fact, this feature of not-so-well pronounced Mie resonances is exactly what makes our material system (pores in silicon nitride) so attractive as the resulting spectrometers can be operated in a very broadband fashion and, for instance, apply to other material systems such as ZnO, chalcogenides, and LiNbO3 and broad wavelength ranges. To be even more explicit, and to illustrate the above-mentioned topology-dependence, we provide below a comparison of the scattering efficiencies in TE- and TM-polarization of an air pore (125 nm radius) in silicon nitride with the scattering efficiencies in TE- and TM-polarization of a silicon nitride rod (125 nm radius) in air.

For low filling fractions of scatterers (very roughly up to filling fractions of about 10%), multiple-scattering theory allows us to express the quantities relevant to the multiple scattering medium such as scattering and transport mean free paths, energy transport velocities, diffusion constants, etc. in terms of the single-scatterer quantities (such as the single-scatterer scattering cross section, asymmetry parameter, T-matrix, etc.) and the filling fraction alone (independent scattering approximation). Specifically, in Eq. 4.2, the transport mean free path expressed in terms of the single-scatterer scattering cross section and single-scattering asymmetry parameter for low filling fractions is one of the main results of multiple-scattering theory. This originates from the fact that for low filling fractions, independent scattering prevails, i.e., light scatters at a scatterer and then "moves" on to the next scatterer. However, because of the low filling fraction, this "moving" on to the next scatterer is essentially uncorrelated with the previous scattering event. Clearly, it is precisely in this regime that the effects of Mie resonances have a maximum impact on the multiple-scattering medium's properties (as exemplified by Eq. 4.2). Consequently, as these quantities enter into Eq. 4.2, our multiple-scattering

results fully contain the effect of Mie resonances – just as our electrodynamic simulations fully contain the results of Mie resonances.

In the high filling fraction regime, multiple-scattering theory becomes somewhat more complicated and this is related to the afore-mentioned "moving on to the next scatterer". In fact, the scattering cross section of a single scatterer provides the effective optical size, which can be considerably larger than the geometrical size (see Fig. 4.2(a)). This means that for higher filling fractions, the effective sizes of the single scatterers start to overlap long before geometrical close packing is reached. Once these effective sizes start to overlap, "moving on to the next scatterer" becomes a correlated process and corrections to the results of the independent scatterer approximation become important. Specifically, this overlap of effective sizes leads to a smearing out of the spectral features associated with single-scatterer Mie resonances. One way of dealing with this effect is to utilize an effective medium theory [4]. In this approach, the strongly scattering medium is replaced by effective scattering units that are embedded in a fictitious host material with renormalized properties that encode the above correlation effects. This system of "effective scattering units in a fictitious host material" then becomes amenable to a treatment within the independent scattering approximations.

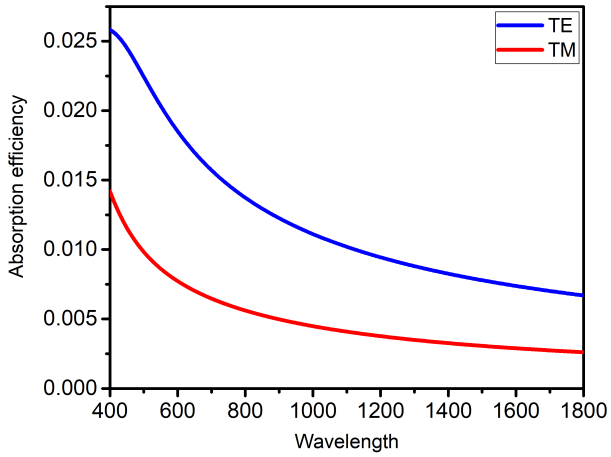

Figure 4.9: Absorption efficiency (absorption cross section normalized to the geometric cross section) of an air pore of radius 125 nm with $\epsilon = 1 + 0.01i$ in silicon nitride under normal incidence for TM- and TE-polarization.

Finally, an important question regarding the usefulness of a random spectrometer is that the device should work independently of the concrete realization of the random pores. This clearly mandates that the random spectrometer works in the diffusive regime, i.e., that the transport mean free path is sufficiently small relative to the device size, i.e., in our case the radius of the semi-circle. If this diffusive limit is not reached (in our case of a filling fraction of 9% and operation around 1500 −1600 nm), the device operates in the ballistic regime and its performance depends on the concrete realization of disorder, i.e., the precise arrangement of the pores. This is the essence of why we combine numerical simulation with multiple-scattering theory. Multiple-scattering theory clearly

states that the random spectrometer is more likely to operate in the diffusive regime for wavelengths between 700-800 nm than for wavelengths between 1500 −1600 nm, but it is not entirely clear whether a ratio of transport mean free path to device size of about 0.15 is already sufficient for realizing the diffusive regime. Our subsequent numerical simulations clearly demonstrate that diffusive transport occurs in the 700 −800 nm range whereas the behavior in the 1500 −1600 nm range is dominated by ballistic transport and it might be possible to find specific pore arrangements where resolution in the ballistic regime is improved relative to those we have shown above (or potentially even better than when the device operates in the diffusive regime). Clearly, by changing the filling fraction, we can potentially also reduce the size of the spectrometer, but higher filling ratios also will lead to larger out-of-plane losses. Notably, the total transmission spectrum can be associated with the absorption cross section spectrum by a single scatterer of radius 125 nm with $\epsilon = 1 + 0.01i$ in silicon nitride matrix (see Fig. 4.9). Moreover, in the case of TE-polarization, where the absorption is higher, we observe lower total transmission (see Fig. 4.6) and reflection due to the stronger optical losses.

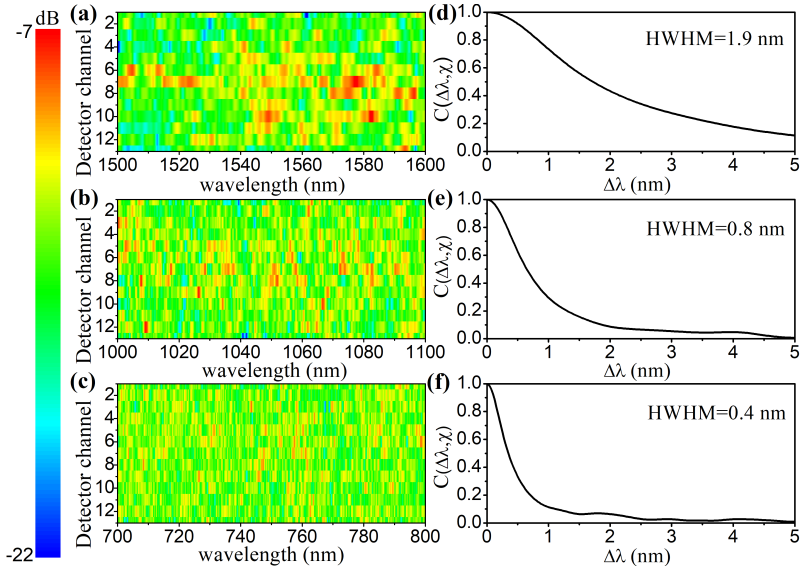

Figure 4.10: Panels (a), (b) and (c): Wavelength- and detector-resolved transmission matrix for a random spectrometer surrounded by PMC boundary for TE-polarization in the telecom, NIR, and visible wavelength regime, respectively. The ordinate labels correspond to the detector index. The color coding corresponds to the relative intensity transmitted into the different waveguides and expressed in decibels. Panels (d), (e) and (f): The normalized spectral correlation function corresponding to the wavelength regimes of panels (a), (b) and (c).

In order to confine light in the scattering area, we could surround the random spectrometer with a reflecting boundary which is a perfect magnetic conductor (PMC) or perfect electric conductor (PEC), for TE- or TM- polarized light, respectively. Due to the reflecting boundary, the light scatters back into the scattering area and therefore

more scattering events take place. Moreover, since light is confined into the random spectrometer, the computational area is significantly reduced, whereas the overall computational time is increased due to the longer effective optical path length. As can be seen in Figs. 4.10 and 4.11, with the reflecting boundary, the random spectrometer exhibits a more uniform light distribution over the detectors and overall higher spectral resolution in the different wavelength parts. At telecom wavelengths, we already observe the onset of the diffusion regime for both polarizations with a HWHM = 1.9 nm. Upon moving to NIR wavelengths, the transmission matrix is characterized by sharp peaks, while the HWHM is less than 1 nm (HWHM = 0.8 nm). In the visible regime, we obtain the highest resolution accompanied by a strong decorrelation of light with HWHM = 0.4 nm.

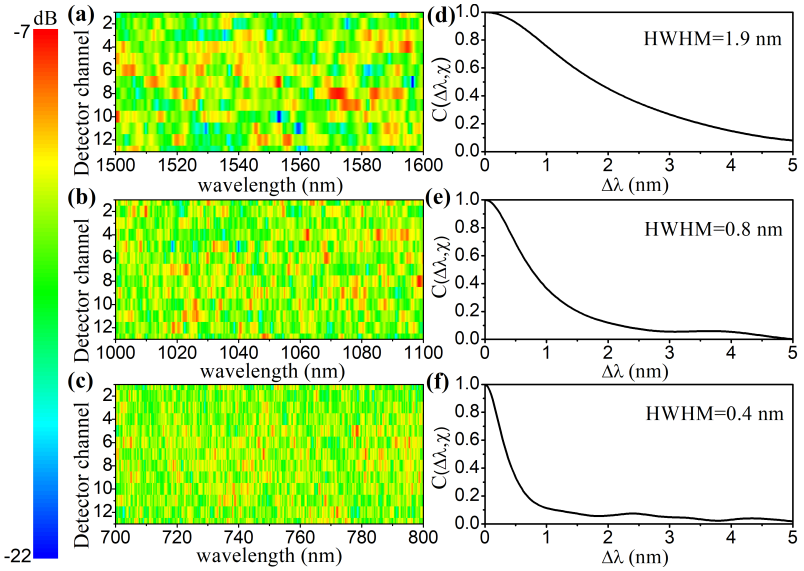

Figure 4.11: Panels (a), (b) and (c): Wavelength- and detector-resolved transmission matrix for a random spectrometer surrounded by PEC boundary for TM polarization in the telecom, NIR, and visible wavelength regime, respectively. The ordinate labels correspond to the detector index. The color coding corresponds to the relative intensity transmitted into the different waveguides and expressed in decibels. Panels (d), (e) and (f): The normalized spectral correlation function corresponding to the wavelength regimes of panels (a), (b) and (c).

Notably, the HWHM of the spectral function at the different wavelengths regimes is the same for both polarizations. This fact indicates that when the diffusive transport is fully developed, the spectrometer exhibits a polarization-independent spectral resolution.

4.2 Spectral reconstruction algorithm

To reconstruct a discretized input signal, we first have to calibrate the transmission matrix T by recording the intensity distribution of a "monochromatic" input light on

the detectors. Therefore, by setting a tunable laser, for every new position of the input centre wavelength, we obtain an I^{k_λ} vector, which divided by the input signal value S_{k_λ} can be considered as the next column of the transmission matrix:

$$I^{k_\lambda}(1:\lambda_f) = T(1:\lambda_f, k_\lambda)S_{k_\lambda} \ , \tag{4.3}$$

where λ_f is the number of the recorded wavelengths. It is clear from Eq. 4.3 that the measured vector I^{k_λ} is proportional to the k_λ column of the transmission matrix. The simple approach by inverting the transmission matrix $S = T^{-1}I$ in order to reconstruct the input signal fails as the inversion of the transmission matrix is ill-conditioned due to the experimental noise. To overcome this issue, we employ a singular value decomposition algorithm

$$\begin{aligned} (T)_{N\times M} &= (U)_{N\times N}(D)_{N\times M}(V)^T_{M\times M} \ , \\ UU^T &= 1 \\ V^TV &= 1 \\ D &= diag(d_1, d_2, ..., d_N) \\ d_1 &> d_2 > ... > d_N > 0 \ , \end{aligned} \tag{4.4}$$

where U and V are unitary matrices, D is a diagonal matrix with real positive singular values and $N = 13$ denotes the number of the output waveguides. Since the small values of the elements of the matrix D are the most susceptible to experimental noise and can be amplified in the inversion process $T^{-1} = VDU^T$, we employ a truncated version approach [36], where we consider as zero the small singular values of the matrix D. By taking into account only the elements with the higher singular values N_L, we have:

$$(T)_{N\times M} = (U)_{N\times N_L}(D)_{N_L\times N_L}(V)^T_{N_L\times M} \ , \tag{4.5}$$

where the pseudo-inverse of the transmission matrix takes the form:

$$(T)^{-1}_{M\times N} = (V)_{M\times N_L}(D)^{-1}_{N_L\times N_L}(U)^T_{N_L\times N} \ . \tag{4.6}$$

In order to test the truncated inversion technique of the singular value decomposition algorithm, we attempt to resolve two spectral lines at 1580 nm and 1585 nm. In Fig. 4.12, we show the reconstructed spectra for different numbers of non-zero elements of the matrix D. Moreover, for $N = 13$, the truncated inversion technique fails due to the strong background noise. For $N = 12, 11, 10, 9$ non-zero elements, the background noise is reduced, but not eliminated, and consequently, the two spectral peak positions at 1580 nm and 1585 nm can be reconstructed. Further reduction of the non-zero elements, e.g., $N = 5$ affects the resolution of the spectrometer by making the recovered spectral peaks broader and consequently, the resolve of two closely spaced peaks fails [36].

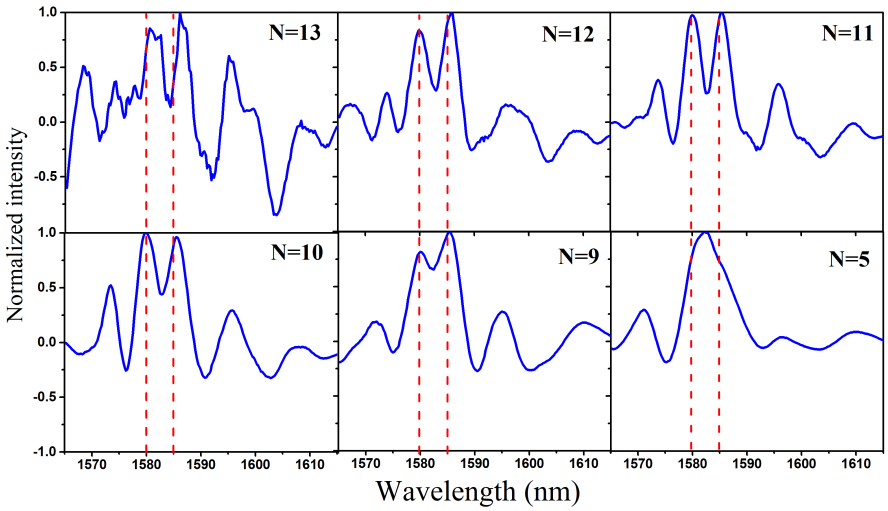

Figure 4.12: Reconstructed spectrum (blue line) of two spectral lines separated by 5 nm using the truncated version approach. N indicates the number of singular values used in the transmission matrix inversion algorithm. The red dotted lines mark the centre wavelengths of the probe lines.

Since the background noise is still present, even for the optimal number ($N = 11$) of the non-zero elements of the matrix D in the truncated inversion approach, we can further improve the quality of the spectral resolution by employing a nonlinear optimization algorithm where the optimal input signal S minimizes $\left\|I - TS\right\|^2$ [37, 38]. In Fig. 4.13, we show that due to the nonlinear optimization algorithm, the width of the spectral peaks and the background noise are sufficiently reduced. In this work, we use the non-linear optimization technique for the reconstruction of the input spectra.

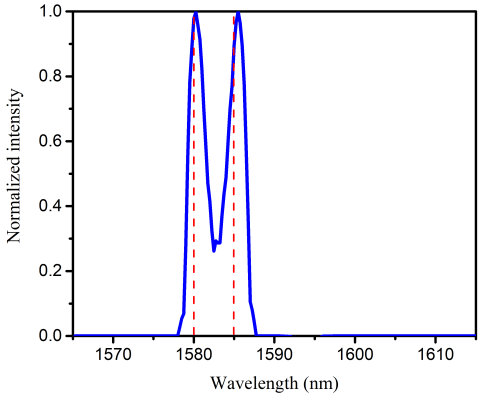

Figure 4.13: Reconstructed spectrum (blue line) of two spectral lines separated by 5 nm using a nonlinear optimization algorithm. The red dotted lines mark the centre wavelengths of the probe lines.

4.3 Experimental results

As we already mentioned, silicon nitride-based random spectrometers are expected to show high spectral resolution in the visible and NIR wavelength regime along with small footprint [P1]. The realization of these spectrometers is accomplished by Hartmann et al. [P3] so that the experimental findings and the theoretical predictions show good agreement. As we can see in Fig. 4.14, through a single input waveguide (with a width of 1.3 µm), light is launched into the center of the semicircular scattering area and after multiple scattering, the signal reaches the 13 output waveguides at the circumference of the scattering area (with an initial width of 2.5 µm, which is linearly tapered to 1.3 µm). The semicircular scattering area of radius $L = 100$ µm consists of a random array of identical pores with radius 125 nm and covers the 5% of the scattering area. Due to the semicircular shape of the scattering area, the distance from the center to the output waveguides is constant. In Fig. 4.14 (b), a scanning electron micrograph of a random spectrometer is depicted. As shown in the schematic of the whole device (see Fig. 4.15(a)), the random spectrometer is coupled with 3D polymer fiber-to-waveguide couplers [P2], which provide broadband transmission, low optical losses, and high stability (see Fig. 4.15(b)). It is worth noting that a minimum distance of 50 nm is applied between the scatterers (see Figs. 4.15(c) and (d)).

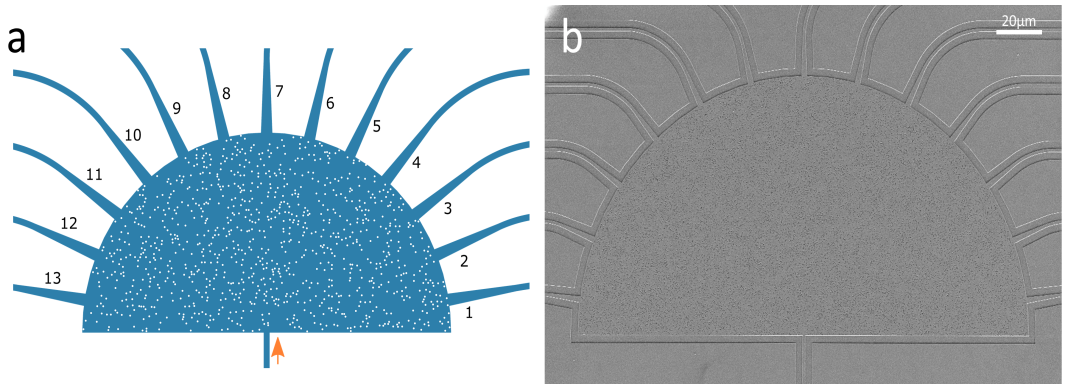

Figure 4.14: (a) Schematic of the random spectrometer. An input waveguide delivers light into the center of the semicircular scattering area and after multiple scattering, the signal is detected at the 13 readout waveguides along the circumference of the scattering area, or escapes into free space. (b) Scanning electron micrograph of the fabricated random spectrometer, composed of a semicircular scattering area with radius $L = 100$ µm, which consists of a random array of identical pores with radius 125 nm and covers the 5% of the scattering area.

In order to reconstruct the input signal, the transmission matrix T is calibrated by recording the wavelength-dependent transmitted light on the 13 detectors. Moreover, the intensity distribution of light in one spectral channel is stored in the respective column of the transmission matrix T by utilizing several tunable laser sources (Santec TLS510, Superlum BS930 and NewFocus TLB6700) in the telecom, NIR, and visible wavelength

regime, respectively, measuring one column of the transmission matrix at a time. Since the probe signals belong to different spectral regions, the calibration occurs only for the respective spectral windows. The number of independent spatial channels defines the number of the simultaneously measured independent spectral channels (a bandwidth of $2M\delta\lambda$ corresponds to M detectors). Therefore, a window of 40 nm (1530 −1570 nm), 15 nm (950 −965 nm), and 15 nm (765 −780 nm) occurs in the telecom, NIR, and visible wavelength range, respectively. The spacing between the spectral channels in the different wavelength regions is 0.1 nm.

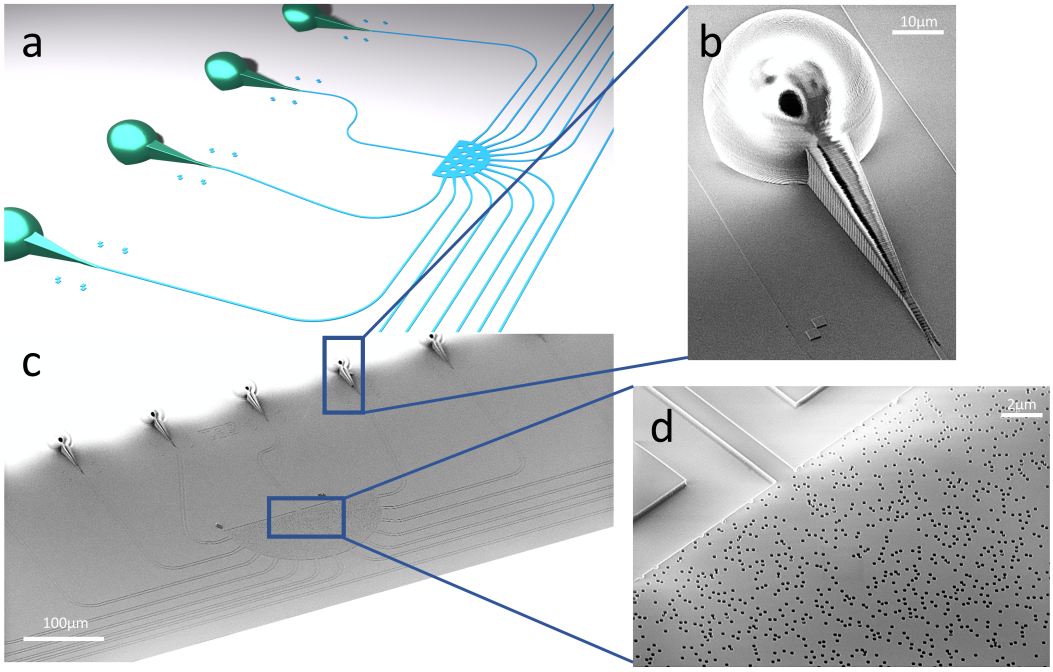

Figure 4.15: (a) Schematic representation of the spectroscopic device. (b) Scanning electron micrograph image of the 3D polymer fiber-to-waveguide coupler. (c) Scanning electron micrograph image of the spectroscopic device. (d) Scattering region of the spectrometer (composed of a random array of identical pores). Despite the fact that a minimum distance of 50 nm is applied between the scatterers, some of them still overlap due to fabrication imperfection.

A comprehensive study conducted by Hartmann et al. [P3], in order to obtain spectroscopic devices with high spectral resolution, for TE-polarized light, by measuring the transmission matrix T and calculating the respective HWHM (see Eq. 4.1). The study is confined only in the telecom wavelength region, where the fabrication is faster due to the in-plane grating couplers and includes a variation of: the radius of the scattering area from 20 µm to 140 µm with a step of 20 µm, the radius of the pores from 50 µm to 200 µm with a step of 20 µm and the filling fraction from 5% to 23% with a step of 2%, while the total amount of the measured devices is 560. According to the results, a random spectrometer exhibits the highest spectral resolution, for TE-polarization, when is

composed of a semicircular scattering area, which consists of a random array of identical pores (125 nm radius) with filling fraction of 5%.

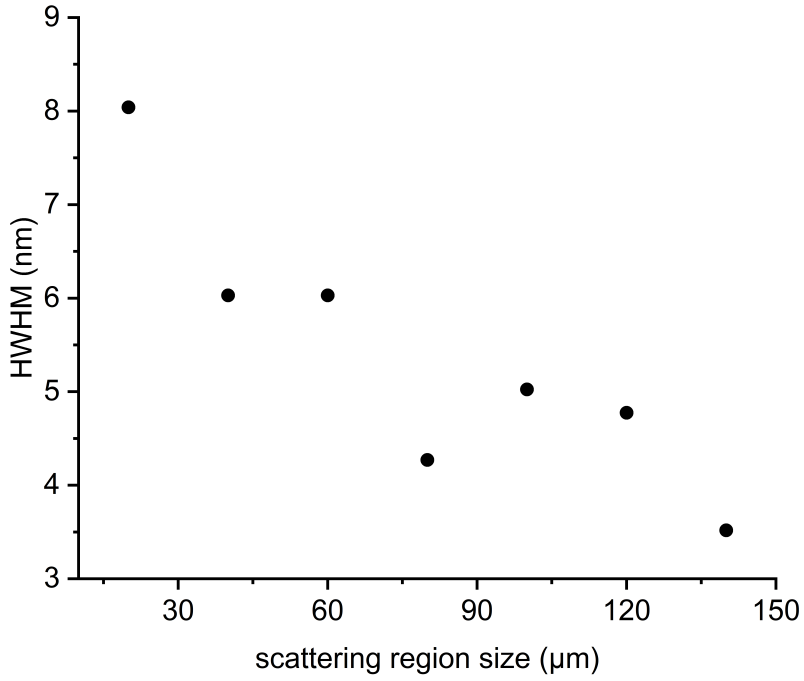

Figure 4.16: Variation of the HWHM of the correlation function obtained from a random spectrometer, composed of a semicircular scattering area, which consists of a random array of identical pores with fixed radius 125 nm and filling ratio 5%, versus the radius of the scattering area L (scattering region size).

Another important parameter is the radius of the scattering area L. Since the spectral resolution scales as $1/L^2$ [21], the HWHM decreases (see Fig. 4.16) while increasing the radius of the scattering area due to the fact that larger scattering areas with fixed filling fraction ($f = 5\%$) consist of more scatterers and therefore more scattering events occur.

In order to provide an estimate of the attainable device performance, Hartmann et al. [P3] measured the total transmission into the 13 output ports (including out-couplers), normalized to the transmission of a reference waveguide (without scattering area but complete with in- and out-coupler). Therefore, an estimate for the total transmission of the device only, i.e., for the random spectrometer without coupling structures but including out-of-plane losses is provided. The results are depicted in Fig. 4.17 (a) for the telecom and in Fig. 4.17 (b) for the visible wavelength range. In the telecom wavelength regime, the total transmission is around -30 dB, while for shorter wavelengths (765 nm -780 nm), we observe an even lower transmission (around -40 dB) due to the fact that moving to visible wavelength regime, the scattering efficiency (see Fig. 4.2) increases

monotonously and therefore, the overall stronger scattering leads to higher out-of-plane losses.

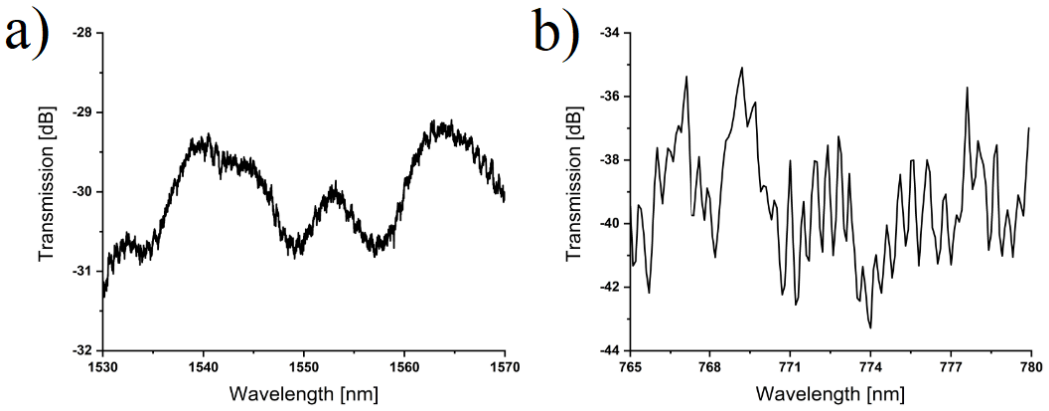

Figure 4.17: Frequency-resolved measured total transmission into the 13 output ports (including out-couplers) of a random spectrometer with filling ratio f = 5% and scattering area of radius $L = 100\,\mu m$ in the (a) telecom and (b) visible wavelength regime. The total transmission is normalized to the transmission of a reference waveguide (including in- and out-couplers) so that the results characterize the actual random spectrometer device including out-of-plane losses.

In order to reconstruct a discretized input signal, the transmission matrix T is calibrated in the different wavelength regions. As we can see in Fig. 4.18 (a), the intensity distribution at telecom wavelengths is characterized by high concentrations in the central readout waveguides with a HWHM of 3.41 nm (Fig. 4.18 (b)). In the NIR wavelength part of the spectrum (950 nm-965 nm), the diffusive regime becomes more dominant due to reduced transport mean free path (see Fig. 4.2 (c)) and therefore, a more uniform distribution along with stronger decorrelation of light is obtained (HWHM = 0.8 nm). Upon moving to shorter wavelengths (765 nm-780 nm), we obtain the highest resolution (HWHM = 0.4 nm) where at the same time the transmission matrix is characterized by sharp intensity peaks due to further decrease of the transport mean free path. It is worth noting that the HWHM in the telecom, NIR, and visible wavelength regime obtained from the experiment is smaller than the respective HWHM predicted by the theory [P1], due to the fact that the radius of the scattering area of the experimental device ($L = 100\,nm$) is significantly larger than the radius of the scattering area of the simulated spectrometer ($L = 25\,nm$).

As we already mentioned, the simple approach by inverting the transmission matrix $S = T^{-1}I$ in order to reconstruct the input signal fails, since the matrix inversion is susceptible to the experimental noise. To overcome this issue, a combination of a

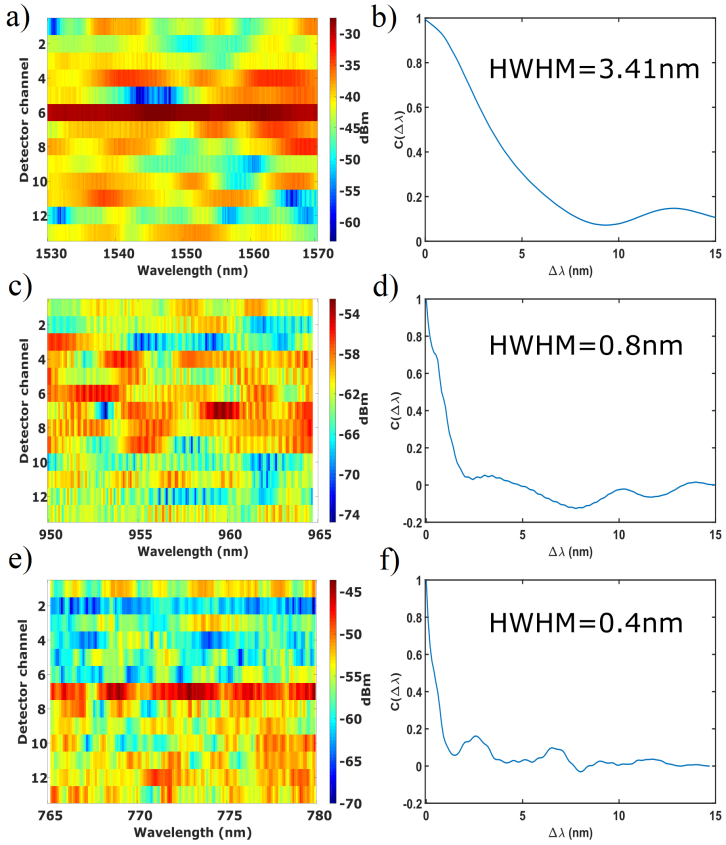

Figure 4.18: Panels (a), (c) and (e): Wavelength- and detector-resolved transmission matrix of a random spectrometer, composed of a scattering area of radius $L = 100\,\mu m$, which consists of a random array of identical pores with radius 125 nm and filling ratio 5%, for TE-polarization, in the telecom, NIR, and visible wavelength regime, respectively. Light is launched from the input waveguide and is detected by the detectors D_1 to D_{13}. The ordinate labels correspond to the detector index. The color coding corresponds to the relative intensity transmitted into the different waveguides and expressed in decibels. Panels (b), (d) and (f): The normalized spectral correlation function corresponds to the wavelength regimes of panels (a), (c) and (e).

truncated singular value decomposition method with a non-linear optimization approach which minimizes $\|I - TS\|^2$ is employed [37, 38]. As shown in Fig. 4.19, the input signal spectra for multiple narrow spectral lines across the telecom, NIR, and visible wavelength region is accurately recovered. Moreover, in order to test the limit of the spectral resolution in the telecom, NIR, and visible regime, a reconstruction of two probe signals spectrally separated by 3 nm, 1 nm, and 0.3 nm, respectively, is successfully attempted (see Fig. 4.19). Therefore, the realization of broadband on-chip random spectrometers with high spectral resolution is achieved [P3], where at the same time the experimental results and the theoretical findings show good agreement.

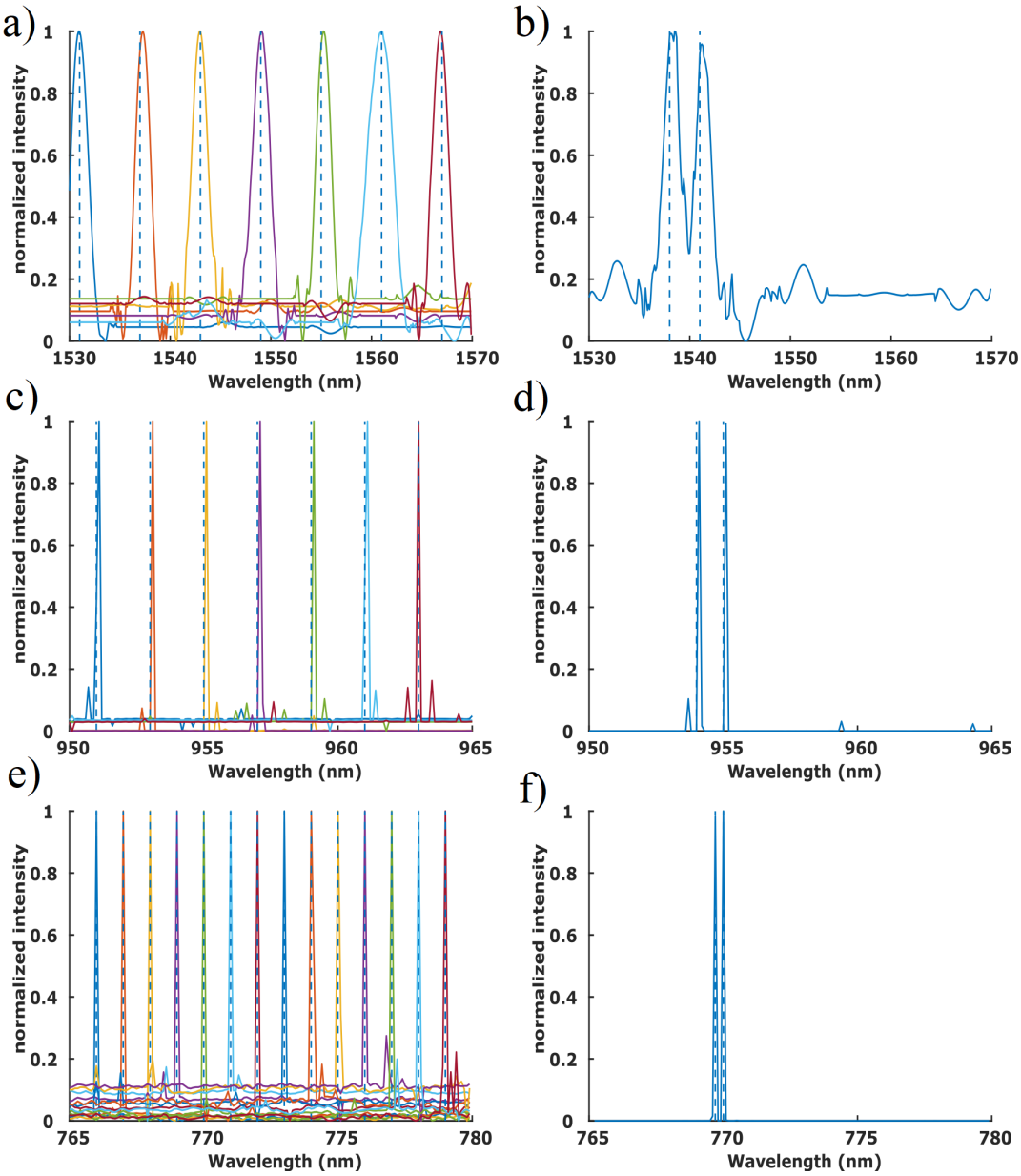

Figure 4.19: Panels (a), (c) and (e): reconstructed spectra for multiple narrow spectral lines across the telecom, NIR, and visible wavelength range, respectively. The dotted lines represent the probe signals, which are spectrally separated by 6 nm, 2 nm and 1 nm, respectively. Panels b), d) and f): reconstruction of two probe signals in order to test the spectral resolution, separated by 3 nm, 1 nm, and 0.3 nm, respectively.

In summary, we studied the optical response of planar spectrometers based on disordered waveguides. Moreover, we have shown that for low density of scatterers, the

spectral resolution depends on the scattering efficiency and asymmetry parameter of a single scatterer. Furthermore, high spectral resolution is obtained in the NIR and visible regime due to reduced transport mean free path. Finally, direct comparison with experimental results [P3] showed that our design studies can be utilized for the realization of broadband spectroscopic devices with high spectral resolution.

CHAPTER 5

Enhanced backscattering in plasmonic silver-coated dielectric nanospheres

Light scattering by small particles can find many applications on several aspects of physics, such as spectroscopy, astrophysics, nuclear physics, meteorology, sensing, optical communications and biophysics [3, 39]. Moreover, plasmonic nanoparticles are suitable for enhancing the light-matter interaction due to their ability to confine light in subwavelength volumes and achieve huge local field enhancement at specific frequencies that can be tuned within a relatively broad spectrum by changing the corresponding materials and geometrical parameters [40].

Along with the enhanced light-matter interaction, scattering directionality is another important parameter regarding many applications. Moreover, the control of the directionality of scattered light relies mostly on the optimization of the interference between the electric and magnetic behaviour of the scatterer. By studying hypothetical spheres with identical electric permittivity and magnetic permeability [41–43], Kerker et al. theoretically predicted that is possible to obtain both zero-backward-scattering and near-zero-forward scattering (Kerker conditions). Although Kerker conditions rely on the interference of electric and magnetic dipoles [44, 45], mostly obtained by small dielectric particles of high refractive index [46, 47], a generalized Kerker condition based on the interference of electric dipole and electric quadrupole moments is also reported [48]. Another category of materials, such as magneto-optical materials, has been also used for achieving high directional light scattering [49–51]. Controlling the direction of scattered light can also achieved by all-dielectric [52] and magneto-electric [53] core-shell spheres. Although zero-backward-scattering and near-zero-forward scattering manifest at a narrow spectral region, recently has been shown that metallo-dielectric core-shell nanoparticles beyond the dipole limit [54] exhibit broadband zero-backward and near-zero-forward scattering. Moreover, broadband suppression of backscattering

at optical frequencies using wavelength-sized dielectric spheres with low permittivity is reported [55].

However, for many applications based on multiple light scattering, preferential backscattering is generally desired. In the case of backscattering, the average cosine of the scattering angle, the so-called asymmetry parameter g is negative. When the radius of the scatterer is much shorter than the incoming wavelength, the scattering is isotropic and hence $g \sim 0$, while for Mie scatterers of radius equal or longer than the incident wavelength, the scattering is mostly forward and $g \sim 1$. In general, negative asymmetry parameter hardly occurs in nature. It has been shown that magnetic particles with large values of permeability [56] and lossless dielectric nanospheres (silicon or germanium) [57] exhibit negative g in the infrared region. In addition, the application of an external magnetic field breaks the scattering isotropy for magneto-optical cylinders in the dipole regime. This break of symmetry leads to preferential backward scattering [34]. Moreover, short-range correlated disorder systems exhibit negative values of the asymmetry parameter [58] and have been associated with enhanced backscattering at Bragg-like matching resonances [59]. In these cases, the negative asymmetry parameter leads to an unusual multiple light scattering regime where the extinction mean free path is longer than the transport mean free path [57].

In this work [P4], we present an alternative strategy to achieve preferential backscattering by using composite plasmonic nanoparticles with core-shell morphology. We show that the attainment of negative g rely on the interference of the hybrid plasmon modes and we propose simple design rules for achieving preferential backscattering along with strong light-matter interaction.

5.1 Asymmetry parameter in dielectric nanospheres

We assume a homogeneous sphere of radius $S = 100\,\text{nm}$ characterized by EM parameters $\epsilon = 4$ and $\mu = 1$, in air. The scattering efficiency spectrum of the scatterer in the visible region manifests two pronounced peaks at the blue end of the spectrum. The long wavelength spectral peak stems from a combination of magnetic and electric type of dipole Mie-resonance modes, while for the short wavelength spectral peak quadrupole Mie-resonance modes of both types are also involved (Fig. 5.1(b)). Due to the interference between the magnetic and electric dipole moment, the asymmetry parameter is positive and therefore light scatters mostly in the forward direction. Moreover, as shown in Fig. 5.1(b), the magnetic and electric dipole moment overlap at $\lambda = 350\,\text{nm}$ and $\lambda = 459\,\text{nm}$, where the first Kerker condition is fulfilled ($a_1 = b_1$). Especially at the long wavelength ($\lambda = 459\,\text{nm}$), where there are no higher order contributions and therefore the first Kerker condition is fully fulfilled, the constructive interference is maximum and a peak ($g = 0.55$) in the asymmetry parameter spectrum is observed (Fig 5.1(c)). However, moving to shorter wavelengths, due to the fact that second order multipole contributions become significant, the first Kerker condition at $\lambda = 350\,\text{nm}$ is only partially fulfilled (for $n = 1$ and not for $n = 2$) and consequently, the asymmetry parameter is slightly reduced. It is worth noting that third and even higher order multipole con-

tributions ($n = 3, ...$) are negligible due to the size of the scatterer with respect to the incident wavelength.

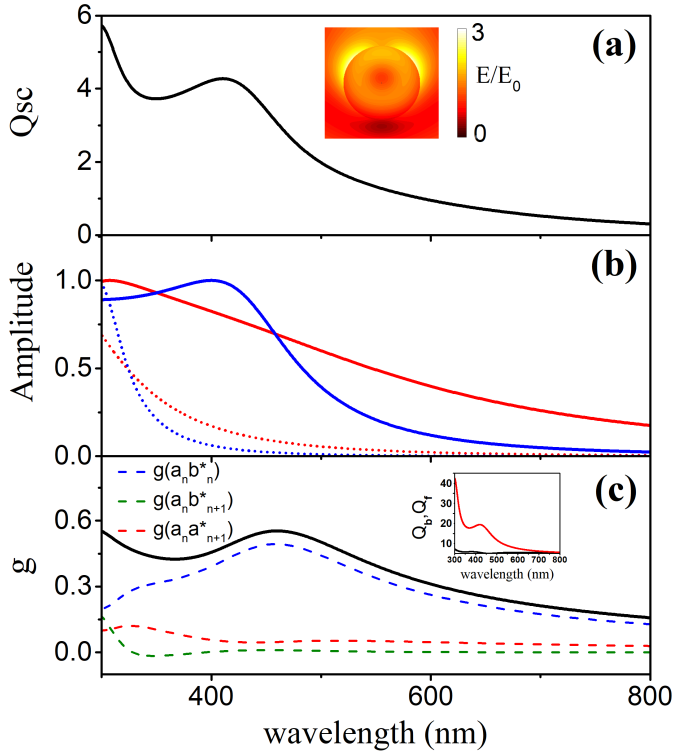

Figure 5.1: (a) Scattering efficiency Q_{sc} of a dielectric sphere of radius $S = 100\,\text{nm}$ with permittivity $\epsilon = 4$, in air. The relative (with respect to the incident plane wave) electric field amplitude distribution in the plane of polarization, at the resonance wavelength, is depicted in the inset. (b) Electric (red lines) and magnetic type (blue lines) Mie coefficients for $n = 1$ (solid lines) and $n = 2$ (dashed lines). (c) Asymmetry parameter g and the contribution of the corresponding terms (Eq. 2.23). Inset: Corresponding backward (black line) and forward (red line) scattering efficiency (see Eqs. 2.21 and 2.22, respectively).

5.2 Asymmetry parameter in plasmonic-coated dielectric nanospheres

We consider now a composite particle, composed of a spherical core of radius 90 nm, characterized by EM parameters $\epsilon = 4$ and $\mu = 1$, coated with a concentric spherical silver shell, 10 nm thick. In this case, since there are two dielectric-metal interfaces, particle- and cavity-like plasmon modes are formed at the outer and inner surfaces of the shell, respectively. These modes interact with each other and give rise to hybrid plasmon modes, by analogy to the formation of bonding and antibonding electron states of a molecule by symmetric and antisymmetric linear combination of the atomic orbitals,

respectively [60–62]. The short wavelength antibonding hybrid mode is mostly localized about the shell, whereas the long wavelength bonding hybrid mode extends in the core region. The particle- and cavity-like dipoles as well as the quadrupole plasmon modes are manifested as peaks in the scattering cross section spectrum. Higher order multipole plasmon modes have a long lifetime and are washed out by dissipation. In our calculations, we employ the actual optical constants of silver, deduced from the experiment [63]. As shown in Fig. 5.2(b), the long wavelength plasmon modes are mainly of electric type (red lines), while the short wavelength particle-like plasmon mode is a combination of electric and magnetic type.

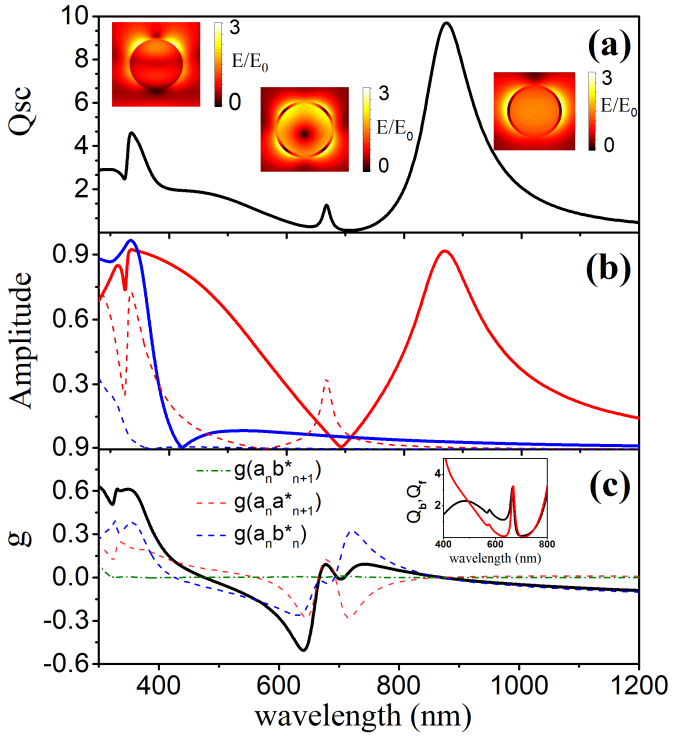

Figure 5.2: (a) Scattering efficiency Q_{sc} of a composite nanoparticle, composed of a dielectric core of radius 90 nm and permittivity $\epsilon = 4$, coated with a concentric silver shell, 10 nm thick, in air. The relative (with respect to the incident plane wave) electric field amplitude distributions in the plane of polarization, at the three resonances, are depicted in the inset. (b) Electric (red lines) and magnetic type (blue lines) Mie coefficients for $n = 1$ (solid lines) and $n = 2$ (dashed lines). Asymmetry parameter g and the contribution of the corresponding terms (see Eq. 2.23). Inset: Corresponding forward (red line) and backward (black line) scattering efficiency. In the wavelength range where $g < 0$, we obtain $Q_b > Q_f$.

The interference between the electric and magnetic type Mie coefficient, for $n = 1$, gives rise to negative asymmetry parameter as we observe from the corresponding term $\text{Re}\left(a_n b_n^*\right)$ (Fig. 5.2(c)). Moreover, another mechanism occurs at the same wavelength

region. The overlap of the electric dipole and quadrupole moment enhances the backscattering and the asymmetry parameter exhibits at $\lambda_1 = 640\,\text{nm}$, a minimum $g = -0.51$. Therefore, for a low density dispersion of such scatterers, a peculiar regime occurs (see Eq. 2.24), where the extinction mean free path is longer than the transport mean path. It is worth noting that the backscattering occurs at wavelengths where the scattering efficiency is relatively low. By adjusting the geometrical parameters, like the thickness of the shell, we can achieve backscattering combined with strong light-matter interaction.

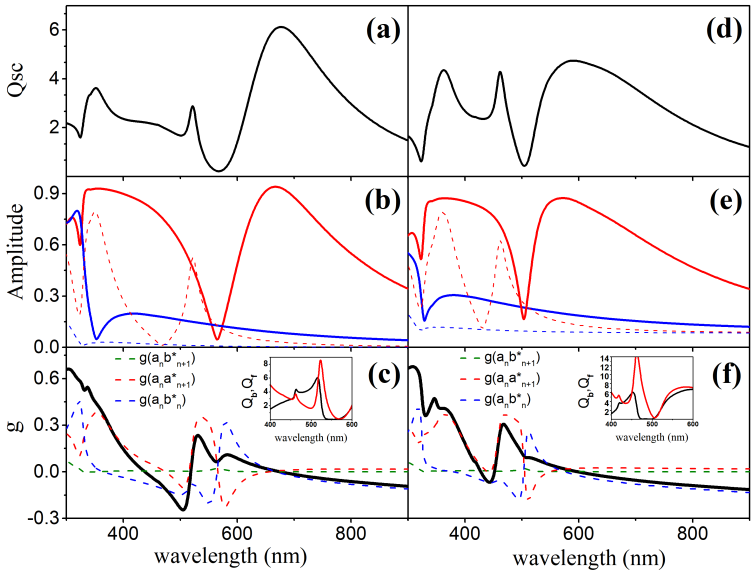

Figure 5.3: Panels (a), (b) and (c): Scattering efficiency, Mie coefficients of electric (red lines) and magnetic type (blue lines) for $n = 1$ (solid lines) and $n = 2$ (dashed lines), asymmetry parameter and the contribution of the corresponding terms of a composite nanoparticle, composed of a dielectric core of radius 80 nm and permittivity $\epsilon = 4$, coated with a concentric silver shell, 20 nm thick, in air, respectively. Panels (d), (e) and (f): Scattering efficiency, Mie coefficients of electric (red lines) and magnetic type (blue lines) for $n = 1$ (solid lines) and $n = 2$ (dashed lines), asymmetry parameter and the contribution of the corresponding terms of a composite nanoparticle, composed of a dielectric core of radius 70 nm and permittivity $\epsilon = 4$, coated with a concentric silver shell, 30 nm thick, in air, respectively. In both cases, the total radius of the scatterer is 100 nm. Insets: Corresponding forward (red line) and backward (black line) scattering efficiency. In the wavelength range where $g < 0$, we obtain $Q_b > Q_f$

In Fig. 5.3, we display a systematic variation of the plasmon modes and the corresponding asymmetry parameter with respect to the shell thickness. By increasing the shell thickness, the resonances come closer and the antibonding plasmon modes at lower wavelengths are more pronounced due to the weaker plasmon hybridization. In this way, we can achieve stronger scattering for the wavelengths where the backscattering

occurs. It is worth noting that for thicker shells, the asymmetry parameter takes on smaller negative values due to the fact that the terms $\mathrm{Re}\left(a_n b_n^*\right)$ and $\mathrm{Re}\left(a_n a_{n+1}^*\right)$ (see Eq. 2.23) interact destructively. Therefore, the choice of the shell thickness depends on the desired characteristics. Thicker shells lead to a stronger scattering and reduced backscattering, while, in contrast, thinner shells offer stronger backscattering along with weak light-matter interaction.

5.3 Asymmetry parameter in plasmonic-coated dielectric nanocylinders

A similar analysis holds for 2D cylindrical scatterers. We assume an infinite plasmonic-coated cylinder of radius $S = 100\,\mathrm{nm}$, composed of a dielectric core ($\epsilon = 4$), coated with a concentric spherical silver shell, in air. In Fig. 5.4, we perform a systematic variation of the scattering efficiency and the asymmetry parameter with respect to the shell thickness. In all cases, we observe that due to the interference of the plasmon modes, the asymmetry parameter takes on high positive and negative values. Therefore, by adjusting the thickness of the shell, we can obtain high directional scattering also in 2D cylindrical scatterers.

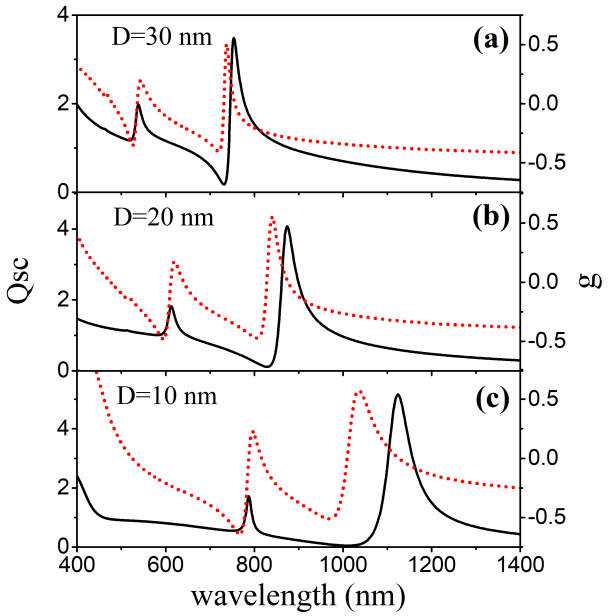

Figure 5.4: Variation of the scattering efficiency (black solid lines) and asymmetry parameter (red dotted lines) spectra (solid lines) of an infinite dielectric cylinder, coated with a concentric silver shell, in air, versus the thickness D of the shell. In all cases, the radius of the scatterer is $S = 100\,\mathrm{nm}$.

In summary, through Mie theory, we have shown that composite plasmonic nanoparti-

cles with dielectric-metal core-shell morphology exhibit negative asymmetry parameter due to the interference of the hybrid plasmon modes at the outer and inner surface of the shell. Morever, by properly adjusting the thickness of the shell, we can obtain preferential backscattering along with strong light-matter interaction.

CHAPTER 6

Enhanced Faraday rotation in shape-modified magneto-optical metasurfaces

Magneto-optical nanostructures (MO) exhibit intriguing optical properties and offer impressive opportunities for tailoring the light-matter interaction at the nanoscale. Due to the fact that the MO effects are rather weak in the optical domain, the enhancement of the MO response is crucial for many photonic applications based on miniaturized isolators.

Enhanced Faraday effects, in the context of strong field localization in the active magnetic region, have been reported in one dimensional magnetophotonic crystals. For instance, single cavity structures composed of a magnetic thin film, sandwiched between two dielectric Bragg mirrors [64, 65], and magnetic/dielectric multilayer fields [66, 67] enhance the Faraday effect at the cavity resonant wavelength and at the photonic band edges, respectively.

At the same time, composite nanostructures composed of magnetic materials and noble metals exhibit large Faraday rotation due to the plasmon driven strong field enhancement in the vicinity of the MO material. Moreover, a combination of large Faraday rotation and high transmittance can occur in perforated metallic films [68–70] and metallic gratings [71, 72], optically coupled with magnetic materials. Significantly enhanced Faraday rotation, due to plasmonic and MO properties, was also reported in other geometries, such as metallic nanoparticles [73–77], core-shell particles [78–80] and multilayers [81–83]. However, magnetoplasmonic structures show relatively low transmittance due to absorptive losses.

Recently, enhanced MO response was measured in high permittivity nanoantennas covered with a magnetic film [84]. High index dielectric nanoparticles provide impressive opportunities for field localization due to the electric and magnetic Mie resonances accompanied with low optical losses. Importantly, the spectral overlap of electric and magnetic dipole resonances in all-dielectric metasurfaces results

in almost 100% transmission [85]. Therefore, it has been shown that all-dielectric magneto-optical metasurfaces exhibit enhanced Faraday rotation along with near-unity transmittance [86].

In the present work [P5], we seek to obtain an enhanced Faraday rotation along with high transmittance in all-dielectric metasurfaces composed of shape-modified magnetic (Ce:BIG) nanoscatterers. For the above purpose, a random search is applied to acquire the possibly best-shaped scattering structure out of a predefined geometry configuration space. For all structures, a Discontinuous Galerkin Time-Domain method (DGTD) [7] is employed to compute both the Faraday rotation and transmission spectrum.

6.1 Enhanced Faraday rotation by metasurfaces of nanodisks

We first consider a square array of period $P = 850\,\text{nm}$, composed of magneto-optical nanodisks of radius $R = 360\,\text{nm}$ and height $H = 260\,\text{nm}$, which can be described by a scalar relative magnetic permeability $\mu_g = 1$ and a relative electric permittivity tensor

$$\overleftrightarrow{\epsilon_g} = \begin{pmatrix} \epsilon & -ig & 0 \\ ig & \epsilon & 0 \\ 0 & 0 & \epsilon \end{pmatrix}, \tag{6.1}$$

if we take the gyration vector along the z-axis, with $\epsilon = 6.25$ and $g = 0.06$ [87]. Accordingly, the host medium is characterised by $\epsilon_h = 2.1$ and $\mu_h = 1$. The transmission

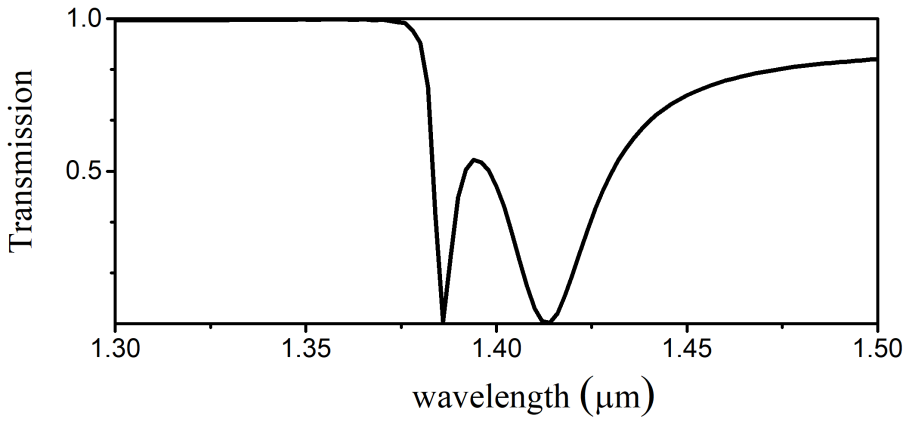

Figure 6.1: Transmission spectrum of light normally incident on a square array of period $P = 850\,\text{nm}$, composed of magneto-optical nanodisks of radius $S = 360\,\text{nm}$ with $\epsilon = 6.25$ and $g = 0.06$, in a host medium with $\epsilon_h = 2.1$.

spectrum (see Fig. 6.1) of light, normally incident ($\mathbf{k} = k\hat{\mathbf{z}}$) on the metasurface and with the polarization direction along the x-axis, is characterised by two well spectrally

separated minima, where the transmission vanishes, at $\lambda \sim 1.39\,\mu m$ and $\lambda \sim 1.42\,\mu m$, stemming from single scattering dipole resonances of magnetic and electric type, respectively. Since high transmission is essential for many photonic applications, it is necessary to convert our metasurface into Huygens' metasurface by adjusting the geometrical parameters of the single disks in order to obtain spectrally overlapping electric and magnetic dipole resonances [85]. In Fig. 6.2, we depict the transmission spectrum for the case of the overlapping resonances where the radius of the disks is reduced and equals 310 nm. The two resonances overlap at $\lambda \sim 1.35\,\mu m$ and the transmission is almost 100%. The transmitted wave is generally elliptically polarized with ellipticity angle χ and the long axis of the ellipse forms an angle θ with the polarization direction of the incident wave. It is worth noting that when the ellipticity angle vanishes ($\chi = 0$), the transmitted wave is linearly polarized. The light-matter interaction is enhanced due to the overlapping of the dipole resonances at $\lambda \sim 1.35\,\mu m$ and therefore, we obtain a Faraday rotation angle of $\theta = -7.5°$ (see Fig 6.2 (b)), which is a ten times enhancement of the -0.75° induced by the corresponding solid film of the same thickness [86]. In order

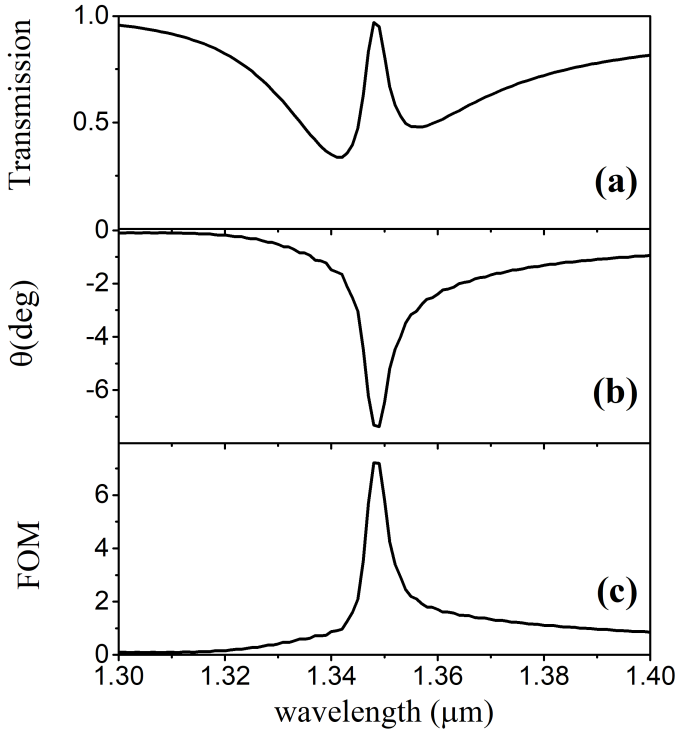

Figure 6.2: (a) Transmission spectrum of light incident normally on a square array of period $P = 850\,nm$, composed of magneto-optical nanodisks of radius $S = 310\,nm$ with $\epsilon = 6.25$ and $g = 0.06$, in a host medium with $\epsilon_h = 2.1$. (b) Corresponding Faraday rotation angle. (c) Figure of merit (FOM) between Faraday rotation angle θ and transmission T.

to estimate a trade-off between the transmission and Faraday rotation, we define a figure

of merit (FOM) [69, 86]

$$\mathrm{FOM} = \sqrt{T}|\theta| \ . \tag{6.2}$$

Since the enhanced Faraday rotation angle is accompanied with high transmission, we obtain a FOM of 7.35 ($\lambda \sim 1.35\,\mu\mathrm{m}$), as can be seen in Fig. 6.2 (c).

6.2 Enhanced Faraday rotation by metasurfaces of shape-modified nanodisks

We investigate now a periodic square array composed of shape-modified magneto-optical nanodisks. The initial shape of the scatterers is a nanodisk of radius $S = 360\,\mathrm{nm}$ and height $H = 260\,\mathrm{nm}$, located within a unit-cell of period $p_x = p_y = 850\,\mathrm{nm}$. For each scatterer, we choose a set of $4N$ equiangular distributed points $\mathbf{r}_i = (x_i, y_i) = (r_i \sin(i\Delta\phi), r_i \cos(i\Delta\phi))$ with radial positions $\mathbf{r}_i$, chosen between a minimal circular radius $r_{\min}$ and a minimal distance d to the unit-cell boundary and with a separation angle $\Delta\phi = \frac{2\pi}{4N}$. The control points ($\mathbf{r}_i$) are connected through a spline curve as shown in Fig. 6.3 (a). To avoid a self-intersecting spline, we smooth (cf. Fig 6.3 (b)) the neighboring point positions by employing Gaussian weights:

$$\tilde{\mathbf{r}}_i = \frac{\sum_j w_{ij}\mathbf{r}_j}{\sum_j w_{ij}}, \quad \text{with} \quad w_{ij} = \exp\left(-|\phi_i - \phi_j|^2 \langle|\mathbf{r}|\rangle^2 / L^2\right) \ , \tag{6.3}$$

where $L = f r_{\min}\Delta\phi$ is the correlation length with a correlation factor f varying between $f \in [4.5, 5.5]$ and $\phi_i = i\Delta\phi$. In order to preserve the polarization independence in x- and y-direction, we impose a fourfold circular symmetry. For the spatial discretization of the scattering geometry, we use an adaptive tetrahedral mesh by utilizing the freely available mesher *Gmsh* [88]. Moreover, the computational domain (cf. Fig 6.3 (c)) consists of a surrounding medium (SiO_2) with a height of 1500 nm, a TfSf contour from where we launch a Gaussian modulated plane wave and contours for recording the Poynting flux. To terminate the simulation domain, we employ the Silver-Müller boundary conditions and to avoid back reflection of the outgoing radiation, we surround the computational domain with 500 nm thick layer of uPML at the top and bottom of the computational domain. Finally, we employ periodic boundary conditions along the x- and y-directions.

To find the best trade-off between the transmittance T and Faraday rotation angle θ, we define a FOM as [86]

$$FOM = \begin{cases} \max_\lambda |\theta(\lambda)|\sqrt{T(\lambda)} & \text{for} \quad T(\lambda) > 0.3 \\ 0 & \text{else} \end{cases} \tag{6.4}$$

where the cut-off ($T(\lambda) > 0.3$) ensures a relatively high transmission. After a random search (by randomly changing the radial positions $\mathbf{r}_i$), we find the modified shape that corresponds to the highest FOM. The results shown in Fig. 6.4 (b), are obtained by full electrodynamic calculations utilizing a discontinuous Galerkin time-domain (DGTD)

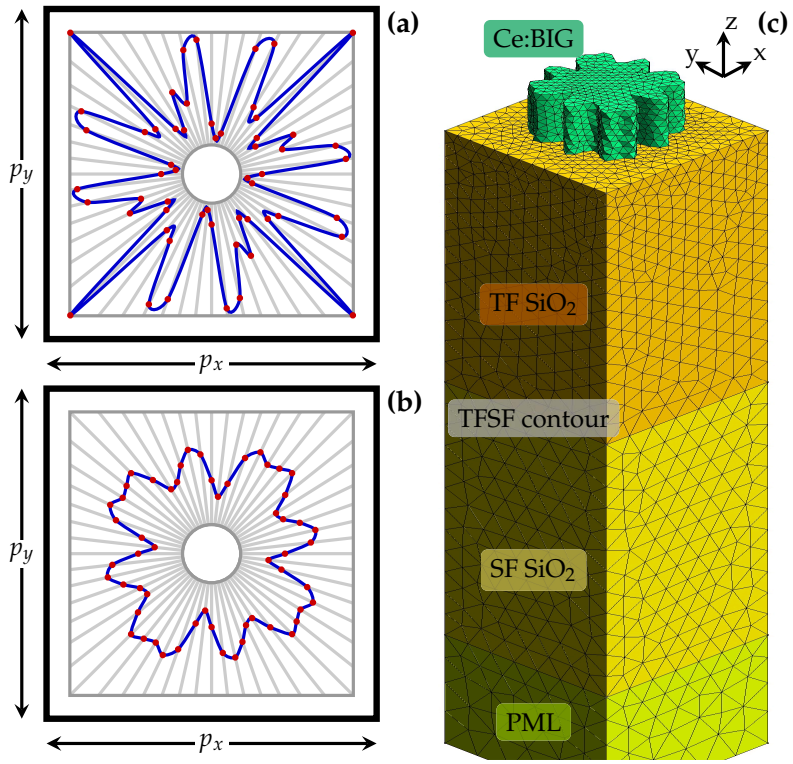

Figure 6.3: Modified shape and setup generation: (a) Construction of scatterer surface line with a spline using a set of control points $\mathbf{r}_i$. (b) Spline after application of Gaussian smoothing filter to the control points. (c) Computational domain.

finite-element approach [7] that we properly extended to non-dispersive anisotropic materials by implementing [P5] a well-suited numerical flux [89, 90]. Within this approach, the time-stepping is handled by a 14-stage fourth-order low-storage-Runge scheme [8]. After a Fourier transform of the (time-dependent) Poynting flux, we recover the frequency-resolved transmission spectra $T(\lambda)$ and the corresponding E-field components in order to calculate the Faraday rotation $\theta(\lambda)$ and ellipticity $\phi(\lambda)$ spectra with a single time-domain computation.

For a square array of shape-modified magneto-optical nanodisks, we display in Fig. 6.4 both the transmittance and Faraday rotation angle. Moreover, the transmission spectrum is characterized by a peak of almost 100% transmittance at $\lambda \sim 1.295\,\mu\text{m}$, a fact that indicates that the shape-modified scatterers still act as Huygens' sources, along with enhanced Faraday rotation angle $\theta = 13°$ (see Fig. 6.4 (b)). The corresponding modified cross section of a single scatterer is shown in Fig. 6.3 (b). Since the enhancement of the Faraday rotation is much stronger than in the case of simple nanodisks [86], we obtain a figure of merit $FOM = 13$ (see Fig. 6.4 (c)), which is almost a 2 times enhancement of the $FOM = 7.35$ induced by the metasurface of nanodisks (see Fig. 6.2 (c)).

In summary, we have shown the existence of enhanced Faraday rotation along with

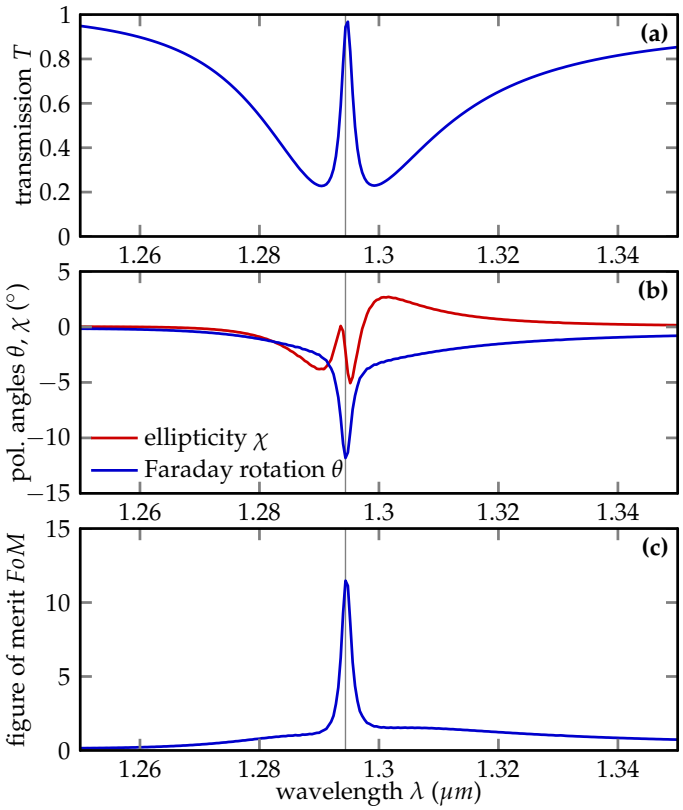

Figure 6.4: (a) Transmission spectrum of the shape-optimized scattering structure, (b) Corresponding Faraday rotation θ and ellipticity χ angle. (c) Figure of merit between the Faraday rotation angle and transmission.

almost 100% transmittance in all-dielectric magneto-optical metasurfaces composed of shape-modified nanodisks. This high figure of merit between the Faraday rotation and transmission can be obtained by setting a number of control points along the circumference of the nanodisks and randomly changing their radial position. It is worth noting that we can optimize the afore-described magneto-optical structure by applying an optimization algorithm in order to acquire the possibly best-shaped scatterers. In this regard, preliminary results obtained by means of full electrodynamic simulations in conjunction with a genetic algorithm, show similar magneto-optical response and shape modification [P5].

CHAPTER 7

Conclusions

In this thesis, we have studied the optical response of planar random spectrometers in the telecom, NIR and visible wavelength regime by means of full electrodynamic simulations, multiple scattering theory, and Mie theory [P1]. We have shown that in the low concentration limit ($f \leq 0.1$), the spectral resolution depends on two single scattering quantities, the scattering efficiency and the asymmetry parameter. Moreover, at visible wavelengths where the diffusive regime is fully developed, the spectrometers exhibit the highest resolution. On the other hand, at NIR wavelengths where the transition regime between diffusive and ballistic transport occurs, the spectral resolution is sufficiently high for certain applications. Specifically, a transport mean free path of $l_t/L = 0.1$ with respect to the device size L provides the best trade-off between the transmission and spectral resolution. It is worth noting that for higher filling fractions (($f \geq 0.1$), the single scattering properties are washed out by strong multiple scattering corrections. In this high-f regime, the transport mean free path can be determined by an effective medium theory [4]. Based on our design studies, Hartmann et al. [P3] proceeded with the realization of random spectrometers operating in the visible and NIR wavelength regime.

In this regard, Gehring et al. [P2] demonstrated an approach for optical coupling between single-mode fibers and planar photonic circuitry. The contact-free coupling occurs on the top of the chip by utilizing 3D devices obtained by direct laser writing. The couplers manifest low losses in a wide optical bandwidth, independent of periodicity due to near-adiabatic tapering. These properties paved the way towards the realization of random spectrometers operating in a broad wavelength spectrum.

Furthermore, through Mie theory, we have shown the existence of preferential high backscattering by a subwavelength composite nanoparticle with dielectric-metal core-shell morphology [P4]. Such composite nanoparticles offer a versatile platform for engineering hybrid plasmon modes. Moreover, the interaction of the particle- and cavity-like modes give rise to enhanced backward scattering. By properly adjusting the thickness of the shell, we can achieve high backward directionality along with strong scattering. The negative asymmetry parameter leads to an anomalous scattering regime where the

extinction mean free path is longer than the transport mean free path for a dilute suspension of scatterers. Our results could be useful for many applications, such as sensing and spectroscopy.

Finally, we have studied the magneto-optical response of all-dielectric Huygens' metarsufaces composed of shape-modified magneto-optical nanodisks. We have shown that by setting a number of control points along the circumference of the nanodisks and randomly changing their radial position, we can obtain a high figure of merit between the transmittance and Faraday rotation. The figure of merit and consequently, the shape modification of the nanodisks can be optimized by applying a genetic algorithm [P5].

APPENDIX A

Vector identities

Some useful identities which include combinations of inner and vector products are:

$$\mathbf{a}\cdot\left(\mathbf{b}\times\mathbf{c}\right)=\mathbf{b}\cdot\left(\mathbf{c}\times\mathbf{a}\right)=\mathbf{c}\cdot\left(\mathbf{a}\times\mathbf{b}\right) \tag{A.1}$$

$$\mathbf{a}\times\left(\mathbf{b}\times\mathbf{c}\right)=\left(\mathbf{a}\cdot\mathbf{c}\right)\mathbf{b}-\left(\mathbf{a}\cdot\mathbf{b}\right)\mathbf{c} \tag{A.2}$$

$$\left(\mathbf{a}\times\mathbf{b}\right)\cdot\left(\mathbf{c}\times\mathbf{d}\right)=\left(\mathbf{a}\cdot\mathbf{c}\right)\left(\mathbf{b}\cdot\mathbf{d}\right)-\left(\mathbf{a}\cdot\mathbf{d}\right)\left(\mathbf{b}\cdot\mathbf{c}\right)\ . \tag{A.3}$$

The action of the operators $\nabla\cdot$ and $\nabla\times$ on a vector or a combination of two vectors or a combination of a vector and a scalar ϕ can be described by the following identities:

$$\nabla\times\nabla\phi=0 \tag{A.4}$$

$$\nabla\cdot\left(\nabla\times\mathbf{a}\right)=0 \tag{A.5}$$

$$\nabla\times\left(\nabla\times\mathbf{a}\right)=\nabla\left(\nabla\cdot\mathbf{a}\right)-\nabla^2\mathbf{a} \tag{A.6}$$

$$\nabla\cdot\left(\phi\mathbf{a}\right)=\mathbf{a}\cdot\nabla\phi+\phi\nabla\cdot\mathbf{a} \tag{A.7}$$

$$\nabla\times\left(\phi\mathbf{a}\right)=\nabla\phi\times\mathbf{a}+\phi\nabla\times\mathbf{a} \tag{A.8}$$

$$\nabla\left(\mathbf{a}\cdot\mathbf{b}\right)=\left(\mathbf{a}\cdot\nabla\right)\mathbf{b}+\left(\mathbf{b}\cdot\nabla\right)\mathbf{a}+\mathbf{a}\times\left(\nabla\times\mathbf{b}\right)+\mathbf{b}\times\left(\nabla\times\mathbf{a}\right) \tag{A.9}$$

$$\nabla\cdot\left(\mathbf{a}\times\mathbf{b}\right)=\mathbf{b}\cdot\left(\nabla\times\mathbf{a}\right)-\mathbf{a}\cdot\left(\nabla\times\mathbf{b}\right) \tag{A.10}$$

$$\nabla\times\left(\mathbf{a}\times\mathbf{b}\right)=\mathbf{a}\left(\nabla\cdot\mathbf{b}\right)-\mathbf{b}\left(\nabla\cdot\mathbf{a}\right)+\left(\mathbf{b}\cdot\nabla\right)\mathbf{a}-\left(\mathbf{a}\cdot\nabla\right)\mathbf{b}\ . \tag{A.11}$$

We recall some very useful identities which relate volume integrals over volume V enclosed by a surface A, to the corresponding surface integrals over the boundary of volume V. The vector $\widehat{\mathbf{n}}$ is the outward pointing unit normal vector. Divergence theorem:

$$\int_V d^3r\ \nabla\phi = \int_A d^2r\ \widehat{\mathbf{n}}\ \phi\ . \tag{A.12}$$

Gauss's theorem:

$$\int_V d^3r\ \nabla\cdot\mathbf{a} = \int_A d^2r\ \widehat{\mathbf{n}}\cdot\mathbf{a}\ . \tag{A.13}$$

Stokes's theorem:

$$\int_V d^3r\ \nabla\times\mathbf{a} = \int_A d^2r\ \widehat{\mathbf{n}}\times\mathbf{a}\ . \tag{A.14}$$

Green's first identity:

$$\int_V d^3r\Big[\phi_1\nabla^2\phi_2 + \nabla\phi_1\cdot\nabla\phi_2\Big] = \int_A d^2r\ \widehat{\mathbf{n}}\cdot\phi_1\nabla\phi_2\ . \tag{A.15}$$

Green's second identity:

$$\int_V d^3r\Big[\phi_1\nabla^2\phi_2 - \nabla\phi_1\cdot\nabla\phi_2\Big] = \int_A d^2r\ \widehat{\mathbf{n}}\cdot\Big[\phi_1\nabla\phi_2 - \phi_2\nabla\phi_1\Big]\ . \tag{A.16}$$

Green's vector identity:

$$\int_V d^3r\Big[\mathbf{a}\cdot\nabla\times(\nabla\times\mathbf{b}) - \mathbf{b}\cdot\nabla\times(\nabla\times\mathbf{a})\Big] = -\int_A d^2r\Big[\mathbf{b}\cdot\widehat{\mathbf{n}}\times(\nabla\times\mathbf{a}) + (\nabla\times\mathbf{b})\cdot(\widehat{\mathbf{n}}\times\mathbf{a})\Big]\ . \tag{A.17}$$

We can derive the Eq. A.17 by applying the Gauss theorem (A.13) for the vector $\mathbf{b}\times(\nabla\times\mathbf{a}) - \mathbf{a}\times(\nabla\times\mathbf{b})$ instead of the vector $\mathbf{a}$, and by using suitable vector identities. The Eq. A.17 can be generalized also in the case where instead of the vector $\mathbf{b}$ we have a dyadic tensor $\mathbf{B}$. Moreover, for $\mathbf{b} = \mathbf{B}\cdot\widehat{\mathbf{c}}$, where $\widehat{\mathbf{c}}$ is a unit vector, the Eq. A.17 reads

$$\begin{aligned}&\Bigg\{\int_V d^3r\Big\{\mathbf{a}\cdot\Big[\nabla\times(\nabla\times\mathbf{B})\Big] - \Big[\nabla\times(\nabla\times\mathbf{a})\Big]\cdot\mathbf{B}\Big\}\\ &+\int_A d^2r\Big\{\Big[\widehat{\mathbf{n}}\times(\nabla\times\mathbf{a})\Big]\cdot\mathbf{B} + (\widehat{\mathbf{n}}\times\mathbf{a})\cdot(\nabla\times\mathbf{B})\Big\}\Bigg\}\cdot\widehat{\mathbf{c}} = 0\ .\end{aligned}$$

Due to the fact that the above equation holds for any $\widehat{\mathbf{c}}$, we have

$$\begin{aligned}&\int_V d^3r\Big\{\mathbf{a}\cdot\Big[\nabla\times(\nabla\times\mathbf{B})\Big] - \Big[\nabla\times(\nabla\times\mathbf{a})\Big]\cdot\mathbf{B}\Big\}\\ &= -\int_A d^2r\Big\{\Big[\widehat{\mathbf{n}}\times(\nabla\times\mathbf{a})\Big]\cdot\mathbf{B} + (\widehat{\mathbf{n}}\times\mathbf{a})\cdot(\nabla\times\mathbf{B})\Big\}\ .\end{aligned} \tag{A.18}$$

Moreover, if $\mathbf{B} = \mathbf{b_1} \cdot \mathbf{b_2}$, then $\mathbf{a} \cdot \mathbf{B} = (\mathbf{a} \cdot \mathbf{b_1})\mathbf{b_2}$ and $\mathbf{B} \cdot \mathbf{a} = \mathbf{b_1}(\mathbf{b_2} \cdot \mathbf{a})$. Finally, the curl of a dyadic tensor reads

$$\nabla \times \mathbf{B} = \begin{pmatrix} 0 & -\partial_z & \partial_y \\ \partial_z & 0 & -\partial_x \\ -\partial_y & \partial_x & 0 \end{pmatrix} \begin{pmatrix} b_{1x}b_{2x} & b_{1x}b_{2y} & b_{1x}b_{2z} \\ b_{1y}b_{2x} & b_{1y}b_{2y} & b_{1y}b_{2z} \\ b_{1z}b_{2x} & b_{1z}b_{2y} & b_{1z}b_{2z} \end{pmatrix} . \tag{A.19}$$

APPENDIX B

Spherical harmonics

The spherical harmonics, $Y_{lm}(\widehat{\mathbf{r}})$, constitute the angular part of the solutions of Helmholtz equation and satisfy the differential equation

$$\begin{aligned} \nabla^2 Y_{lm}(\widehat{\mathbf{r}}) &= \left[\frac{1}{r^2}\frac{\partial}{\partial r}\left(r^2\frac{\partial}{\partial r}\right) - \frac{\mathbf{L}^2}{r^2}\right] Y_{lm}(\widehat{\mathbf{r}}) = \\ &= -\frac{\mathbf{L}^2}{r^2} Y_{lm}(\widehat{\mathbf{r}}) = -\frac{l\left(l+1\right)}{r^2} Y_{lm}(\widehat{\mathbf{r}}) \ , \end{aligned} \tag{B.1}$$

where $\mathbf{L}$ is the angular momentum operator

$$\begin{aligned} \mathbf{L} &= -i\left(\mathbf{r}\times\nabla\right) = i\left(\widehat{\boldsymbol{\theta}}\frac{1}{\sin\theta}\frac{\partial}{\partial\phi} - \widehat{\boldsymbol{\phi}}\frac{\partial}{\partial\theta}\right) \\ \mathbf{L}^2 &= -\frac{1}{\sin\theta}\frac{\partial}{\partial\theta}\left(\sin\theta\frac{\partial}{\partial\theta}\right) - \frac{1}{\sin^2\theta}\frac{\partial^2}{\partial\phi^2} \ , \end{aligned} \tag{B.2}$$

and the argument $\widehat{\mathbf{r}}$ denotes the dependence of the vector $\mathbf{r}$ on the angles θ and ϕ in the spherical coordinates. The $Y_{lm}(\widehat{\mathbf{r}})$ are given by

$$Y_{lm}(\widehat{\mathbf{r}}) = (-1)^m \sqrt{\frac{2l+1}{4\pi}\frac{(l-m)!}{(l+m)!}}\, P_l^m(\cos\theta) e^{im\phi} \ , \tag{B.3}$$

with $l = 0, 1, \ldots$, $m = -l, -l+1, \ldots, l-1, l$ and $P_l^m(\cos\theta)$ the Legendre polynomials

$$P_l^m(x) = \frac{1}{2^l l!}\left(1-x^2\right)^{m/2}\frac{d^{l+m}}{dx^{l+m}}\left(x^2-1\right)^l \ , \quad x = \cos\theta \tag{B.4}$$

for $m > 0$, while for $m < 0$ are defined by

$$P_l^{-m}(x) = (-1)^m \, \frac{(l-m)!}{(l+m)!} \, P_l^m(x) \; . \tag{B.5}$$

From the above relations arise

$$Y_{lm}^*(\widehat{\mathbf{r}}) = (-1)^m \, Y_{l-m}(\widehat{\mathbf{r}}) \; , \tag{B.6}$$

and

$$Y_{lm}(-\widehat{\mathbf{r}}) = (-1)^l \, Y_{lm}(\widehat{\mathbf{r}}) \tag{B.7}$$

$$Y_{lm}(\theta = 0, \phi) = \sqrt{\frac{2l+1}{4\pi}} \; \delta_{m0} \; . \tag{B.8}$$

The $Y_{lm}(\widehat{\mathbf{r}})$ fulfil the orthonormality and completeness relations

$$\int_0^{2\pi} d\phi \int_0^{\pi} d\theta \sin\theta \; Y_{lm}(\widehat{\mathbf{r}}) Y_{l'm'}^*(\widehat{\mathbf{r}}) = \delta_{ll'} \delta_{mm'} \tag{B.9}$$

$$\sum_{lm} Y_{lm}(\widehat{\mathbf{r}}) Y_{lm}^*(\widehat{\mathbf{r}}') = \delta \left(\widehat{\mathbf{r}} - \widehat{\mathbf{r}}' \right) \; , \tag{B.10}$$

the addition theorem

$$\sum_{m=-l}^{l} \left| Y_{lm}(\widehat{\mathbf{r}}) \right|^2 = \frac{2l+1}{4\pi} \; , \tag{B.11}$$

a set of relations which relate spherical harmonics of different orders

$$\cos\theta Y_{lm}(\widehat{\mathbf{r}}) = \zeta_{l+1}^m Y_{l+1m}(\widehat{\mathbf{r}}) + \zeta_l^m Y_{l-1m}(\widehat{\mathbf{r}}) \tag{B.12}$$

$$e^{i\phi} \sin\theta Y_{lm}(\widehat{\mathbf{r}}) = 2 \left[\gamma_l^{-m} Y_{l-1m+1}(\widehat{\mathbf{r}}) - \gamma_{l+1}^{m+1} Y_{l+1m+1}(\widehat{\mathbf{r}}) \right] \tag{B.13}$$

$$e^{-i\phi} \sin\theta Y_{lm}(\widehat{\mathbf{r}}) = 2 \left[\gamma_{l+1}^{-m+1} Y_{l+1m-1}(\widehat{\mathbf{r}}) - \gamma_l^m Y_{l-1m-1}(\widehat{\mathbf{r}}) \right] \tag{B.14}$$

$$m \cot\theta Y_{lm}(\widehat{\mathbf{r}}) = - \left[\alpha_l^m e^{-i\phi} Y_{lm+1}(\widehat{\mathbf{r}}) + \alpha_l^{-m} e^{i\phi} Y_{lm-1}(\widehat{\mathbf{r}}) \right] \; , \tag{B.15}$$

as well as the relations

$$\frac{\partial Y_{lm}(\widehat{\mathbf{r}})}{\partial\theta} = \alpha_l^m e^{-i\phi} Y_{lm+1}(\widehat{\mathbf{r}}) - \alpha_l^{-m} e^{i\phi} Y_{lm-1}(\widehat{\mathbf{r}}) \tag{B.16}$$

$$= i\psi_l \; X_{lm,\phi}(\widehat{\mathbf{r}}) \tag{B.17}$$

$$\frac{\partial Y_{lm}(\widehat{\mathbf{r}})}{\partial\phi} = im \; Y_{lm}(\mathbf{r}) \tag{B.18}$$

$$= -i\psi_l \; \sin\theta \; X_{lm,\theta}(\widehat{\mathbf{r}}) \; . \tag{B.19}$$

Finally, another useful relation:

$$\begin{aligned}\nabla\left[f_l(qr)Y_{lm}(\widehat{\mathbf{r}})\right] &= f_l(qr)\nabla Y_{lm}(\widehat{\mathbf{r}}) + qf_l^{'}(qr)Y_{lm}(\widehat{\mathbf{r}})\ \widehat{\mathbf{r}} \\ &= i\psi_l\frac{f_l(qr)}{r}\left[X_{lm,\phi}(\widehat{\mathbf{r}})\widehat{\boldsymbol{\theta}} - X_{lm,\theta}(\widehat{\mathbf{r}})\widehat{\boldsymbol{\phi}}\right] \\ &\quad + qf_l^{'}(qr)Y_{lm}(\widehat{\mathbf{r}})\ \widehat{\mathbf{r}}\ . \end{aligned} \tag{B.20}$$

In the above relations

$$\psi_l = \sqrt{l\left(l+1\right)} \tag{B.21}$$

$$\alpha_l^m = \frac{1}{2}\left[\left(l-m\right)\left(l+m+1\right)\right]^{1/2} \tag{B.22}$$

$$\gamma_l^m = \frac{\left[\left(l+m\right)\left(l+m-1\right)\right]^{1/2}}{2\left[\left(2l-1\right)\left(2l+1\right)\right]^{1/2}} \tag{B.23}$$

$$\zeta_l^m = \frac{\left[\left(l+m\right)\left(l-m\right)\right]^{1/2}}{\left[\left(2l-1\right)\left(2l+1\right)\right]^{1/2}}\ , \tag{B.24}$$

and $X_{lm,\theta}(\widehat{\mathbf{r}})$, $X_{lm,\phi}(\widehat{\mathbf{r}})$ are the components of the vector spherical harmonics, $\mathbf{X}_{lm}(\widehat{\mathbf{r}})$, which are defined by

$$\psi_l\mathbf{X}_{lm}(\widehat{\mathbf{r}}) = \mathbf{L}Y_{lm}(\widehat{\mathbf{r}}) \equiv -i\mathbf{r}\times\nabla Y_{lm}(\widehat{\mathbf{r}})\ . \tag{B.25}$$

By definition, $\mathbf{X}_{00}(\widehat{\mathbf{r}}) = 0$, while for $l \geq 1$

$$\begin{aligned}\psi_l\mathbf{X}_{lm}(\widehat{\mathbf{r}}) &= \left[\alpha_l^{-m}\cos\theta e^{i\phi}Y_{lm-1}(\widehat{\mathbf{r}}) - m\sin\theta Y_{lm}(\widehat{\mathbf{r}}) + \alpha_l^m\cos\theta e^{-i\phi}Y_{lm+1}(\widehat{\mathbf{r}})\right]\widehat{\boldsymbol{\theta}} \\ &\quad + i\left[\alpha_l^{-m}e^{i\phi}Y_{lm-1}(\widehat{\mathbf{r}}) - \alpha_l^m e^{-i\phi}Y_{lm+1}(\widehat{\mathbf{r}})\right]\widehat{\boldsymbol{\phi}} \qquad \text{(B.26)} \\ &= \alpha_l^{-m}Y_{lm-1}(\widehat{\mathbf{r}})\left(\widehat{\mathbf{x}}+i\widehat{\mathbf{y}}\right) + mY_{lm}(\widehat{\mathbf{r}})\ \widehat{\mathbf{z}} + \alpha_l^m Y_{lm+1}(\widehat{\mathbf{r}})\left(\widehat{\mathbf{x}}-i\widehat{\mathbf{y}}\right)\ . \qquad \text{(B.27)}\end{aligned}$$

From the $\mathbf{L}^2Y_{lm} = l(l+1)Y_{lm}$ and $\mathbf{L}^2\mathbf{L} = \mathbf{L}\mathbf{L}^2$ we have $\mathbf{L}^2\mathbf{X}_{lm}(\widehat{\mathbf{r}}) = l(l+1)\mathbf{X}_{lm}(\widehat{\mathbf{r}})$. From Eq. B.25 we can show:

$$\mathbf{X}_{lm}^*(\widehat{\mathbf{r}}) = (-1)^{m+1}\,\mathbf{X}_{l-m}(\widehat{\mathbf{r}})\ , \tag{B.28}$$

$$\mathbf{X}_{lm}(\widehat{\mathbf{r}})\times\widehat{\mathbf{r}} = X_{lm,\phi}(\widehat{\mathbf{r}})\ \widehat{\boldsymbol{\theta}} - X_{lm,\theta}(\widehat{\mathbf{r}})\ \widehat{\boldsymbol{\phi}} = -\frac{ir\nabla Y_{lm}}{\psi_l}\ , \tag{B.29}$$

and

$$\widehat{\mathbf{r}}\times\left[\mathbf{X}_{lm}(\widehat{\mathbf{r}})\times\widehat{\mathbf{r}}\right] = \mathbf{X}_{lm}(\widehat{\mathbf{r}})\ . \tag{B.30}$$

The action of the operators $\nabla\times$ and $\nabla\cdot$ on the $\mathbf{X}_{lm}(\widehat{\mathbf{r}})$ is described by

$$\begin{aligned}\nabla\times\mathbf{X}_{lm}(\widehat{\mathbf{r}}) &= \frac{1}{r}\left[i\psi_l Y_{lm}(\widehat{\mathbf{r}})\,\widehat{\mathbf{r}} - X_{lm,\phi}(\widehat{\mathbf{r}})\,\widehat{\boldsymbol{\theta}} + X_{lm,\theta}(\widehat{\mathbf{r}})\,\widehat{\boldsymbol{\phi}}\right]\\ &= \frac{1}{r}\left[i\psi_l Y_{lm}(\widehat{\mathbf{r}})\,\widehat{\mathbf{r}} - \mathbf{X}_{lm}(\widehat{\mathbf{r}})\times\widehat{\mathbf{r}}\right]\\ &= \frac{i}{\psi_l}\left[\frac{\psi_l^2}{r}Y_{lm}(\widehat{\mathbf{r}})\,\widehat{\mathbf{r}} + \nabla Y_{lm}(\widehat{\mathbf{r}})\right] \qquad \text{(B.31)}\end{aligned}$$

and

$$\nabla\cdot\mathbf{X}_{lm}(\widehat{\mathbf{r}}) = 0, \qquad \text{(B.32)}$$

from which we can derive the relations

$$\nabla\times f_l(x)\mathbf{X}_{lm}(\widehat{\mathbf{r}}) = q\left\{i\psi_l\frac{f_l(x)}{x}Y_{lm}(\widehat{\mathbf{r}})\,\widehat{\mathbf{r}} - \left[f_l'(x)+\frac{f_l(x)}{x}\right]\mathbf{X}_{lm}(\widehat{\mathbf{r}})\times\widehat{\mathbf{r}}\right\} \qquad \text{(B.33)}$$

$$\nabla\cdot\left[f_l(x)\mathbf{X}_{lm}(\widehat{\mathbf{r}})\right] = 0 \qquad \text{(B.34)}$$

$$\nabla^2\left[f_l(x)\mathbf{X}_{lm}(\widehat{\mathbf{r}})\right] = -\nabla\times\left[\nabla\times f_l(x)\mathbf{X}_{lm}(\widehat{\mathbf{r}})\right] = -q^2 f_l(x)\mathbf{X}_{lm}(\widehat{\mathbf{r}})\ , \qquad \text{(B.35)}$$

with $x = qr$. For the above relation we are making use of the relation

$$\begin{aligned}\nabla\left\{\nabla\cdot\left[f_l(x)\mathbf{X}_{lm}(\widehat{\mathbf{r}})\right]\right\} &= \nabla\left[\nabla f_l(x)\cdot\mathbf{X}_{lm}(\widehat{\mathbf{r}}) + f_l(x)\nabla\cdot\mathbf{X}_{lm}(\widehat{\mathbf{r}})\right]\\ &= \nabla\left[\nabla f_l(x)\cdot\mathbf{X}_{lm}(\widehat{\mathbf{r}})\right] = 0\ . \qquad \text{(B.36)}\end{aligned}$$

The vector spherical harmonics fulfil the orthonormality relations

$$\int_0^{2\pi}d\phi\int_0^{\pi}d\theta\sin\theta\ \mathbf{X}_{lm}(\widehat{\mathbf{r}})\cdot\mathbf{X}^*_{l'm'}(\widehat{\mathbf{r}}) = \delta_{ll'}\delta_{mm'} \qquad \text{(B.37)}$$

$$\int_0^{2\pi}d\phi\int_0^{\pi}d\theta\sin\theta\ \mathbf{X}_{lm}(\widehat{\mathbf{r}})\cdot\left[\widehat{\mathbf{r}}\times\mathbf{X}^*_{l'm'}(\widehat{\mathbf{r}})\right] = 0\ , \qquad \text{(B.38)}$$

where we have

$$\begin{aligned}\sum_{lm}\left\{\mathcal{A}^{(1)}_{lm}(r)\mathbf{X}_{lm}(\widehat{\mathbf{r}}) + \mathcal{A}^{(2)}_{lm}(r)\left[\widehat{\mathbf{r}}\times\mathbf{X}_{lm}(\widehat{\mathbf{r}})\right]\right\} &= 0 \Rightarrow\\ \mathcal{A}^{(1)}_{lm}(r) = \mathcal{A}^{(2)}_{lm}(r) &= 0\ . \qquad \text{(B.39)}\end{aligned}$$

Finally, we can show

$$\int_0^{2\pi}d\phi\int_0^{\pi}d\theta\sin\theta\ \mathbf{X}_{lm}(\widehat{\mathbf{r}})\cdot\nabla\left[f_l(r)\mathbf{X}^*_{l'm'}(\widehat{\mathbf{r}})\right] = 0\ , \qquad \text{(B.40)}$$

and by applying the Eq. (B.9) and (B.27)

$$\begin{aligned}\int_0^{2\pi} d\phi \int_0^{\pi} d\theta \sin\theta \; Y_{lm}(\widehat{\mathbf{r}}) \mathbf{X}^*_{l'm'}(\mathbf{r}) &= \frac{\delta_{ll'}}{\psi_l} \Big[\delta_{m+1m'} \alpha_{l'}^{-m'} \left(\widehat{\mathbf{x}} - i\widehat{\mathbf{y}} \right) \\ &+ \delta_{mm'} m \, \widehat{\mathbf{z}} + \delta_{m-1m'} \alpha_{l'}^{m'} \left(\widehat{\mathbf{x}} + i\widehat{\mathbf{y}} \right) \Big] \quad \text{(B.41)}\end{aligned}$$

and

$$\begin{aligned}\int_0^{2\pi} d\phi \int_0^{\pi} d\theta \sin\theta \; Y_{lm}(\widehat{\mathbf{r}}) Y^*_{l'm'}(\widehat{\mathbf{r}}) \, \widehat{\mathbf{r}} &= \delta_{m+1m'} \left(-\gamma_{l+1}^{m+1} \delta_{l+1l'} + \gamma_l^{-m} \delta_{l-1l'} \right) \left(\widehat{\mathbf{x}} - i\widehat{\mathbf{y}} \right) \\ &+ \delta_{m-1m'} \left(\gamma_{l+1}^{-m+1} \delta_{l+1l'} - \gamma_l^{m} \delta_{l-1l'} \right) \left(\widehat{\mathbf{x}} + i\widehat{\mathbf{y}} \right) \\ &+ \delta_{mm'} \left(\zeta_{l+1}^{m} \delta_{l+1l'} + \zeta_l^{m} \delta_{l-1l'} \right) \widehat{\mathbf{z}} \; . \quad \text{(B.42)}\end{aligned}$$

APPENDIX C

Bessel functions

The solutions to Laplace equation, $\nabla^2 F(\mathbf{r}) = 0$, for scalar fields in cylindrical coordinates take the form $F(\mathbf{r}) = F_\nu(x)\exp(\pm qz + i\nu\phi)$, where $\mathbf{r} = (\rho, \phi, z)$ the position vector in cylindrical coordinates $x = q\rho$, and $F_\nu(x)$ the radial solution, which is given by the Bessel equation

$$F_\nu''(x) + \frac{1}{x}F_\nu'(x) + \left(1 - \frac{\nu^2}{x^2}\right)F_\nu(x) = 0 \ , \tag{C.1}$$

where the prime denotes differentiation with respect to the function's argument. The Eq. C.1 is a linear differential equation of second order and therefore, for a specific value of ν, there are two linearly independent solutions. For non-integer values of ν, two linearly independent solutions are the Bessel functions of the first kind $\pm\nu$

$$J_{\pm\nu}(x) = \left(\frac{x}{2}\right)^{\pm\nu} \sum_{s=0}^{\infty} \frac{(-1)^s}{s!\Gamma(s \pm \nu + 1)} \left(\frac{x}{2}\right)^{2s} \ . \tag{C.2}$$

When $\nu(= n)$ is an integer then

$$J_{-n}(x) = (-1)^n J_n(x) \ , \tag{C.3}$$

and a second linearly independent solution is the Bessel function of the second kind

$$N_\nu(x) = \frac{J_\nu(x)\cos(\nu\pi) - J_{-\nu}(x)}{\sin(\nu\pi)} \ , \tag{C.4}$$

which is calculated for $\nu \to n$. From all of the possible solutions of Eq. C.1 only the Bessel function of the first kind does not diverge at $x = 0$. The Bessel functions satisfy the recurrence relations

$$F_{\nu-1}(x) + F_{\nu+1}(x) = \frac{2\nu}{x}F_\nu(x) \tag{C.5}$$

$$F_{\nu-1}(x) - F_{\nu+1}(x) = 2F_\nu'(x) \ . \tag{C.6}$$

The Bessel functions of the first kind can be defined by using integral representations

$$J_\nu(x) = \frac{1}{\pi}\int_0^\pi d\phi \cos(x\sin\phi - \nu\phi) \tag{C.7}$$

$$= \frac{1}{\pi i^\nu}\int_0^\pi d\phi \exp(ix\cos\phi)\cos(\nu\phi) \tag{C.8}$$

$$= \frac{1}{2\pi i^\nu}\int_0^{2\pi} d\phi \exp(i[z\cos\phi + \nu\phi]) \ , \tag{C.9}$$

while the following relations are fulfilled

$$\sum_{n=-\infty}^{\infty} J_n(x) = \sum_{n=-\infty}^{\infty} J_n^2(x) = 1 \tag{C.10}$$

and

$$\exp(ix\cos\phi) = \sum_{n=-\infty}^{\infty} i^n J_n(x)\exp(in\phi) \ . \tag{C.11}$$

The solutions to Helmholtz equation for scalar fields, $\nabla^2 F(\mathbf{r}) + q^2 F(\mathbf{r}) = 0$, take the form $F(\mathbf{r}) = \sum_{lm} f_l(qr) Y_{lm}(\widehat{\mathbf{r}})$, where $Y_{lm}(\widehat{\mathbf{r}})$ are the spherical harmonics (see appendix B), where $\widehat{\mathbf{r}}$ denotes the dependence of the vector $\mathbf{r}$ on the angles θ, ϕ in spherical coordinates, and $f_l(qr)$ is the radial part of the solutions of Helmholtz equation.

$$\left[\frac{1}{r^2}\frac{\partial}{\partial r}\left(r^2\frac{\partial}{\partial r}\right) + q^2 - \frac{l\left(l+1\right)}{r^2}\right] f_l(qr) = 0 \ , \tag{C.12}$$

or, equally,

$$f_l^{''}(x) + \frac{2}{x} f_l^{'}(x) + \left[1 - \frac{l\left(l+1\right)}{x^2}\right] f_l(x) = 0 \ , \tag{C.13}$$

with $x = qr$, if we analyze the operator ∇^2 in spherical coordinates. The Eq. C.13 has, for a specific value of l, two linearly independent solutions. Well known solutions are the Bessel, Neumann and Hankel functions of the first or second kind

$$j_l(x) = \sqrt{\frac{\pi}{2x}} J_{l+1/2}(x) = (2x)^l \sum_{s=0}^{\infty} \frac{(-1)^s\left(s+l\right)!}{s!\left(2s+2l+1\right)!}\ x^{2s} \tag{C.14}$$

$$n_l(x) = \sqrt{\frac{\pi}{2x}} N_{l+1/2}(x) = 2\left(-2x\right)^{-l-1} \sum_{s=0}^{\infty} \frac{(-1)^s\left(s-l\right)!}{s!\left(2s-2l\right)!}\ x^{2s} \tag{C.15}$$

$$h_l^+(x) = j_l(x) + i\ n_l(x) \tag{C.16}$$

$$h_l^-(x) = j_l(x) - i\ n_l(x) \ . \tag{C.17}$$

From all of the possible solutions of Eq. C.1 only the $j_l(x)$ does not diverge at $x = 0$. All the solutions satisfy the recurrence relations

$$xf_l'(x) = lf_l(x) - xf_{l+1}(x) \tag{C.18}$$
$$\big(2l+1\big)\, f_l(x) = xf_{l-1}(x) + xf_{l+1}(x) \tag{C.19}$$
$$xf_{l-1}(x) = xf_l^{'}(x) + \big(l+1\big)\, f_l(x) \tag{C.20}$$
$$\big(2l+1\big)\, f_l'(x) = lf_{l-1}(x) - \big(l+1\big)\, f_{l+1}(x)\ . \tag{C.21}$$

The Wronski determinant is also very useful

$$\begin{vmatrix} j_l(x) & n_l(x) \\ j_l^{'}(x) & n_l^{'}(x) \end{vmatrix} = \frac{1}{x^2}\ . \tag{C.22}$$

The asymptotic behaviour of the spherical Bessel, Neumann and Hankel ($x \gg 1$) functions reads

$$j_l(x \gg 1) \ \sim\ \frac{1}{x}\sin(x - \frac{l\pi}{2}) \tag{C.23}$$
$$n_l(x \gg 1) \ \sim\ -\frac{1}{x}\cos(x - \frac{l\pi}{2}) \tag{C.24}$$
$$h_l^+(x \gg 1) \ \sim\ \big(-i\big)^{l+1}\,\frac{e^{ix}}{x} \tag{C.25}$$
$$h_l^-(x \gg 1) \ \sim\ i^{l+1}\frac{e^{-ix}}{x}\ , \tag{C.26}$$

while for small arguments ($x \ll 1$) we have

$$j_l(x \ll 1) \ \sim\ \frac{x^l}{\big(2l+1\big)!!} \tag{C.27}$$
$$n_l(x \ll 1) \ \sim\ -\frac{\big(2l-1\big)!!}{x^{l+1}}\ . \tag{C.28}$$

Publications and presentations

Publications in peer-reviewed journals

[P1] P. Varytis et al. “Design study of random spectrometers for applications at optical frequencies.” In: *Opt. Lett.* 43.13 (2018), pp. 3180–3183.

[P2] H. Gehring et al. “Low-loss fiber-to-chip couplers with ultrawide optical bandwidth.” In: *APL Photonics* 4.1 (2019), p. 010801.

[P3] W. Hartmann et al. “Waveguide integrated broadband spectrometer based on tailored disorder.” In: (to be submitted).

[P4] P. Varytis and K. Busch. “Negative asymmetry parameter in plasmonic silver-coated dielectric nanospheres.” In: (to be submitted).

[P5] T. Kiel et al. “Enhanced Faraday rotation in all-dielectric magneto-optical metasurfaces composed of shape-optimized nanodisks.” In: (to be submitted).

Conference proceedings

[C1] D.-N. Huynh, P. Varytis, and K. Busch. “A slab waveguide source for discontinuous Galerkin time-domain methods.” In: *Photonics for Solar Energy Systems VII*. Vol. 10688. International Society for Optics and Photonics. 2018, p. 106880V.

Oral presentations

[O1] P. Varytis et al. “Electrodynamic simulations of 2D random spectrometer in the very near-infrared regime.” In: DPG Spring Meeting, Berlin (2018).

Poster presentations

[W1] P. Varytis et al. “Light-Path Engineering in Disordered Waveguiding Systems.” In: MRS Fall Meeting, Boston (2018).

Bibliography

[1] J.D. Jackson. *Classical electrodynamics*. John Wiley & Sons, 1998.

[2] G.B. Arfken, H.J. Weber, and F.E. Harris. *Mathematical methods for physicists: A comprehensive guide*. Academic Press, 2011.

[3] C.F. Bohren and D.R. Huffman. *Absorption and scattering of light by small particles*. John Wiley & Sons, 2008.

[4] A. Kirchner, K. Busch, and C.M. Soukoulis. "Transport properties of random arrays of dielectric cylinders." In: *Phys. Rev. B* 57.1 (1998), p. 277.

[5] H.C. Hulst and H.C. van de Hulst. *Light scattering by small particles*. Courier Corporation, 1957.

[6] J.S. Hesthaven and T. Warburton. "Nodal high-order methods on unstructured grids: I. Time-domain solution of Maxwell's equations." In: *J. Comput. Phys.* 181.1 (2002), pp. 186–221.

[7] K. Busch, M. König, and J. Niegemann. "Discontinuous Galerkin methods in nanophotonics." In: *Laser Photonics Rev.* 5.6 (2011), pp. 773–809.

[8] J. Niegemann, R. Diehl, and K. Busch. "Efficient low-storage Runge–Kutta schemes with optimized stability regions." In: *J. Comput. Phys.* 231.2 (2012), pp. 364–372.

[9] M. König. *Discontinuous Galerkin methods in nanophotonics*. Karlsruhe Institute of Technology (Ph.D. thesis), 2011.

[10] J.S. Hesthaven and T. Warburton. *Nodal discontinuous Galerkin methods: Algorithms, analysis, and applications*. Springer Science & Business Media, 2007.

[11] J.-M. Jin. *The finite element method in electromagnetics*. John Wiley & Sons, 2015.

[12] P. Monk et al. *Finite element methods for Maxwell's equations*. Oxford University Press, 2003.

[13] M. König et al. "Stretched-coordinate PMLs for Maxwell's equations in the discontinuous Galerkin time-domain method." In: *Opt. Express* 19.5 (2011), pp. 4618–4631.

[14] J. Niegemann. *Higher-order methods for solving Maxwell's equations in the time-domain*. Universität Karlsruhe (Ph.D. thesis), 2009.

[15] N.W. Ashcroft and N.D. Mermin. *Solid state physics*. Brooks/Coole Thomson Learning, 2005.

[16] H.J. Hagemann, W. Gudat, and C. Kunz. "Optical constants from the far infrared to the x-ray region: Mg, Al, Cu, Ag, Au, Bi, C, and Al_2O_3." In: *Report of the Deutsches Elektronen-Synchrotron, DESY Sr-74/7* 52 (1974).

[17] H.J. Hagemann, W. Gudat, and C. Kunz. "Optical constants from the far infrared to the x-ray region: Mg, Al, Cu, Ag, Au, Bi, C, and Al_2O_3." In: *J. Opt. Soc. Am.* 65.6 (1975), pp. 742–744.

[18] L. Le Guyader et al. "Nanoscale sub-100 picosecond all-optical magnetization switching in GdFeCo microstructures." In: *Nature Commun.* 6 (2015), p. 5839.

[19] W.R. Hendren et al. "Optical and magneto-optical characterization of TbFeCo and GdFeCo thin films for high-density recording." In: *J. Phys. Condens. Matter* 15.9 (2003), p. 1461.

[20] J. Schöberl. "NETGEN An advancing front 2D/3D-mesh generator based on abstract rules." In: *Comput. Vis. Sci* 1.1 (1997), pp. 41–52.

[21] B. Redding et al. "Compact spectrometer based on a disordered photonic chip." In: *Nat. Photonics* 7.9 (2013), pp. 746–751.

[22] A. Dhakal et al. "Single mode waveguide platform for spontaneous and surface-enhanced on-chip Raman spectroscopy." In: *Interface Focus* 6.4 (2016), p. 20160015.

[23] A. Yodh and B. Chance. "Spectroscopy and imaging with diffusing light." In: *Phys. Today* 48.3 (1995), pp. 34–41.

[24] S.K. Gayen and R.R. Alfano. "Emerging optical biomedical imaging techniques." In: *Opt. Photonics news* 7.3 (1996), p. 16.

[25] H. Zhao et al. "Visible-to-near-infrared octave spanning supercontinuum generation in a silicon nitride waveguide." In: *Opt. Lett.* 40.10 (2015), pp. 2177–2180.

[26] D. J Moss et al. "New CMOS-compatible platforms based on silicon nitride and Hydex for nonlinear optics." In: *Nat. Photonics* 7.8 (2013), pp. 597–607.

[27] I. Goykhman, B. Desiatov, and U. Levy. "Ultrathin silicon nitride microring resonator for biophotonic applications at 970 nm wavelength." In: *Appl. Phys. Lett.* 97.8 (2010), p. 081108.

[28] A.Z. Subramanian et al. "Near-infrared grating couplers for silicon nitride photonic wires." In: *IEEE Photonic Tech. L.* 24.19 (2012), pp. 1700–1703.

[29] S. Romero-García et al. "Silicon nitride CMOS-compatible platform for integrated photonics applications at visible wavelengths." In: *Opt. Express* 21.12 (2013), pp. 14036–14046.

[30] S. Romero-García et al. “Visible wavelength silicon nitride focusing grating coupler with AlCu/TiN reflector.” In: *Opt. Lett.* 38.14 (2013), pp. 2521–2523.

[31] M.P. van Albada et al. “Speed of propagation of classical waves in strongly scattering media.” In: *Phys. Rev. Lett.* 66.24 (1991), p. 3132.

[32] B.A. van Tiggelen et al. “Speed of light in random media.” In: *Phys. Rev. B* 45.21 (1992), p. 12233.

[33] A. Ishimaru. *Wave propagation and scattering in random media*. Vol. 2. Academic press New York, 1978.

[34] T.J. Arruda, A.S. Martinez, and F.A. Pinheiro. “Electromagnetic energy and negative asymmetry parameters in coated magneto-optical cylinders: Applications to tunable light transport in disordered systems.” In: *Phys. Rev. A* 94.3 (2016), p. 033825.

[35] D.J. Pine et al. “Diffusing wave spectroscopy.” In: *Phys. Rev. Lett.* 60.12 (1988), p. 1134.

[36] Q. Hang et al. “Photonic bandgap fiber bundle spectrometer.” In: *Appl. Opt.* 49.25 (2010), pp. 4791–4800.

[37] B. Redding, S.M. Popoff, and H. Cao. “All-fiber spectrometer based on speckle pattern reconstruction.” In: *Opt. Express* 21.5 (2013), pp. 6584–6600.

[38] S. Becker, J. Bobin, and E.J. Candès. “NESTA: A fast and accurate first-order method for sparse recovery.” In: *SIAM J. Imaging Sci.* 4.1 (2011), pp. 1–39.

[39] R. Huschka et al. “Light-induced release of DNA from gold nanoparticles: nanoshells and nanorods.” In: *J. Am. Chem. Soc.* 133.31 (2011), pp. 12247–12255.

[40] S.A. Maier. *Plasmonics: fundamentals and applications*. Springer Science & Business Media, 2007.

[41] M. Kerker, D.-S. Wang, and C.L. Giles. “Electromagnetic scattering by magnetic spheres.” In: *J. Opt. Soc. Am.* 73.6 (1983), pp. 765–767.

[42] R. Gómez-Medina, M. Nieto-Vesperinas, and J.J. Sáenz. “Nonconservative electric and magnetic optical forces on submicron dielectric particles.” In: *Phys. Rev. A* 83.3 (2011), p. 033825.

[43] B. García-Cámara et al. “Exception for the zero-forward-scattering theory.” In: *J. Opt. Soc. Am. A* 25.11 (2008), pp. 2875–2878.

[44] S. Person et al. “Demonstration of zero optical backscattering from single nanoparticles.” In: *Nano Lett.* 13.4 (2013), pp. 1806–1809.

[45] J.-M. Geffrin et al. “Magnetic and electric coherence in forward- and back-scattered electromagnetic waves by a single dielectric subwavelength sphere.” In: *Nature Commun.* 3 (2012), p. 1171.

[46] A. García-Etxarri et al. “Strong magnetic response of submicron silicon particles in the infrared.” In: *Opt. Express* 19.6 (2011), pp. 4815–4826.

[47] W. Liu et al. “Scattering of core-shell nanowires with the interference of electric and magnetic resonances.” In: *Opt. Lett.* 38.14 (2013), pp. 2621–2624.

[48] R. Alaee et al. “A generalized Kerker condition for highly directive nanoantennas.” In: *Opt. Lett.* 40.11 (2015), pp. 2645–2648.

[49] D. Lacoste et al. “Optics of a Faraday-active Mie sphere.” In: *J. Opt. Soc. Am. A* 15.6 (1998), pp. 1636–1642.

[50] W.J.M. Kort-Kamp et al. “Molding the flow of light with a magnetic field: plasmonic cloaking and directional scattering.” In: *J. Opt. Soc. Am. A* 31.9 (2014), pp. 1969–1976.

[51] P. Varytis and N. Stefanou. “Plasmon-driven large Hall photon currents in light scattering by a core–shell magnetoplasmonic nanosphere.” In: *J. Opt. Soc. Am. B* 33.6 (2016), pp. 1286–1290.

[52] R.R. Naraghi, S. Sukhov, and A. Dogariu. “Directional control of scattering by all-dielectric core-shell spheres.” In: *Opt. Lett.* 40.4 (2015), pp. 585–588.

[53] W. Liu et al. “Broadband unidirectional scattering by magneto-electric core–shell nanoparticles.” In: *ACS Nano* 6.6 (2012), pp. 5489–5497.

[54] Y. Li et al. “Broadband zero-backward and near-zero-forward scattering by metallo-dielectric core-shell nanoparticles.” In: *Sci. Rep.* 5 (2015), p. 12491.

[55] M.I. Abdelrahman, C. Rockstuhl, and I. Fernandez-Corbaton. “Broadband suppression of backscattering at optical frequencies using low permittivity dielectric spheres.” In: *Sci. Rep.* 7.1 (2017), p. 14762.

[56] F.A. Pinheiro, A.S. Martinez, and L.C. Sampaio. “New effects in light scattering in disordered media and coherent backscattering cone: systems of magnetic particles.” In: *Phys. Rev. Lett.* 84.7 (2000), p. 1435.

[57] R. Gómez-Medina et al. “Negative scattering asymmetry parameter for dipolar particles: Unusual reduction of the transport mean free path and radiation pressure.” In: *Phys. Rev. A* 85.3 (2012), p. 035802.

[58] L.F. Rojas-Ochoa et al. “Photonic properties of strongly correlated colloidal liquids.” In: *Phys. Rev. Lett.* 93.7 (2004), p. 073903.

[59] G.M. Conley et al. “Light transport and localization in two-dimensional correlated disorder.” In: *Phys. Rev. Lett.* 112.14 (2014), p. 143901.

[60] E. Prodan et al. “A hybridization model for the plasmon response of complex nanostructures.” In: *Science* 302.5644 (2003), pp. 419–422.

[61] T.V. Teperik, V.V. Popov, and F.J. García de Abajo. “Radiative decay of plasmons in a metallic nanoshell.” In: *Phys. Rev. B* 69.15 (2004), p. 155402.

[62] C. Tserkezis, G. Gantzounis, and N. Stefanou. “Collective plasmonic modes in ordered assemblies of metallic nanoshells.” In: *J. Phys. Condens. Matter* 20.7 (2008), p. 075232.

[63] P.B. Johnson and R.W. Christy. “Optical constants of the noble metals.” In: *Phys. Rev. B* 6.12 (1972), p. 4370.

[64] M. Inoue et al. “One-dimensional magnetophotonic crystals.” In: *J. Appl. Phys.* 85.8 (1999), pp. 5768–5770.

[65] H. Kato et al. “Theoretical analysis of optical and magneto-optical properties of one-dimensional magnetophotonic crystals.” In: *J. Appl. Phys.* 93.7 (2003), pp. 3906–3911.

[66] A.A. Fedyanin et al. “Phase-matched magnetization-induced second-harmonic generation in yttrium-iron-garnet magnetophotonic crystals.” In: *IEEE Trans. Magn.* 40.4 (2004), pp. 2850–2852.

[67] A.B. Khanikaev et al. “Nonlinear Verdet law in magnetophotonic crystals: Interrelation between Faraday and Borrmann effects.” In: *Phys. Rev. B* 78.19 (2008), p. 193102.

[68] V.I. Belotelov, L.L. Doskolovich, and A.K. Zvezdin. “Extraordinary magneto-optical effects and transmission through metal-dielectric plasmonic systems.” In: *Phys. Rev. Lett.* 98.7 (2007), p. 077401.

[69] A.B. Khanikaev et al. “Anomalous Faraday effect of a system with extraordinary optical transmittance.” In: *Opt. Express* 15.11 (2007), pp. 6612–6622.

[70] D. Li et al. “Plasmon-enhanced magneto-optical activity in a nanostructure with circle annular arrays.” In: *J. Opt. Soc. Am. B* 33.5 (2016), pp. 922–927.

[71] V.I. Belotelov et al. “Magnetooptical effects in the metal-dielectric gratings.” In: *Opt. Commun.* 278.1 (2007), pp. 104–109.

[72] J.Y. Chin et al. “Nonreciprocal plasmonics enables giant enhancement of thin-film Faraday rotation.” In: *Nature Commun.* 4 (2013), p. 1599.

[73] G. Armelles et al. “Localized surface plasmon resonance effects on the magneto-optical activity of continuous Au/Co/Au trilayers.” In: *Opt. Express* 16.20 (2008), pp. 16104–16112.

[74] A.V. Baryshev, H. Uchida, and M. Inoue. “Peculiarities of plasmon-modified magneto-optical response of gold–garnet structures.” In: *J. Opt. Soc. Am. B* 30.9 (2013), pp. 2371–2376.

[75] M. Caminale et al. “Tuning the magneto-optical response of iron oxide nanocrystals in Au- and Ag-based plasmonic media.” In: *ACS Appl. Mater. Interfaces* 5.6 (2013), pp. 1955–1960.

[76] E. Almpanis et al. “Metal-nanoparticle arrays on a magnetic garnet film for tunable plasmon-enhanced Faraday rotation.” In: *J. Opt. Soc. Am. B* 33.12 (2016), pp. 2609–2616.

[77] A.V. Baryshev and A.M. Merzlikin. “Tunable plasmonic thin magneto-optical wave plate.” In: *J. Opt. Soc. Am. B* 33.7 (2016), pp. 1399–1405.

[78] L. Wang et al. “Plasmonics and enhanced magneto-optics in core-shell Co-Ag nanoparticles.” In: *Nano Lett.* 11.3 (2011), pp. 1237–1240.

[79] G. Armelles et al. “Magneto-optical properties of core-shell magneto-plasmonic $Au - Co_xFe_{3-x}O_4$ nanowires.” In: *Langmuir* 28.24 (2012), pp. 9127–9130.

[80] P. Varytis, P.A. Pantazopoulos, and N. Stefanou. “Enhanced Faraday rotation by crystals of core-shell magnetoplasmonic nanoparticles.” In: *Phys. Rev. B* 93.21 (2016), p. 214423.

[81] J. B. González-Díaz et al. “Surface-magnetoplasmon nonreciprocity effects in noble-metal/ferromagnetic heterostructures.” In: *Phys. Rev. B* 76.15 (2007), p. 153402.

[82] C. Clavero et al. “Magnetic-field modulation of surface plasmon polaritons on gratings.” In: *Opt. Lett.* 35.10 (2010), pp. 1557–1559.

[83] C. Clavero et al. “Magnetic field modulation of intense surface plasmon polaritons.” In: *Opt. Express* 18.8 (2010), pp. 7743–7752.

[84] M.G. Barsukova et al. “Magneto-optical response enhanced by Mie resonances in nanoantennas.” In: *ACS Photonics* 4.10 (2017), pp. 2390–2395.

[85] M. Decker et al. “High-efficiency dielectric Huygens’ surfaces.” In: *Adv. Opt. Mater* 3.6 (2015), pp. 813–820.

[86] A. Christofi et al. “Giant enhancement of Faraday rotation due to electromagnetically induced transparency in all-dielectric magneto-optical metasurfaces.” In: *Opt. Lett.* 43.8 (2018), pp. 1838–1841.

[87] Z. Yu, Z. Wang, and S. Fan. “One-way total reflection with one-dimensional magneto-optical photonic crystals.” In: *Appl. Phys. Lett.* 90.12 (2007), p. 121133.

[88] C. Geuzaine and J.-F. Remacle. “Gmsh: A 3-D finite element mesh generator with built-in pre-and post-processing facilities.” In: *Int. J. Numer. Meth. Eng.* 79.11 (2009), pp. 1309–1331.

[89] M. König, K. Busch, and J. Niegemann. “The discontinuous Galerkin time-domain method for Maxwell’s equations with anisotropic materials.” In: *Photonics Nanostructures: Fundam. Appl.* 8.4 (2010), pp. 303–309.

[90] J. Alvarez et al. “3-D discontinuous Galerkin time-domain method for anisotropic materials.” In: *IEEE Antennas Wirel. Propag. Lett.* 11 (2012), pp. 1182–1185.

Acknowledgments

I would like to thank Professor Kurt Busch for giving me the opportunity to work in his group. Moreover, I would like to express my appreciation to Professor Marian Florescu and Professor Wolfram Pernice for reading and grading this thesis as well as to Professor Oliver Benson and Professor Caterina Cocchi for being members of the examination committee. Special thanks to Wladislaw Hartmann with whom I had a great collaboration, to Helge Gehring and to Professor Wolfram Pernice. I am grateful to my friend and scientist Danny Mantadakis who has proof-read my thesis and to my colleague Thomas Kiel with whom I had a nice collaboration.